BULGARIAN CHEMICAL COMMUNICATIONS

2025 Volume 57 / Special Issue E

Selected papers presented at the 2nd Seminar on investigations, modeling, and optimization of nanocomposite structures, 2 April 2025, Sofia

Journal of the Chemical Institutes of the Bulgarian Academy of Sciences and of the Union of Chemists in Bulgari

PREFASE

The present special issue of the journal Bulgarian Communications (BCC) Chemical selected papers from the presentations delivered at the 2nd SEMINAR ON INVESTIGATIONS, **OPTIMIZATION MODELING AND** OF **NANOCOMPOSITES** STRUCTURES. The Seminar was organized under the auspices of the Institute of Chemical Engineering (IChE) at the Bulgarian Academy of Sciences (BAS), as a leading organization for the implementation of the Contract № KΠ-06-H57/3/15.11.2021 with the Bulgarian National Science Fund (BNSF) under the project: "Optimal safety loads and geometry for layered nanocomposites under thermo-mechanical loading", project leader – prof. Tatyana Petrova.

The 1st **SEMINAR** ON INVESTIGATIONS, **MODELING** AND **OPTIMIZATION** OF **NANOCOMPOSITES** STRUCTURES was held on 23 April 2023 in Sofia, in the IChE - BAS. Both seminars are held with the financial support of BNSF, under the project mentioned above. We hope that these seminars are a good start for the development of new, modern scientific topics at the IChE and that the scientific results reported at them, thanks to the open access and support of the BCC journal, will be widely disseminated.

The 2nd **SEMINAR** ON INVESTIGATIONS, **MODELING** AND **OPTIMIZATION** OF **NANOCOMPOSITES** STRUCTURES, is held on 2nd April, 2025, in the Conference hall, Hotel of BAS, 50 "Shipchenski prohod" blvd.. 1113, Sofia (https://amoravski.github.io/Chemists-Temp-Site/bg/SecondSeminar.htm). About 22 active scientists from 6 institutes of BAS, 5 Bulgarian and two foreign universities, have participated in the Seminar by two plenary lectures, four key lectures, and 16 poster presentations. The scientific program was divided into sections on four different topics: NC - experimental; NC - modeling; NC optimization; and NC - synthesis, structure, and applications. The main objection to such a selection was the consolidation of fundamental research with attempts to apply it to the understanding of nanocomposites design, investigate to experimentally and theoretically the behavior and properties of NCs, and their applications.







During the Seminar, there were invited plenary and key lectures: Prof. Wilfried Becker (Technical University of Darmstadt, Germany), Prof. Tsviatko Rangelov (Institute of Mathematics and Informatics – BAS), MSc. Alexander Moravski (Sofia University St. Kl. Ohridski), PhD, Margarita

Georgieva (Burgas State University, Prof. A. Zlatarov), assoc. Prof. Jenia Georgieva (Institute of Physical Chemistry, BAS), Prof. Tatyana Petrova (IChE-BAS). It is worth underlining the active participation of young scientists at the 2nd Seminar, both with oral presentations and with posters.

April 2025

Guest Editors:

Tatyana Petrova Elisaveta Kirilova

Wear resistance analysis of additively manufactured nanocomposite structures

M. Dimova-Gabrovska¹, Y. Brusarska¹, E. Kirilova^{2*}, D. Shopova³, D. Damyanova⁴, S. Rangelov¹

Received: May 02 2025; Revised: June 09, 2025

Numerous scientific studies describe the benefits of additive manufacturing for the purposes of prosthetic dental medicine. The materials used in this technology must have mechanical properties close to those of the tissues they aim to restore. The present study aims to test, under laboratory conditions, the wear resistance of additively manufactured trial nanocomposite specimens made from CROWNTEC. The specimens were grouped according to their orientation during printing. The surface normal vector in Group A forms an angle of 0° with the printing platform, in Group $B - 30^{\circ}$, in Group $C - 60^{\circ}$, and in Group $D - 90^{\circ}$. To conduct the laboratory study, the "Sofia" chewing simulator was used. Spheres made of silicon nitride were selected as antagonistic elements, and distilled water was used as the liquid medium. Each specimen underwent 50,000 chewing simulation cycles, and the results were recorded using a Mettler Toledo ME303 analytical balance. After analyzing the results, it was found that the specimens had the highest average weight in Group B (6.526 g \pm 0.037 g) and the lowest in Group D (6.511 g \pm 0.032 g). The other two groups had an average weight of 6.515 g (\pm 0.032 g) for Group C and 6.515 g (\pm 0.044 g) for Group A. Wear of the material was greatest when the printed layers were at a 30° angle to the printing platform surface and lowest when the layers were parallel to the platform.

Keywords: additive manufacturing; wear resistance; nanocomposite materials; prosthetic dental medicine.

INTRODUCTION

Additive manufacturing is becoming increasingly applicable in all fields of dental medicine [1-4]. This technology enables the fabrication of 3D models through the layer-by-layer deposition of material [5-7]. Over the past decade, three-dimensional printing has become an alternative to subtractive manufacturing [8-10].

A primary priority in the treatment with removable and fixed prosthetic structures is the fulfillment of the medico-biological indicator "function," contributing to the long-term health of the patient [11-14]. 3D printing technology allows the use of various materials, facilitating the choice of this method for the fabrication of both removable and fixed prosthetic constructions [15-17]. Three-dimensional printing enables the rapid production of complex structures, significantly shortening the timeframes for therapeutic procedures [18].

The main requirements for materials used in fixed prosthetics are reviewed and summarized in numerous studies [3, 16, 19-21]. The mechanical and physical properties of both conventional and additive manufacturing materials should be close or

even identical to those of the tissues they replace [22-27].

One mechanical property of dental materials that attracts significant scientific interest is wear resistance [28-31]. Wear resistance is the property of a material to resist the process of abrasion. The chewing function is a mechanical loading process where restorative materials interact with opposing teeth, creating friction that results in the loss of both the material and the hard-dental tissues [19]. Wear depends on many factors, such as surface condition, structure homogeneity, material fatigue, load level, and the presence of intermediaries like saliva and food [20, 32-34].

The wear resistance of dental materials is critical to the clinical longevity of prosthetic structures. Abrasion of restorative materials deteriorates aesthetics and promotes the adhesion of microorganisms to prosthetic surfaces [35].

Ceramic materials and metal alloys are preferred for permanent fixed structures due to their low wear rates, whereas resin-based materials exhibit significantly higher abrasion [23, 36-38]. The growing interest in additive manufacturing requires the development of new generations of materials

¹Department of Prosthetic Dental Medicine, Faculty of Dental Medicine, Medical University – Sofia, 1, Sv. Georgi Sofiyski Str., Sofia 1431, Bulgaria

²Institute of Chemical Engineering, Bulgarian Academy of Sciences, Acad. G. Bontchev, Str., Bl. 103, 1113 Sofia, Bulgaria

³Department of Prosthetic Dental Medicine, Faculty of Dental Medicine, Medical University -Plovdiv, 3, Hr. Botev Blvd., 4000, Bulgaria

⁴Department of Pediatric Dental Medicine, Faculty of Dental Medicine, Medical University "Prof. Dr. Paraskev Stoyanov" – Varna, 55 Marin Drinov Str., Varna 9002, Bulgaria

^{*} To whom all correspondence should be sent: E-mail: elisavetakirilova.iche.bas@gmail.com

suited for this technology. To meet the needs of fixed prosthetics, composites reinforced with inorganic fillers such as zirconium nanoparticles, silanized dental glass, and ceramics are now being introduced to the market [39].

In 2022, SAREMCO (Switzerland) introduced a new nanocomposite material with ceramic inclusions for additive manufacturing of permanent fixed restorations – CROWNTEC. The material is designed for the fabrication of permanent restorations, such as single crowns, inlays, onlays, and veneers. Composition-wise, it is a light-curing, flowable methacrylic acid-based polymer [40, 41]. Due to its composition and the relevance of additive technologies, this new generation of materials is a justified subject of scientific interest.

The mechanical characteristics of resin-based materials depend on several factors, such as filler shape, filler size, hardness, and printing parameters [39, 42]. Studies have shown that these materials are susceptible to rapid aging. When exposed to liquid environments like the oral cavity, resin-based materials absorb water, leading to a degradation of their mechanical properties by affecting the polymer network [43].

The available scientific literature indicates that additive manufacturing offers the possibility to produce fixed prosthetic structures using modern nanocomposites [18, 44]. The wear resistance of these materials determines their clinical longevity and functionality [39]. The mechanical characteristics of resinous structures applied *via* 3D printers highlight the necessity for laboratory studies in this area. Analyzing wear resistance is crucial to determining their potential for use in fixed prosthetics [8, 19].

AIM OF THE STUDY

The present study aims to laboratory test the wear resistance of additively manufactured trial nanocomposite bodies made from CROWNTEC material.

Null Hypothesis (*H*₀): The weights of the specimens are comparable across all groups.

Alternative Hypothesis (H_1): The weights of the specimens vary significantly among the groups.

MATERIALS AND METHODS

For the study, 60 trial bodies were manufactured from the nanocomposite material CROWNTEC (SAREMCO, Switzerland) with incorporated ceramics. The specimens were divided into four groups based on their spatial orientation during printing:

Group A: normal vector forms an angle of 0° with the printing platform surface;

Group B: normal vector forms an angle of 30° with the printing platform surface;

Group C: normal vector forms an angle of 60° with the printing platform surface;

Group D: normal vector forms an angle of 90° with the printing platform surface.

The difference in spatial orientation during additive manufacturing leads to structural differences corresponding to the angles of 0°, 30°, 60°, and 90°.

The digital design and preparation for printing were carried out using the "3D Sprint" software, while the specimens were printed using a NextDent 5100 (NextDent, USA) 3D printer based on digital light processing (DLP).

Laboratory tests were performed using the "Sofia" chewing simulator, developed by Dr. I. Chakalov [45]. Specimens were cylindrical, with an external diameter of 25 mm and a height of 9 mm, as per the simulator requirements. Silicon nitride (Si₃N₄) spheres were used as antagonists (Fig. 1), and distilled water was the liquid medium.



Figure 1. Silicon nitride spheres.

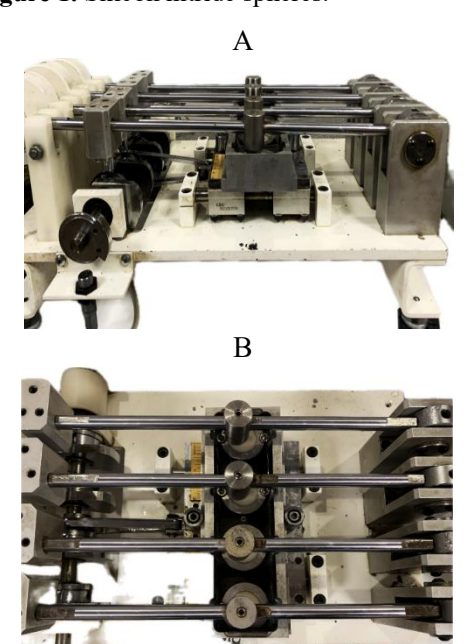


Figure 2. Chewing simulator "Sofia".

The testing methodology consisted of the antagonist descending onto the sample to simulate initial tooth contact, followed by a sliding movement with dynamic force variation, ending with the antagonist detaching from the sample. Each specimen underwent six paths, equating to 50,000 chewing cycles (Fig. 2 A and B).

Measurements were taken using the Mettler Toledo ME303 (Mettler Toledo, Switzerland) analytical balance to determine the sample masses before and after the chewing simulation (Fig. 3 A and B).

A) Before

B) After



Figure 3. Mettler Toledo ME303 analytical balance measuring sample weights before and after the simulation.

Statistical methods used

- Descriptive statistics
 - Average a measurement of the average tendency;
 - Mean –a measurement of the characteristic in the middle;
 - Standard deviation (SD) a measurement of the average dispersion;
 - Lower (LCL) and Upper (UCL) the limits within which the actual mean of the general population lies;
 - Absolute (N) values a measurement for determining the number of cases;
 - Minimum value and Maximum value.
- Hypothesis testing
 - Parametric test for difference in "k" number of independent samples (ANOVA test);

- Post-hoc test to determine between which groups of "k" number of independent samples are significant differences;
- The independent samples t-test (also known as the two-sample t-test) is a parametric statistical test used to determine whether there is a significant difference between the means of two independent groups.

All hypothesis testing was conducted with a 5% significance threshold.

Statistics were performed with IBM SPSS Statistics 26, and graphs were generated with Excel 2010.

RESULTS

In the present study, a total of 60 test specimens were examined, evenly distributed into four groups (A, B, C, and D) according to the angle of the normal vector to the surface relative to the printing platform (angles of 0°, 30°, 60°, and 90°, respectively). The mass of the specimens was measured in grams both before and after the experiment in order to assess the level of wear resistance.

The measured average mass of the specimens prior to the experiment was 6.535 g, with a standard deviation of ± 0.039 g. The lightest specimen weighed 6.460 g, while the heaviest weighed 6.612 g. Half of the specimens were lighter than 6.534 g, and the other half were heavier.

The measured average mass of the specimens after the experiment was 6.517 g, with a standard deviation of ± 0.036 g. The lightest specimen weighed 6.449 g, and the heaviest weighed 6.579 g. Half of the specimens were lighter than 6.519 g, and the other half were heavier. (Table 1). When examining the differences between the mean weights of the specimens in the groups at the beginning of the experiment, the highest mean weight was recorded in Group B (6.563 g ± 0.036 g), while the lowest mean weight was observed in Group D (6.517 g ± 0.031 g). The remaining two groups had mean weights of 6.528 g (±0.033 g) for Group C and 6.530 g (± 0.041 g) for Group A. The difference between the groups is graphically represented in Figure 4.

Table 1. Summary of the statistical characteristics of the sample. Unit of measurement: (g)

Group	Mean	Median	Std. deviation	Minimum	Maximum	LCL/UCL	N
Before the experiment	6.535	6.534	0.039	6.460	6.612	6.525 / 6.544	60
After the experiment	6.517	6.519	0.036	6.449	6.579	6.499 / 6.535	60

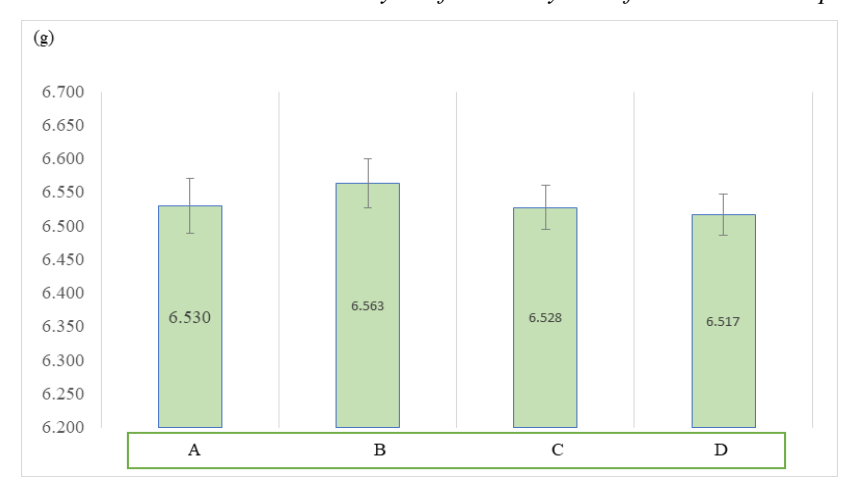


Figure 4. Difference in the weights of the specimens between groups at the beginning of the experiment, (g).

The significance level was determined with a test error of 5%. The distribution of weights was assessed using the Kolmogorov-Smirnov test, which confirmed a normal distribution of weights within each group (Table 2). Therefore, the differences were analyzed using analysis of variance (ANOVA) for comparing the means of several independent samples.

Table 2. Results of the normality test for the weight distribution within each group prior to the experiment. One-Sample Kolmogorov-Smirnov Test

Group		Weight	Result
		before (g)	
A	Asymp. Sig.	.200 ^{a, b}	Normal
	(2-tailed)		distribution
В	Asymp. Sig.	.054ª	Normal
	(2-tailed)		distribution
С	Asymp. Sig.	.200 ^{a, b}	Normal
	(2-tailed)		distribution
D	Asymp. Sig.	.200 ^{a, b}	Normal
	(2-tailed)		distribution

^a Lilliefors significance correction. ^b This is a lower bound of the true significance.

The significance level obtained from the test [p = 0.5%] is lower than the accepted risk of error of 5%. Therefore, the alternative hypothesis is accepted, stating that there is a statistically significant difference in the weights of the specimens between

the groups prior to the experiment. To determine specifically between which groups the differences are significant, a post-hoc test was conducted using the Least Significant Difference (LSD) test. The results revealed that a significant difference exists between the weight of Group B and the weights of all other groups, while no significant differences were found among Groups A, C, and D. This conclusion can be stated with 95% confidence (Table 3).

Following the statistical analysis of the data regarding differences in mean weights between groups after the experiment, the highest mean weight was observed in Group B (6.526 g ± 0.037 g), while the lowest mean weight was found in Group D (6.511 g ± 0.032 g). The other two groups exhibited mean weights of 6.515 g (± 0.032 g) for Group C and 6.515 g (± 0.044 g) for Group A. The differences between the groups are graphically presented in Figure 5.

Testing the weight distribution after the experiment using the Kolmogorov-Smirnov test indicated a normal distribution within each group (Table 4). Therefore, the verification of differences was conducted through analysis of variance (ANOVA) for comparing the means of several independent samples.

Table 3. Results from the test of differences in specimen weights between groups prior to the experiment.

Tested group		Groups under test				
Char. under test	Characteristics	A	В	C	D	
	Mean	6.530 A	6.563 ^B	6.528 A	6.517 A	
Weight	SD	±0.041	± 0.036	±0.033	±0.031	
	N	15	15	15	15	
ANOVA test	P-value	p=0.005				

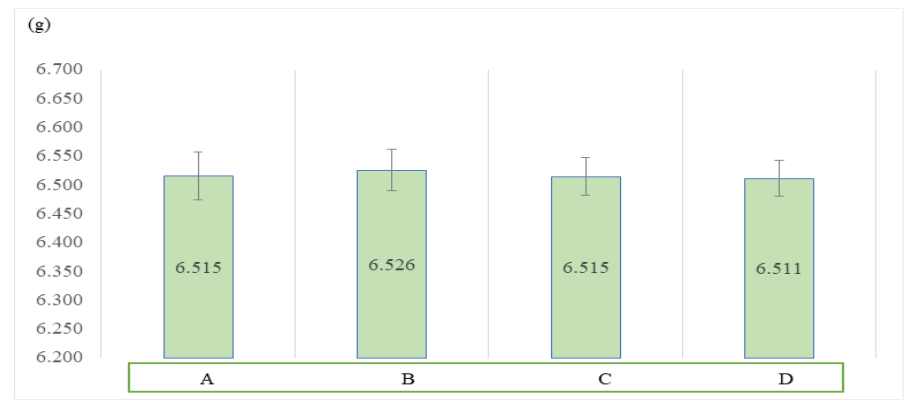


Figure 5. Differences in specimen weights between groups after completion of the experiment, (g).

Table 4. Results of the normality test for the distribution of specimen weights within each group after the experiment. One-Sample Kolmogorov-Smirnov Test

Group		Weight	Result
		before (g)	
A	Asymp. Sig.	.200 ^{a, b}	Normal
	(2-tailed)		distribution
В	Asymp. Sig.	.071a	Normal
	(2-tailed)		distribution
C	Asymp. Sig.	.200 ^{a, b}	Normal
	(2-tailed)		distribution
D	Asymp. Sig.	.200 ^{a, b}	Normal
	(2-tailed)		distribution

^a Lilliefors significance correction. ^b This is a lower bound of the true significance.

The significance level obtained from the test [p = 74.1%] is higher than the accepted risk of error of 5%. Therefore, the null hypothesis is accepted, stating that there is no statistically significant difference in the weights of the specimens between the groups, and that any observed differences are of a random nature. This indicates that the wear resistance across the groups after the experiment is identical. This conclusion can be stated with 95% confidence (Table 5).

Additionally, the difference between the mean weights of the specimens in the groups before and after the experiment was determined. The greatest

difference in weight after the experiment was observed in Group B, where, as a result of wear resistance, a decrease of -0.038 g was recorded. The smallest difference in weight after the experiment was observed in Group D, with a decrease of -0.006 g due to wear resistance. In the remaining two groups, the decreases in weight were -0.015 g for Group A and -0.013 g for Group C. Graphically, the differences among the groups are presented in Figure 6.

The distribution of the weights within the groups had already been tested using the Kolmogorov–Smirnov test (Tables 2 and 4), which indicated a normal distribution of weights in each group. Therefore, the verification was performed using a T-test for the difference between two means of two related samples.

The significance level obtained from the tests [p < 0.001%] is lower than the accepted risk of error of 5%. Consequently, the alternative hypothesis is accepted, stating that there is a statistically significant difference in the direction of weight reduction after the experiment. This indicates that statistically significant wear occurred in each group. This conclusion can be stated with 95% confidence (Table 6).

Table 5. Results from the test of differences in specimen weights between groups after the experiment.

Tested group	Classitia	Groups under test				
Char. under test	Characteristics	A	В	С	D	
	Mean	6.515 ^A	6.526 A	6.515 ^A	6.511 ^A	
Weight	SD	± 0.044	± 0.037	± 0.032	±0.032	
	N	15	15	15	15	
ANOVA test	P-value	p=0.741				

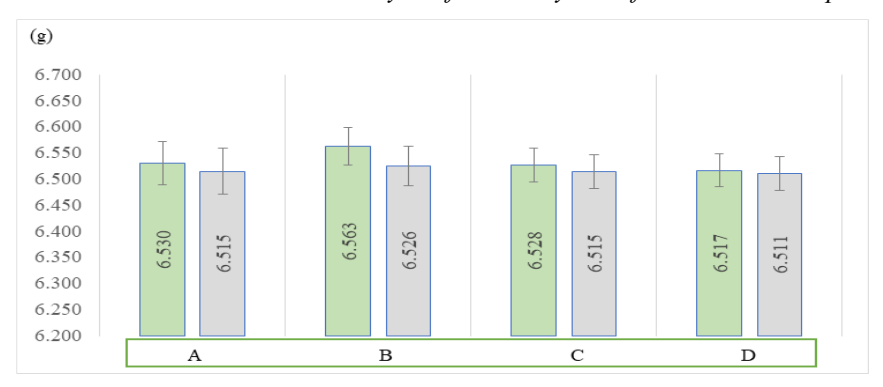


Figure 6. Difference in specimen weights in the groups before and after the experiment, (g).

Table 6. Results from the test of differences in specimen weights between groups prior to the experiment.

Tested group				Groups under test					
Char.	Characteristics	A	A	I	3	(C	I)
under test		Before	After	Before	After	Before	After	Before	After
	Mean	6.530^{A}	6.515 ^B	6.563 ^A	6.526^{B}	6.528 ^A	6.515^{B}	6.517 ^A	6.511 ^B
Weight	SD	±0.041	±0.044	±0.036	±0.037	±0.033	±0.032	±0.031	±0.032
	N	15	15	15	15	15	15	15	15
T test	P-value	p<0	.001	p<0	.001	p<0	.001	p<0	.001

DISCUSSION

The results of the conducted study confirmed the null hypothesis when comparing the mass between the groups before and after the experiment.

Analysis of the specimens' mass before and after the chewing simulation suggests a probable dependence on the orientation during the printing process.

Prior to the laboratory testing, the mean mass of the specimens in Group B was the highest (6.563 g ± 0.036 g), while Group D exhibited the lowest mean mass (6.517 g ± 0.031 g). Groups A and C demonstrated intermediate values with relatively close mean weights (6.530 g and 6.528 g, respectively), suggesting a potential influence of the printing angle on the specimens' mass, possibly due to differences in layer structure and degree of compaction.

Following the application of the laboratory chewing simulation, the same trend in the distribution of group weights was observed. Group B again showed the highest mean weight (6.526 g ± 0.037 g), and Group D remained the lowest (6.511 g ± 0.032 g). Groups C and A continued to exhibit closely aligned values (6.515 g), highlighting that the initial differences in specimen mass persisted after simulation without leading to significant changes in the dynamics between the groups.

The differences between the groups after loading were minimal, indicating that regardless of the initial mass, the specimens exhibited relatively similar behavior in terms of wear resistance. This, in turn, suggests that spatial orientation affects the initial parameters of the specimens but does not have a substantial impact on wear resistance during chewing simulation.

When comparing the differences in the mean mass of the specimens within the groups before and after the experiment, a statistically significant difference was identified, leading to the rejection of the null hypothesis and confirmation of the alternative hypothesis.

Analysis of the results from the laboratory investigation showed that the greatest average weight loss occurred in Group B, where the post-experimental weight difference was 0.038 g, and the smallest in Group D -0.006 g. For the other two groups (A and C), the average material loss was 0.015 g and 0.013 g, respectively.

These values highlight the existence of a relationship between the spatial orientation of the material layers on the studied surface of the specimens and wear resistance. Specimens from Group B, where the normal vector to the surface forms a 30° angle with the printing platform, demonstrated the highest susceptibility to material loss under mechanical loading, likely due to the specific arrangement of layers during printing. This could lead to lower structural stability of constructions in the long term.

The specimens from Group D, where the normal vector to the surface forms a 90° angle, exhibited the lowest degree of wear. This may indicate better wear resistance of the material when the structural layers

are horizontally oriented relative to the printing platform.

The discussed results support the hypothesis that the spatial orientation of the specimens during printing influences the material's wear resistance. These findings could serve as a foundation for determining the optimal orientation in the design and printing of structures made from the nanocomposite material CROWNTEC. Proper spatial orientation of the material layers in permanent fixed constructions could contribute to the long-term success of prosthetic treatment.

CONCLUSIONS

In conclusion, the results of the present study clearly highlight the significant influence of the structural orientation of the layers in additively manufactured specimens made of the nanocomposite material CROWNTEC on the wear resistance of their surfaces. Furthermore, the scientific investigation demonstrated that the printing angle affects the mass of the printed objects.

The highest degree of wear occurred when the material layers were oriented at a 30° angle, while the lowest wear was observed when the layers were horizontally oriented relative to the printing platform, where the normal vector to the surface forms a 90° angle. This leads to the conclusion that the specimens from Group D possess the highest wear resistance.

The results of the present study are supported by findings in a scientific paper published in 2022 [46], where the CROWNTEC material demonstrated relatively low wear values (35.5 \pm 30.2 μm). This aligns with the hypothesis that both the material composition and the spatial orientation during 3D printing play a crucial role in determining wear resistance.

Conversely, in a more recent study by *Grymak et al.* (2024) [47], CROWNTEC exhibited a higher tendency to wear compared to other additively manufactured materials, such as NextDent C&B MFH, particularly under varying loads and environmental conditions. The authors highlight the importance of surface treatment in enhancing wear resistance, suggesting that a combination of optimal spatial orientation and proper surface finishing may significantly improve the performance of prosthetic structures made from CROWNTEC.

Additionally, a comparative study by Türksayar et al. (2024) [48] reinforced the significance of spatial orientation in additive manufacturing by evaluating the mechanical properties of 3D printed versus subtractively manufactured implant-supported crowns. Their findings show that

additively manufactured crowns may possess competitive, or even superior, wear resistance under specific conditions. These results further support the hypothesis that well-defined printing parameters are essential in optimizing the long-term durability of prosthetic constructions made from CROWNTEC.

The experimental data suggests that, for practical applications, it is advisable to orient the material layers' parallel to the printing platform in the zones subject to mechanical loading, in order to enhance the wear resistance of permanent fixed constructions.

Acknowledgement: The data presented in this study are subject to investigation in the Research Project Competition "Grant-2024," entry number 132/29.05.2024, at the Medical University - Sofia.

REFERENCES

- I. Katreva, T. Dikova, M. Abadzhiev, T. Tonchev, D. Dzhendov, M. Simov, S. Angelova, D. Pavlova, M. Doychinova, Scr. Sci. Med. Dent., 2(1), 7 (2016).
- S. Yanakiev, N. Kostova-Kamburova, M. Moskova,
 S. Simeonov, E. Micheva, *Health Sci.*, 1–2(049–050), 182 (2023).
- 3. M. Dimova-Gabrovska, Y. Brusarska, *Sci. Works Union Sci. Bulg.-Plovdiv, Ser. G. Med. Pharm. Dent.*, **XXXI**, 118 (2024).
- 4. Z. Tomova, Y. Zhekov, and A. Vlahova, *Folia Med. (Plovdiv)*, **66(3)**, 431, 2024.
- I. Taneva, 3D Printed Splints for Prevention of Complications in Bruxism - Experimental and Clinical Study, Sofia, 2022.
- 6. Z. Tomova, Y. Zhekov, G. Alexandrov, A. Vlahova, E. Vasileva, *Aust. Dent. J.*, **68**, 294 (2023).
- 7. Z. Tomova, A. Vlahova, I. Stoeva, Y. Zhekov, E. Vasileva, *Open Access. Maced. J. Med. Sci.*, **10**, 143 (2022).
- 8. A. Barazanchi, K. C. Li, B. Al-Amleh, K. M. Lyons, J. N. Waddell, *J. Prosthodont.*, **26(2)**, 156 (2017).
- 9. G. Oberoi, S. Nitsch, M. Edelmayer, K. Janjić, A. S. Müller, H. Agis, *Front. Bioeng. Biotechnol.*, **6**, 172 (2018).
- 10. Z. Tomova, A. Vlahova, S. Zlatev, I. Stoeva, D. Tomov, D. Davcheva, V. Hadzhigaev, *Dent. J.* (*Basel*), 11, 166 (2023).
- D. Damyanova, V. E. Panov, S. T. Angelova, J. IMAB, 21(3), 879 (2015).
- 12. M. Dimova-Gabrovska, D. Dimitrova, D. Konstantinova, I. Gerdzhikov, *Knowledge Int. J.*, **19(4)**, (2017).
- M. Al-Omiri, M. G. Sghaireen, M. M. Alhijawi, I. A. Alzoubi, C. D. Lynch, E. Lynch, *J. Oral Rehabil.*, 41(8), 624 (2014).
- 14. B. Al-Zarea, Med. Princ. Pract., 24(2), 142 (2015).
- M. Dimova-Gabrovska, C. R. Acad. Bulg. Sci., 16 (2023)

- 16. A. Vlahova, S. Zlatev, CAD/CAM technologies in prosthetic dentistry, 2021.
- 17. R. Vladova, T. Petrova, E. Kirilova, B. Boyadjiev, A. Apostolov, W. Becker, A. Moravski, *Acta Polytechnica CTU Proceedings*, **50**, 94 (2024).
- F. Rezaie, M. Farshbaf, M. Dahri, M. Masjedi, R. Maleki, F. Amini, J. Wirth, K. Moharamzadeh, F. E. Weber, L. Tayebi, *J. Compos. Sci.*, 7(2), 80 (2023).
- 19. I. Anastassov, Y. Yoshida, T. Dragev, *Dental Materials*, (2013).
- 20. J. Manappallil, Basic Dental Materials, (2015).
- O. Pecho, R. Ghinea, E. A. N. do Amaral, J. C. Cardona, A. Della Bona, M. M. Pérez, *Dent. Mater.*, 32(5), 105 (2016).
- 22. S. Elsaka, A. M. Elnaghy, *Dent. Mater.*, **32(7)**, 908 (2016).
- 23. L. Fu, H. Engqvist, W. Xia, *Materials (Basel)*, **13(5)**, 1049 (2020).
- 24. N. Intralawan, T. Wasanapiarnpong, P. Didron, T. Rakmanee, A. Klaisiri, N. Krajangta, *J. Int. Dent. Med. Res.*, **15(4)**, 1465 (2022).
- 25. B. Yang, S. Wang, G. Wang, X. Yang, *J. Mech. Behav. Biomed. Mater.*, **124**, 104859 (2021).
- N. Krajangta, A. Klaisiri, S. Leelaponglit, N. Intralawan, P. Tiansuwan, N. Pisethsalasai, *Dent. Mater. J.*, 43(3), 386 (2024).
- Z, Tomova, A. Chonin, I. Stoeva, A. Vlahova, *Folia Med. (Plovdiv)*, **65**, 664 (2023).
- 28. A. Lee, L. H. He, K. Lyons, M. V. Swain, *J. Oral Rehabil.*, **39(3)**, 217 (2012).
- 29. A. Diken Türksayar, M. Demirel, M. B. Donmez, E. O. Olcay, T. F. Eyüboğlu, M. Özcan, *J. Prosthet. Dent.*, **132(1)**, 154 (2024).
- L. Cao, X. Zhao, X. Gong, S. Zhao, *Int. J. Clin. Exp. Med.*, 6(6), 423 (2013).
- 31. E. Kirilova, T. Petrova, W. Becker, J. Ivanova, *ZAMM*, **97(9)**, 1136 (2017).
- 32. S. Kumar, A. Patnaik, I. K. Bhat, *Materwiss*. *Werksttech.*, **51(1)**, 96 (2020).

- 33. R. Vladova, T. S. Petrova, E. G. Kirilova, A. G. Apostolov, B. Ch. Boyadjiev, *Bulg. Chem. Commun.*, **54(4)**, 349 (2022).
- 34. E. Vasileva, Z. Tomova, S. Yankov, I. Hristov, *J. Int. Dent. Med. Res.*, **14**, 485 (2021).
- M. Nayyer, S. Zahid, S.H. Hassan, S.A. Mian, S. Mehmood, H.A. Khan, M. Kaleem, M.S. Zafar, A.S. Khan, *Eur. J. Dent.*, **12(1)**, 57 (2018).
- 36. S. Heintze, F. Reichl, R. Hickel, *Dent. Mater. J.*, **38(3)**, 343 (2019).
- R. Sedlák, M. Ivor, P. Klimczyk, P. Wyzga, M. Podsiadlo, M. Vojtko, J. Dusza, *Ceramics*, 4(1), 40 (2021).
- 38. H. Xing, B. Zou, S. Li, X. Fu, *Ceram. Int.*, **43(18)**, 16340 (2017).
- A. Grymak, J. M. Aarts, A. B. Cameron, J. J. E. Choi, J. Dent., 147, 105120 (2024).
- 40. Permanent 3D printed crowns CROWNTEC, https://saremco.ch/en/products/crowntec
- Instruction for Use I saremco print CROWNTEC I US-version, https://saremco.ch/en/pages/document/gebrauchsan-weisungen
- 42. T. Petrova, E. Kirilova, W. Becker, J. Ivanova, *IOP Conf. Ser. Mater. Sci. Eng.*, **461**, 012067 (2018).
- M. Reymus, R. Fabritius, A. Keßler, R. Hickel, D. Edelhoff, B. Stawarczyk, *Clin. Oral Investig.*, 24(2), 701 (2020).
- 44. A. Vlahova, V. Hadzhigaev, Z. Tomova, R. Kazakova, S. Zlatev, *J. Dent. Oral Care.*, **4**, 5 (2018).
- 45. I. Chakalov, Wear resistance of dental materials in vitro studies, Medical University Sofia, Faculty of Dental Medicine, 2014.
- 46. D. Takada, T. Kumagai, F. Fusejima, T. Ueno, S. Kariya, *J. Dent. Oral Care*, **38(2)**, 42 (2022).
- 47. A. Grymak, J.M. Aarts, A.B. Cameron, J.J.E. Choi, J. *Dent. Sci.*, **147**, 105120 (2024).
- 48. A.A. Diken Türksayar, M. Demirel, M.B. Donmez, E.O. Olcay, T.F. Eyüboğlu, M. Özcan, *J. Prosthet. Dent.*, **132(1)**, 154 (2024).

Synthesis, characterization and application aspects of barium titanate-based ceramic samples with graphene nanostructures introduced

A. A. Georgieva*, F. S. Yovkova, K. Z. Panayotova

Burgas State University "Prof. Dr. Assen Zlatarov", Department of Chemical Technology, 1, Prof. Yakimov Blvd., Burgas 8000, Bulgaria

Received: May 05, 2025; Revised: June 17, 2025

The share of research work aimed at finding innovative approaches to the synthesis of new porous ceramic products to be applied as filters for purification of waste waters, as adsorbents, heat-insulation materials and other components with high thermal resistance, as well as biomedical and catalytic substrates has recently increased. The present paper reports for the preparation of barium titanate-based ceramic samples containing up to 2 mass % of graphene nanostructures (graphene nanoplatelets GnP), synthesized by the method of solid-state sintering. The methods of X-ray diffraction, FT-IR spectroscopy, scanning electron microscopy and light microscopy were used for the characterization of the initial blends and the titanate ceramic samples obtained from them. The results of the analyses showed that the introduced nanoadditive initiated the formation of fine-grain porous structure with grain sizes from 0.5 to 1 μ m. Some basic physicomechanical properties of the samples synthesized were determined, e.g., water absorption (WA, %), apparent density (ρ_{app} , g/cm^3) and apparent (open) porosity (P_{app} , %). The apparent density was close to the theoretical one 5.51 g/cm^3 , the open porosity was 2.04 % and the minimal water absorption - 0.37 %. Some aspects of application are proposed.

Keywords: Ceramic samples, Barium titanate, Graphene nanostructures, Porous ceramic materials, Physicomechanical properties

INTRODUCTION

Ceramic materials based on titanium dioxide. titanates, zirconates and compounds with similar properties form a class of technical ceramics widely used in radio-engineering, electronics, ultrasonic and other application fields for preparation of capacitors and piezoceramic components. Many ceramic materials, obtained from titanates, zirconates and stannates, which are characterized by higher, very high and ultrahigh dielectric permeability, are used to manufacture highfrequency and low-frequency capacitors with linear (induced) or non-linear (spontaneous) polarization [1]. BaTiO₃, as a very important dielectric ceramic material, was widely used for large-scale production of capacitors due to its superior dielectric properties and low cost [2]. Capacitors made from insulating ceramics provide outstanding power density and fast charge-discharge features, making them ideal devices for pulse power applications [3]. Despite the proven benefits, the exploration of BaTiO₃-based high-entropy ceramics is lacking. There's still much potential to uncover in this area.

The literature review revealed that numerous research teams are concentrating on developing approaches for synthesizing new porous ceramic components. These components have potential

applications as wastewater filtration materials, adsorbents, heat insulation materials, and high thermal resistance parts for use in biomedical and catalytic substrates. Besides, the introduction of graphene and its derivatives in the ceramics provides new possibilities for enhancing existing materials and imparting new versatile properties, such as crack propagation resistance, bending strength, electric conductivity, electromagnetic and heat-conductive properties [1, 4-8].

In this regard, the aim of the present work is to obtain and characterize barium titanate-based ceramic samples containing graphene nanostructures, to determine their main physicomechanical properties and propose areas of their possible application.

MATERIALS AND METHODS

Materials

Barium titanate ceramic samples containing up to 2 mass % of graphene nanostructures were prepared by the method of solid-state sintering of predominantly diffusion nature. In most cases, this approach is used for the preparation of special ceramics and it is considered to be completed to sufficient degree when the initial materials are in the form of highly disperse powders.

^{*} To whom all correspondence should be sent: E-mail: adriana georgieva79@yahoo.com

- Initial materials and blend compositions. The following initial materials were used for the preparation of the barium titanate-based ceramic samples with composition D0: highly dispersed BaTiO₃ powder 98 mass % (Sigma Aldrich, purity > 99%) and graphene nanoplatelets GnP 2 mass % (graphene nanoplatelets, Sigma Aldrich).
- Formation and sintering of the ceramic samples. The preparation of the ceramic blends and the synthesis of the samples were carried out as follows: the initial highly dispersed materials were weighed and dry homogenized. The plasticizer used was 4% polyvinyl alcohol. The samples were formed by a semi-dry method on a hydraulic press under pressure of 40 MPa. The samples were then dried at 120°C for 70 min and at 180°C for 50 min. The temperature regime of the sintering process was: at 200°C - isothermal period of 20 min, at 300°C - 20 min, at 400°C - 20 min, at 500°C - 30 min, at 800°C - 30 min, at 1100°C - 30 min, and 1 h isothermal period at the highest temperature of 1300°C. After the end of the second isothermal period, the furnace was switched off and the samples were left to cool freely. The aim of this method was to achieve maximum densification of diffusion nature and obtain porous materials good physicomechanical properties.

Methods

The initial powders and the barium titanate-based ceramic obtained from them were characterized by X-ray powder diffraction, FT-IR spectroscopy, scanning electron microscopy and light microscopy.

- Infrared spectroscopy. FT-IR spectra were taken using Tensor 27 FT-IR spectrophotometer (Bruker, Germany) in the interval 400 4000 cm⁻¹ at a resolution of 1 cm⁻¹. The studies were carried out at room temperature. The sample (0.3 mg) was pressed into KBr (100 mg) pellet at a pressure of 2-4 atm.
- *X-ray powder analysis*. The XRD pattern was recorded using automated computer-controlled XRD system D500 Siemens (Germany) under the following regime: 40 kV, 30 mA, monochromatic copper radiation.
- Scanning electron microscopy. The SEM analysis of the ceramic materials obtained was carried out on a scanning electron microscope Tabletop SEM HIROX SH-4000M, 30× 60 000×, SE&BSE detector, voltage 5 kV 30 kV, resolution 15 nm. The samples were preliminarily wired with gold.
- *Light microscopy*. The Celestron 5 MP LCD Deluxe digital light microscope was used.

RESULTS AND DISCUSSION

The initial blends and the sintered samples were studied by IR spectroscopy. The IR spectra obtained were analyzed and interpreted and the main functional groups present in the compositions of the samples containing 2% of GnP were established. The results of the FT-IR analysis of blend D0 are presented in tabular form in Table 1 and graphically in Fig. 1.

Table 1. Absorption bands and functional groups present in the composition of sintered ceramic samples containing 2 mass % of graphene nanostructures

rs,	Samples from blend D0 sintered at 1300°C	Bond
ave	3447.49	С-Н
CI M	533.35	Ba-Ti-O
=	407.57	Ti-O

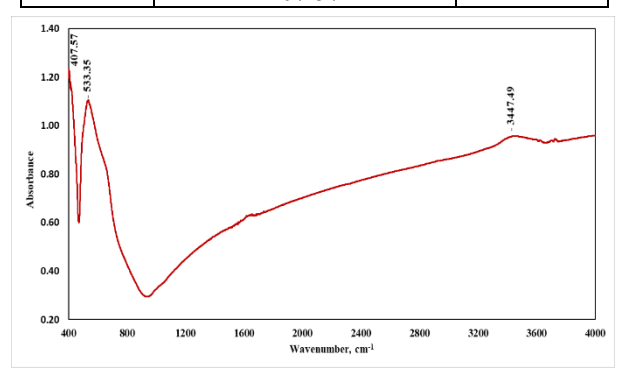


Figure 1. FT-IR spectrum of barium titanate-based sample prepared from blend D0 and sintered at 1300°C

In the spectra of the samples studied, absorption bands were observed at ~3447.49 cm⁻¹ (Fig. 1) which are characteristic of the C–H bond [5] and indicate the presence of carbon containing structures. Most probably, part of the specially introduced graphene structures was burnt during the high-temperature sintering, thus imparting certain porosity within the ceramics obtained.

XRD proved the synthesis of barium titanate ceramics with main phase BaTiO₃ (Fig. 2). Its existence was confirmed by FT-IR analysis.

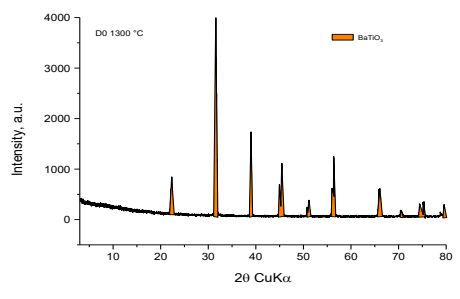


Figure 2. Powder X-ray diffraction pattern of blend D0

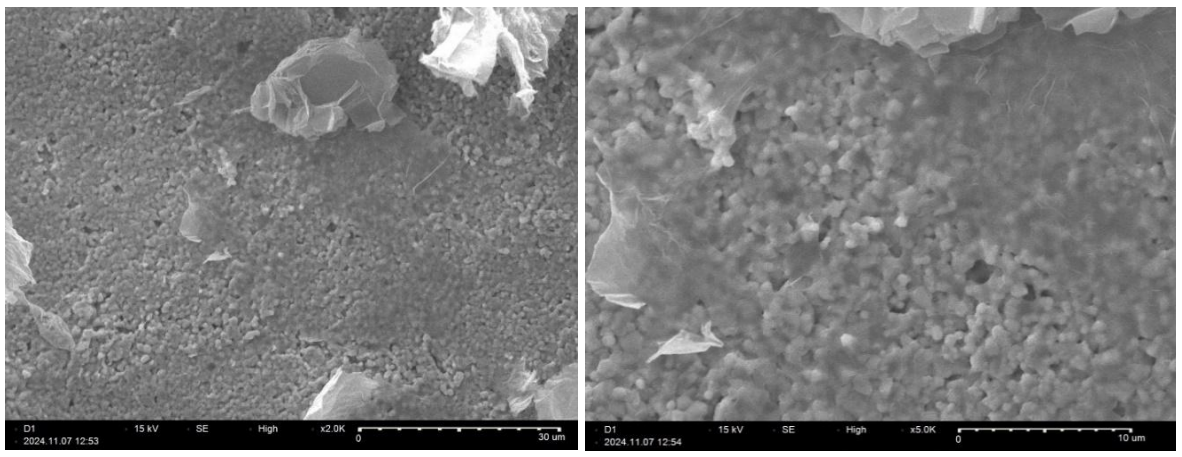


Figure 3. SEM microphotographs of barium titanate-based ceramic samples synthesized from blend D0 at 1300°C



Figure 4. Photographs of the surface of the ceramic materials synthesized

Table 2. Basic physicomechanical properties of the ceramic samples synthesized

Sample № with composition	<i>WA</i> ,	ρ _{app} ,	P _{app} ,
	%	g/cm ³	%
D0	0.37	5.51	2.04

The SEM analysis of the ceramic samples obtained revealed finely grained porous structure with grain sizes from 0.5 to 1 μ m. SEM images of titanate ceramics with added 2% of graphene nanoplatelets GnP taken at different magnifications are shown in Fig. 3.

The surface of the ceramic samples synthesized with added 2% of graphene GnP was studied by light microscopy. The photographs shown in Figure 4 reveal a relatively homogeneous and finely grained structure. It can be seen that open pores had been formed in some places. Obviously, part of the carbon containing material burned with the increase of the temperature and this resulted in formation of certain porosity in the ceramic.

Some basic physicomechanical properties of the barium titanate-based ceramics with added graphene nanoplatelets were determined: water absorption (WA, %), apparent density $(\rho_{app}, g/cm^3)$ and apparent (open) porosity $(P_{app}, \%)$.). The results obtained are presented in Table 2. The apparent density is the ratio between the mass of the material and the volume it occupies including the pores $\rho_{app} = \frac{m}{V}, \frac{kg}{m^3}, \frac{g}{m^3}$. The volume of the pores is usually determined by hydrostatic weighing of water-soaked samples. The apparent density of the samples synthesized was calculated by the expression:

$$\rho_{app} = \frac{m_0 \cdot \rho_m}{V} = \frac{m_0 \cdot \rho_m}{m_1 - m_2}, \frac{kg}{m^3}$$

where: m_0 – mass of the dry sample, kg; m_1 – mass of the water-soaked sample, kg; m_2 – mass of the water-soaked sample weighed under water, kg; V – sample volume, m^3 ; ρ_m – density of the liquid used, kg/m³.

The apparent porosity is the ratio between the volumes of the open pores to the volume of the material including all the pores it contains, in %. The apparent porosity is determined by the expression:

A. A. Georgieva et al.: Synthesis, characterization and application aspects of barium titanate-based ceramic samples...

 $P_{app} = WA. \rho_{app}$, % and the water absorption - $WA = (m_1 - m_0). \frac{100}{m_0}$, where - m_0 is the mass of the dry material, g; m_1 – mass of the material water soaked at high temperature, g [1].

According to literature data, the density of BaTiO₃ is $5.3 \div 5.8 \ g/cm^3$ [1].

The data in Table 2 show that the introduction of a small quantity of graphene in the initial blends (2 mass %) followed by solid-state sintering gave barium titanate-based ceramics with sufficient density (close to the theoretical one), minimal water absorption and some open porosity. Therefore, the graphene structures introduced even in small quantities play the role of pore-forming agents in the ceramics. This observation was confirmed by the results obtained from the analyses carried out (infrared spectroscopy, scanning electron microscopy and light microscopy), as discussed above.

CONCLUSIONS

As a result of the research carried out, samples of barium titanate ceramics were synthesized using the diffusion-type solid-state sintering method. The samples were prepared from initial blends where a small amount of graphene nanostructures (2 mass %) was introduced. For the characterization of the initial blends and the ceramics obtained from them, the methods of X-ray phase analysis, infrared spectroscopy, scanning electron microscopy and light microscopy were used. The main crystalline phases present in the ceramics synthesized were determined by XRD. The analysis proved the synthesis of ceramic with main phase BaTiO₃. The main functional groups present in the compositions of the ceramic samples synthesized were identified by FT-IR while the morphology and structure were studied by SEM. The results of the analyses showed that the introduced nano-additive initiated the formation of a finely grained porous structure with grain sizes from 0.5 to 1 µm. The surface of the BaTiO₃ ceramics prepared by sintering at 1300°C was investigated by light microscopy to find that the samples prepared from blend D0 had relatively homogeneous and finely grained surface. Some physicomechanical properties of the barium titanate

ceramics synthesized were also determined. It had sufficient density, close to the theoretical one -5.51 g/cm³, certain open porosity -2.04 % and minimal water absorption -0.37 %. The results of the studies carried out indicate that, most probably, the introduction of small quantities of graphene in the initial blends, followed by high temperature sintering resulted in burning of part of the graphene structures and imparted some porosity to the ceramic samples obtained.

The porous ceramic materials can be used as heat insulation materials, filtering components, catalytic substrates and dielectric materials in capacitors. Given the characteristics of the synthesized barium titanate ceramics, its dielectric permeability needs to be determined to evaluate its potential application in capacitor devices.

Acknowledgement: The authors wish to express their gratitude to the Scientific Research Institute at the University "Prof. Dr. Assen Zlatarov"- Burgas (contract № HUX-498/2024) for the assistance provided for the realization of the present study.

REFERENCES

- A. Gerasimov, A. Atanasov, V. Toshev, D. Petkov, D. Ivanov, L. Georgieva, L. Pavlova, H. Drenska, P. Vinarov, P. Petrov, S. Bachvarov, S. Panova, S. Bagarov, S. Serbezov, S. Stefanov, S. Dzhambazov, T. Stojkova, T. Datskova, H. Berlinov, Technology of Ceramic Products and Materials, S. Bachvarov (ed.), Saraswati press, Sofia, Bulgaria, 2003, p. 889.
- Zh. Bi, Sh. Zhou, J. Ye, N. Wang, F. Shang, J. Xu, H. Wang, *Ceramics International*, **51** (12), Part A, 16052 (2025).
- J. Zhou, Z. Xu, H. Yang, L. Chu, L. Chen, H. Li, J. Ding, S. Ran, Zh. Sun, X. Hao, *Chem. Eng. J.*, 487, 150476 (2024).
- 4. H. Porwal, S. Grasso, MJ. Reece, *Adv. Appl. Ceram.*, **112**, 443 (2013).
- M. Georgieva, A. Georgieva, K. Panayotova, F. Yovkova, I. Markovska, *Bulg. Chem. Commun.*, 55 (3), 344 (2023).
- 6. Y. Huang, Ch. Wan, *J. of Adv. Ceram.*, **9** (3), 271 (2020).
- 7. I. Ali, X. Mbianda, A. Burakov, E. Galunin, I. Burakova, E. Mkrtchyan, A. Tkachev, V. Grachev, *Environ. Int.*, **127**, 160 (2019).
- M. Li, X. Yin, L. Chen, M. Han, L. Cheng, L. Zhang, *Ceram. Int*, 42 (6), 7099 (2016).

Synthesis and properties of Ni-doped finely dispersed ceramic pigments

M. G. Minova*, F. S. Yovkova, I. G. Markovska, A. A. Georgieva

Burgas State University "Prof. Dr. Assen Zlatarov", Department of Chemical Technology, 8000, 1 Prof. Yakimov Blvd., Burgas, Bulgaria

Received: May 05, 2025; Revised: June 06, 2025

This work aims to synthesize finely dispersed ceramic pigments by the solid-phase synthesis method. Two series of pigments were obtained – from pure and waste raw materials. In the first case, pure raw materials - Al_2O_3 and SiO_2 were used. The initial SiO_2 was introduced into the mixtures as amorphous $SiO_2.nH_2O$. An amorphous form of silica – $SiO_2.nH_2O$ was chosen because it is significantly more reactive than ordinary quartz sand and has a degree of particle dispersion in the range of $2\div7~\mu m$. In the second case, Al_2O_3 and oxidized rice husk ash (RHA) were used, which contained 94.47 % of silica. The synthesis was carried out at temperatures of 1350 °C and 1400 °C with 1-hour isothermal period in a Nabertherm oven. The chromophore used was Ni introduced into the mixtures as NiO. The amount of the chromophore was 5 %. Finely dispersed pigments with a blue-green color were obtained. The synthesized pigments were studied by a number of methods - X-ray diffraction, SEM, DSC, etc. Using the CIELab system, which gives a numerical expression of the visual sensation of color, the basic color characteristics of the pigments were determined - color, brightness, color hue. The pigments synthesized from pure raw materials at 1350 °C had the best indicators, respectively, (a) = - 15.2 and (b) = - 4.9.

Keywords: ceramic pigments, Ni-chromophore, rice husk, solid-state sintering, CIELab system

INTRODUCTION

One of the main methods for producing ceramic pigments with different chromophores – such as nickel, copper, chromium, cobalt, vanadium, iron, etc. is solid-phase synthesis [1]. Ceramic pigments are essentially colorants, which, when applied to various materials, give them a certain color. In this regard, they are widely used in the silicate industry, where they are added to glazes for coloring floor and wall tiles (such as monoporosa), inks for decorating ceramic and glass products, etc. When coloring ceramic tiles, the relative production quantities with about 10 million square meters of tiles per year are about 20-30 tons of pigments depending on the models that are produced. That is why the interest in their production, as well as in the development of new types of highly refractory pigments is very high. In the synthesis of inorganic ceramic pigments, often used as nickel compounds are very following chromophores. Nickel has the characteristics: oxidation state 2⁺, coordination numbers 4 and 6 (most often), spatial coordination tetrahedron and octahedron [2]. In silicate systems, the change in the coordination state of nickel varies depending on the ratio of alkali metal oxides and silicon dioxide. The appearance of nickel in quadruple coordination depends on the strengths of the Me-O single bonds in alkali metal oxides [3].

In ceramic pigments, nickel can be found in the form of the following complexes: [NiO₄] - blue color, [NiO₆] - brown color, or Ni₂SiO₄ - green color. Nickel oxide NiO is resistant to the action of high temperatures, but dissolves in ammonia and concentrated mineral acids. Other nickel compounds are easily soluble in water - Ni(NO₃)₂.6H₂O, NiSO₄.7H₂O, forming green solutions [4].

Wang *et al.* [5] synthesized solid-phase inorganic pigments based on Ni-doped Al₂TiO₅. They used a Ni chromophore, which was added to the batch as NiO. The resulting material has a blue-green color due to the d-d transition of Ni²⁺ in octahedral coordination. It turns out that with the introduction of Ni, the Vickers microhardness values of the composite are higher. Patrocínio *et al.* [6] synthesized a blue pigment based on Ni-doped Zn₂GeO₄. They noted that the pigment is characterized by low toxicity, a bright blue hue, and excellent chemical and thermal resistance.

The present work aims to synthesize finely dispersed ceramic pigments with a nickel chromophore by the solid-phase synthesis method. An innovative and ecological aspect of our work is the fact that we have found a way to utilize agricultural waste, such as rice husks. Millions of tons of rice husks are generated worldwide per year. In some of the compositions, we use rice husk ash

^{*} To whom all correspondence should be sent: E-mail: *minova m@abv.bg*

instead of amorphous SiO₂.nH₂O. The pigments obtained in this way are in no way inferior to those obtained from pure raw materials. On the contrary, in some cases, they give better colors. From an economic point of view, the price of the produced pigments is lower, since waste material is used.

MATERIALS AND METHODS

Materials

Al₂O₃ with a purity of 99.9 % and SiO₂ were used as starting materials. Silicon dioxide was introduced in some of the compositions as amorphous SiO₂.nH₂O, and in others as rice husk ash (RHA). The inorganic part of the raw husk consists of about 20 % SiO₂ and about 5.5 % mixture of: CaO, Fe₂O₃, MgO, Al₂O₃, Na₂O, K₂O, MnO₂ [7]. Ni was used as a chromophore element in an amount of 5 %. Ni was introduced with NiO. Table 1 presents the compositions of the synthesized ceramic pigments.

Fig. 1 shows the scheme for obtaining the pigments.

Table 1. Pigment compositions

Sample №	Composition		Synthesis temperature, °C
M3-5	Al ₂ O ₃	SiO ₂ .nH ₂ O	1350
MR3-5	Al_2O_3	RHA	1350
P3-5	Al ₂ O ₃	SiO ₂ .nH ₂ O	1400
PR3-5	Al ₂ O ₃	RHA	1400

The preparation of the pigments involves several stages. First, the components are mixed and homogenized dry. The thus prepared batches are placed in corundum crucibles and fired in a Nabertherm high-temperature furnace. Firing was done at two final temperatures of 1350 °C and 1400 °C with an isothermal hold of 1 hour. This is followed by cooling to room temperature. The synthesized pigments are removed from the furnace and visually inspected. The pigments are ground in an agate mortar.

Methods

- *Color measurement.* The color of the pigments was determined spectrally on a Lovibond tintometer RT 100 Color.
- *SEM.* The samples were analyzed by scanning electron microscopy (SEM) at 10.00 kV accelerating voltage using an IEM11 microscope, Inovenso INC (Turkey).
- *Hot-stage microscopy (HSM)*. High-temperature microscope ESS Misura HSM 1400 ODHT, model 1600/80, Italy (IFH-BAS) was used. The sample was heated to 1400 °C at a rate of 10 °C min⁻¹, and the graph reflects the changes that occur during heating.
- X-ray diffraction. X-ray diffraction (XRD) was performed on a Bruker D8 Advance automatic powder X-ray diffractometer with CuKα radiation (Ni filter) and registration by a LynxEye solid-state detector. The X-ray spectrum was recorded in the angular range from 5.3 to 80° 2θ with a step of 0.03° 2θ. Qualitative phase analysis was performed using the PDF-2(2009) database of the International Center for Diffraction Data (ICDD). Quantitative analysis was performed with the Topas 2 program.
- DSC. The DSC experiments were performed on an apparatus for complex thermal analysis (STA 449 F3 Jupiter), Netzsch, Germany, by heating to 1100 °C at a rate of 10 °C min⁻¹.

RESULTS AND DISCUSSION

Mixtures studies

The mixtures were studied by DSC, and the results are presented in Figs. 2 and 3. The DSC curves of the two mixtures are quite different. This is explained by the fact that in the batch with pure raw materials, we have SiO₂.nH₂O, while in the other batch, it is replaced by RHA. The first low-temperature endothermic reactions (1) and (2) in Figs. 2 and 3 in both batches can be attributed to the separation of adsorbed water. In Fig. 3 between 400 - 500 °C, we see a large endothermic effect (3), both in height and area. Probably, the unburnt particles in RHA burn. Here the mass loss is the greatest. The endothermic peak (3) in Fig. 2 in the interval 500-550 °C is due to the dehydration of SiO₂.nH₂O.

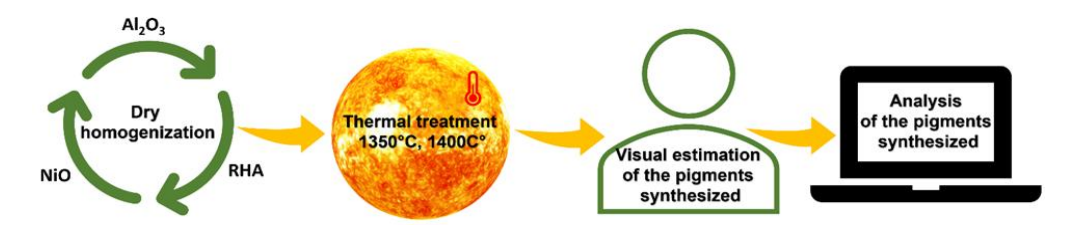


Figure 1. Scheme of pigment preparation

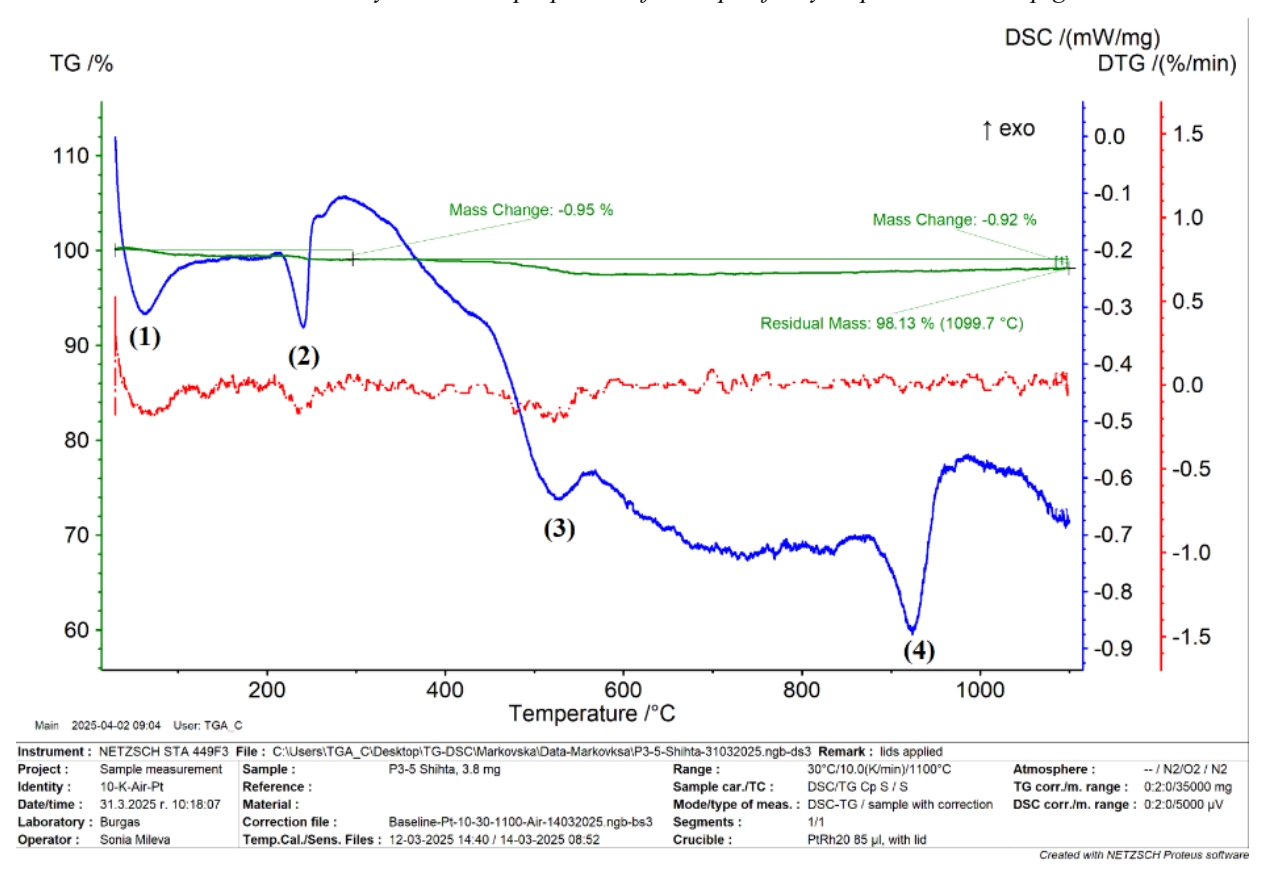


Figure 2. DSC of the mixtures with pure raw materials (Al₂O₃ and SiO₂.nH₂O)

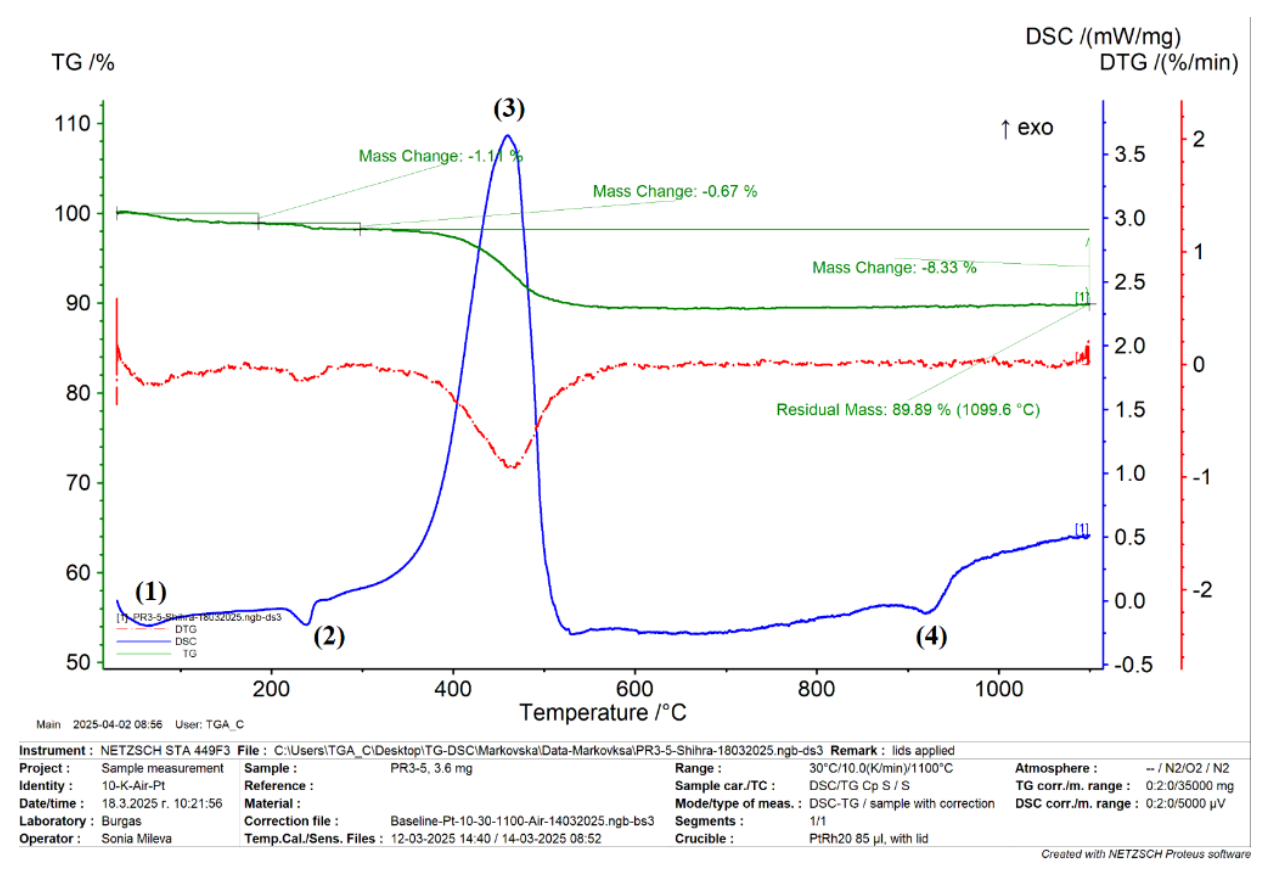


Figure 3. DSC of the mixtures with waste RHA (Al₂O₃ and RHA)

The product of the endothermic processes (4) (Figs. 2 and 3) in the temperature range 900-960 °C is NiAl₂O₄ (spinel) which is formed by a chemical reaction between NiO and Al₂O₃. Javanmardi *et al.* also obtained NiAl₂O₄ by solid-phase synthesis at about 900-960 °C. However, to reach these low temperatures of synthesis they ground the raw materials for many hours. In our work, due to the addition of RHA to the samples, the process was accelerated, since the impurities contained in RHA act as mineralizers and lower the synthesis temperature of the spinel phase [8].

We could not trace endothermic effects of other high-temperature compounds, since the heating of the samples in this analysis was up to 1100 °C.

Hot-stage microscopy (HSM) results of the mixtures

Figure 4 shows the hot-stage microscopy (HSM) results of mixtures obtained from pure raw materials - Al₂O₃ and SiO₂.nH₂O.

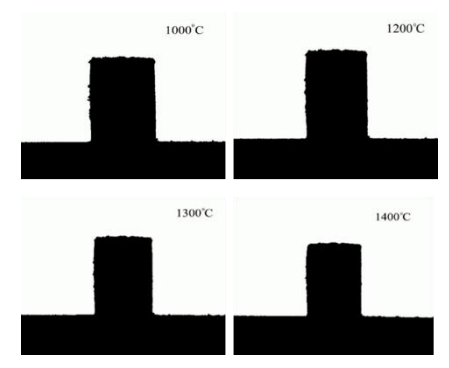


Figure 4. Hot-stage microscopy (HSM) of batches obtained from pure raw materials

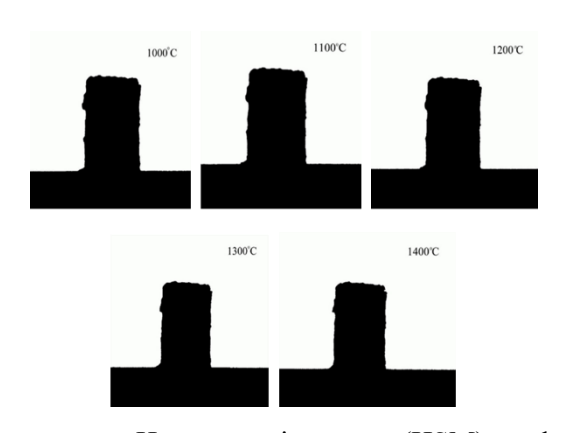


Figure 5. Hot-stage microscopy (HSM) results of mixtures obtained from waste RHA

From Fig. 4 it is seen that up to 1400 °C, the shape of the samples remains constant, without visible changes. Extremely high thermal stability of the samples is observed. Fig. 5 shows the results of hotstage microscopy (HSM) of mixtures obtained from Al₂O₃ and RHA, as a source of SiO₂.

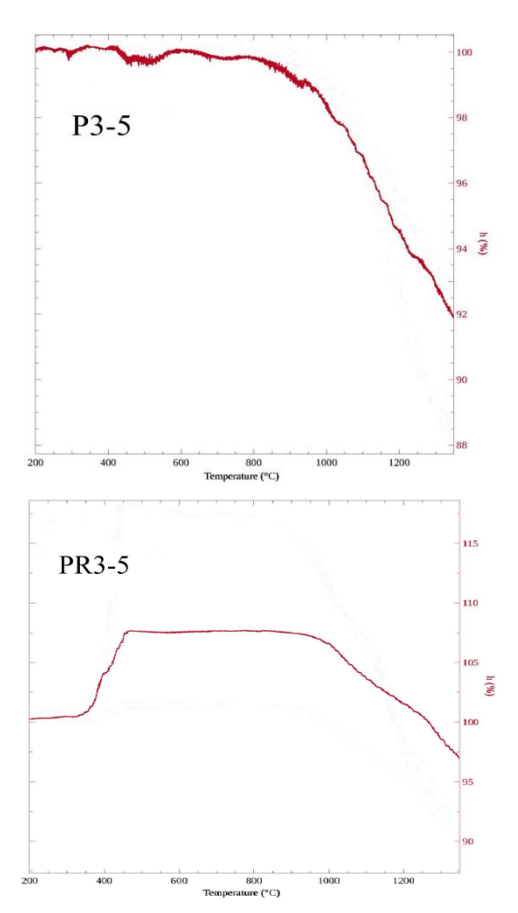


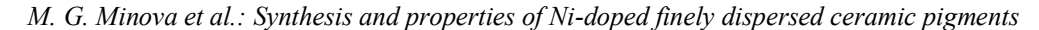
Figure 6. Summary results of hot-stage microscopy for samples without (P3-5) and with rice husk (PR3-5) in their compositions.

The results of Fig. 6 prove the stability of both types of samples. This can be explained in the following way - firstly because the pigments are fired at a lower temperature (1350 °C). Secondly, a tendency to form nickel spinel is observed, in which Al₂O₃ binds to nickel. The remaining Al₂O₃ passes into corundum. SiO₂, due to the inability to bind to Al₂O₃ to mullite, turns into cristobalite.

For comparison, Khattab *et al.* synthesized mullite pigments from waste material containing silica. They reported results similar to ours. At 1300-1350 °C they also obtained corundum and cristobalite as the main phases. With increasing temperature to 1400°C, mullite is mainly formed, while the amount of corundum and cristobalite decreases [9].

Pigments studies

Figure 7 presents the results of the X-ray analysis. It reveals the main phases in the synthesized ceramic pigments, which are: corundum (Al_2O_3), cristobalite (SiO_2), mullite ($3Al_2O_3.2SiO_2$), and nickel spinel ($NiAl_2O_4$). Mullite is detected only in samples P3-5 and PR3-5, fired at 1400 °C. Mullite is not observed in samples M3-5 and MR3-5.



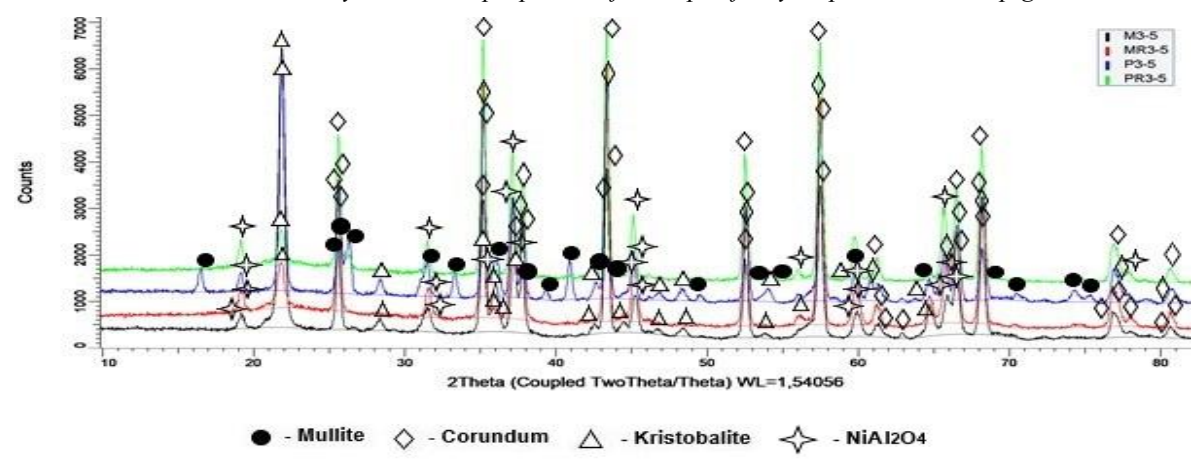


Figure 7. XRD of samples M3-5, MR3-5, P3-5, PR3-5

Figure 8. presents the main phases in the synthesized samples in mass percentages.

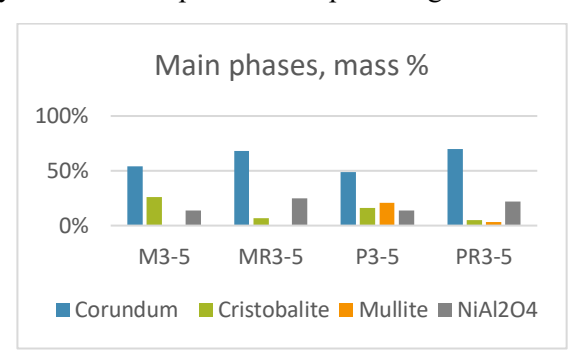


Figure 8. Main phases in the samples

The graph in Fig. 9 shows the crystal sizes of the main phases in the samples.

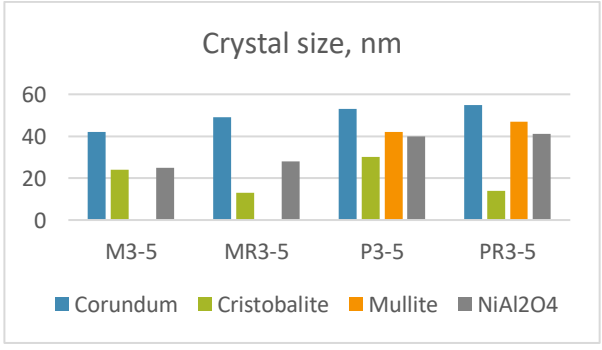


Figure 9. Crystal size of samples.

Table 2. Color coordinates of samples

Composition	T, °C	Color	L*	a *	b *
M3-5	1350		96.3	-15.2	-4.9
MR3-5	1350		79.0	-12.8	-2.9
P3-5	1400		75.2	-15.1	-2.5
PR3-5	1400		76.5	-13.6	-4.2

The size of the crystalline phases varies from 13 nm (MR3-5) to 55 nm (PR3-5), with the average crystal size for each phase being: corundum - 49.75 nm, cristobalite - 20.25nm, mullite - 44.5 nm and NiAl₂O₄ - 33.5 nm.

Color measurement

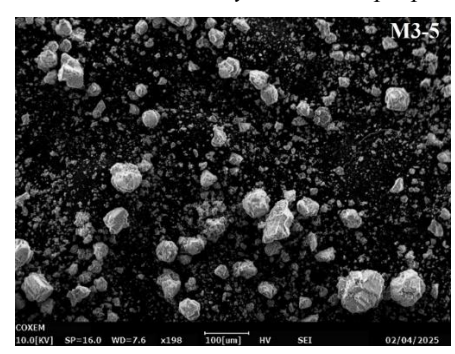
There are different systems for reporting and measuring colors - MKO 1931, CIELuv, CIELab, etc. [10, 11]. For the needs of ceramics in Europe and the USA, the most widely used system is the CIELab system with color coordinates:

- L^* brightness, $L^*=0$ black color, $L^*=100$ white color;
 - a* green color () / red color (+);
 - b* blue color () / yellow color (+).

In our study, the color of the pigments was determined spectrally with a tintometer from the company Lovibond Tintometer RT 100 Color, with the CIELab system.

All synthesized pigments have a beautiful bluegreen color due to the d - d transition of Ni^{2+} in octahedral coordination. The pigments synthesized from pure raw materials at 1350 °C had the best indicators, respectively (a) = -15.2 and (b) = -4.9 (Table 2).

M. G. Minova et al.: Synthesis and properties of Ni-doped finely dispersed ceramic pigments



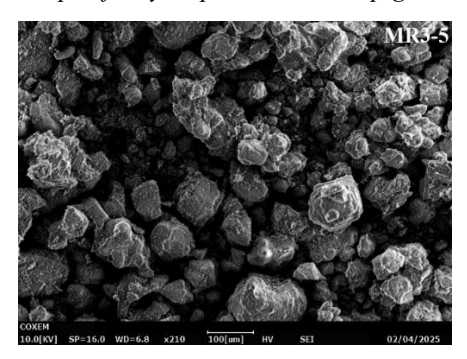
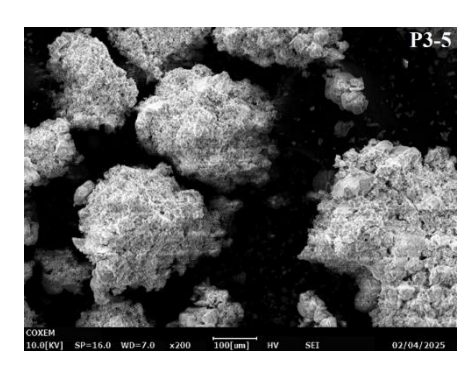


Figure 10. SEM images of samples M3-5 and MR3-5 fired at 1350 °C



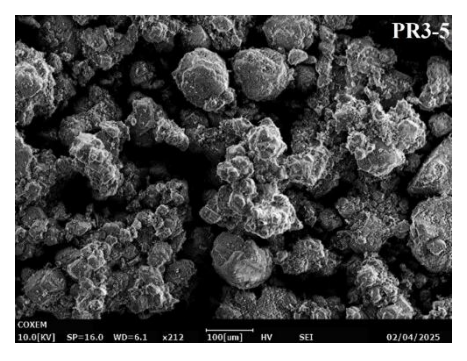


Figure 11. SEM images of samples P3-5 and PR3-5 fired at 1400 °C

Scanning electron microscopy

The samples were analyzed by scanning electron microscopy (SEM) at 10.00 kV accelerating voltage using an IEM11 microscope, Inovenso INC, (Turkey). SEM analysis (Figs. 10 and 11) shows that the particles in the pigments tend to form clusters larger in the pigments fired at a higher temperature -1400 °C.

CONCLUSIONS

The main phases in the synthesized ceramic pigments were identified by X-ray diffraction (XRD): corundum (Al₂O₃), cristobalite (SiO₂), mullite (3Al₂O₃.2SiO₂), and nickel spinel (NiAl₂O₄). It is noteworthy that the main crystalline phase in all compositions is corundum, with nickel spinel also forming everywhere. These two phases are resistant and stable at high temperatures, which also determines the good properties of the synthesized pigments. This conclusion is also confirmed by the hot-stage analysis. The results of hot-stage microscopy of batches obtained from pure raw materials show that up to 1400 °C, the shape of the samples remains constant, without visible changes. Extremely high thermal stability of the samples is observed. The size of the crystals in the main phases was determined. It varies from 13 nm (MR3-5) to 55 nm (PR3-5). The color characteristics of the synthesized pigments were determined spectrally, the pigment with composition M3-5 having the best indicators: (a) = -15.2 and (b) = -4.9.

Acknowledgement: The financial support of this work by the Bulgarian Ministry of Education and Science, National Research Fund under contract number KP-06-N87/14 is gratefully acknowledged.

REFERENCES

- 1. Ts. Ibreva, Ts. Dimitrov *et al.*, *Bulg. Chem. Commun.*, **50**, 31 (2018).
- 2. F. A. Cotton, Modern Inorganic Chemistry, Moscow, 1979 (in Russian).
- 3. A. Wells, Structural Inorganic Chemistry, Mir, Moscow, 1987 (in Russian).
- 4. A. A. Grinberg, Introduction to the Chemistry of Complex Compounds, Chemistry, Leningrad, 1971 (in Russian).
- 5. Y. Wang et al., Solid State Sci., 135, 107088 (2023).
- 6. K. L. Patrocínio et al., Ceramics International, **50**, 31955 (2024).
- 7. F. Yovkova et al., Annual of Assen Zlatarov University, XLVIII, 2603 (2019).
- 8. M. Javanmardi et al., Trans. Nonferrous Met. Soc. China, **26**, 2910 (2016).
- 9. R.M. Khattab *et al.*, *Materials Chemistry and Physics*, **281**, 125880 (2022).
- 10. B. S. Cherepanov *et al.*, Glass and ceramics, 1983 (in Russian).
- 11. M. Troyan, Glass and Ceramics, 1988 (in Russian).

Adhesive bond between dentin and CROWNTEC with different printing orientations

M. Dimova-Gabrovska¹, Y. Brusarska¹, E. Kirilova^{2*}, S. Yanakiev³, Z. Tomova⁴, S. Rangelov¹

Received: May 02, 2025; Revised: June 06, 2025

In prosthetic dental medicine, the success of treatment with fixed restorations depends on numerous key factors. Among them, achieving a strong and durable adhesive bond between the material and natural tooth tissues is of paramount importance for the longevity and effectiveness of any restoration. The present study aims to investigate, in a laboratory setting, the adhesive bond between the composite material CROWNTEC and the dentin of natural teeth using the RelyX Unicem adhesive system. The test specimens were evenly distributed into three groups according to the angle of the normal vector to the surface of the printing platform (angles of 0°, 45°, and 90°). The samples were bonded to previously prepared dentin plates. A universal testing machine MultiTest 2.5-i was used to conduct the tests with a shear bond strength testing fixture. From the conducted study, we established that the highest shear bond strength was recorded in group C - 3.000 MPa, followed by group A with a value of 2.4 MPa and group B with 2.0 MPa. In conclusion, it can be summarized that the best adhesive bond between the material and the dentin surface forms when the material layers of the test specimens are positioned horizontally during the printing, while the weakest adhesive bond forms when the material layers intersect at a 45° angle.

Keywords: additive manufacturing; adhesive bond; composites; shear bond strength.

INTRODUCTION

Technological advancements worldwide have a direct impact on treatment protocols in dental medicine [1-3]. Prosthetic dental medicine, a specialty fundamentally aimed at improving both function and aesthetics, is at the forefront of adopting innovative technologies [4-7].

Computer-Aided Design and Computer-Aided Manufacturing (CAD/CAM) is a technology created in the 1970s that has been repeatedly proven for the purposes of prosthetic dental medicine [8-12]. The system is based on digital scanning and designing of a virtual CAD model, followed by the construction of actual prosthetic restorations (CAM) [13-18]. Digital modeling is also the first step in 3D printing technology—a process increasingly used in the fabrication of removable and fixed prosthetic restorations [19-22]. "Additive manufacturing" is a term frequently encountered in scientific literature to denote this technology. The meaning of the term refers to the essence of the process—building a 3D model through layer-by-layer addition of material [8, 23, 24].

Materials used for additive manufacturing of prosthetic restorations must possess mechanical and

physical properties close to those of the tissues they are meant to replace [25-28].

The specific needs of permanent restorations in prosthetic dentistry also necessitate the development of hybrid materials suitable for the additive manufacturing of permanent fixed restorations [5, 8, 19, 29]. Such a material was developed in 2022 by the company SAREMCO (Switzerland)—a light-curing hybrid composite with embedded ceramic particles in its composition: CROWNTEC (SAREMCO, Switzerland) [30, 31].

A crucial factor determining the success of any treatment involving crowns or bridgework is the adhesive bond between the restorative material and the dentin of natural teeth through the use of cement [14, 32].

The effectiveness and strength of adhesion relate to the cement's ability to bond the dentin surface to the surface of the material, with the force required to break this bond referred to as shear bond strength [25, 26, 33]. Shear bond strength is a mechanical parameter that measures the loads needed to deform or destroy materials under the action of opposing forces. The test specimens are two objects adhesively bonded together [25].

¹Department of Prosthetic Dental Medicine, Faculty of Dental Medicine, Medical University – Sofia, 1 Sv. Georgi Sofiyski Str., Sofia 1431, Bulgaria

²Institute of Chemical Engineering, Bulgarian Academy of Sciences, Acad. G. Bontchev, Str., Bl. 103, 1113 Sofia, Bulgaria

³Medical College "Yordanka Filaretova" – Sofia, Medical University – Sofia, 3 Yordanka Filaretova Str., Sofia 1431, Bulgaria

⁴Department of Prosthetic Dental Medicine, Faculty of Dental Medicine, Medical University -Plovdiv, Hr. Botev Blvd. 3, 4000, Bulgaria

^{*} To whom all correspondence should be sent: E-mail: elisavetakirilova.iche.bas@gmail.com

A key requirement for dental cements is their ability to create equally effective bonds both on enamel and dentin surfaces [30]. The structure of dentin in natural teeth varies greatly over time, influenced by factors such as the patient's age and the number and size of dentinal tubules, while the enamel surface remains homogeneous [35, 36]. Other factors affecting good adhesion between tooth dentin and restorative materials include excessive moisture or over-drying of the tooth after etching with phosphoric acid [37, 38].

The bond between dental structures and adhesive cements is achieved by the replacement of minerals from the hard-dental tissues with monomer molecules from dental cements [39].

Each type of material requires specific preparation of both the dentin surface and the material surface [33, 40-43]. Regarding resin-based materials such as CROWNTEC (SAREMCO, Switzerland), surface preparation usually involves sandblasting with aluminum oxide or chemical treatment with hydrofluoric acid followed by the application of a silane coupling agent. Hydrofluoric acid creates micro-retentions on the surface, thus increasing the bonding area between the material and the cement. This is also the standard protocol for glass-ceramic surface treatment, although for lithium disilicate, hydrofluoric acid application is not recommended above 4.9% concentration [15, 17, 44, 45].

The adhesion of metal-free restorations is achieved using composite cements, which may be self-curing, light-curing, or dual-curing. Composite cements form a strong chemical bond with natural dental structures, contributing to high shear bond strength [17, 46].

The adhesive cement 3MTM - RelyXTM U200 is divided into two components that are mixed immediately before use. The base paste contains methacrylate monomers with phosphoric acid groups, methacrylate monomers, silanized fillers, initiator components, and stabilizers. The catalyst paste also contains methacrylate monomers, alkaline fillers, silanized fillers, initiator components, stabilizers, and pigments. The cement is dual-curing, meaning the reaction starts either under light exposure or through the chemical reaction of the initiator [47]. Literature data indicate that this composite cement adheres better to tooth enamel than to dentin [47-50].

According to the scientific literature, enamel tissue exhibits better adhesion through various

composite cements, while the strength of adhesive bonding to dentin remains a challenge [30, 34, 51].

AIM

The aim of the present study is to investigate, in a laboratory setting, the adhesive bond between test specimens produced from the composite material CROWNTEC (SAREMCO, Switzerland) and the dentin of natural teeth, using the RelyX Unicem (3M) adhesive system.

Null Hypothesis (H_0): Shear bond strength is comparable across all specimens' groups.

Alternative Hypothesis (H_1) : Shear bond strength varies significantly among specimens' groups.

MATERIALS AND METHODS

For the purposes of this study, 45 test specimens were fabricated using a NextDent 5100 3D printer (NextDent, USA), based on digital light processing (DLP) technology, from the composite material CROWNTEC (SAREMCO, Switzerland), which contains ceramic fillers.

The specialized software "3D Sprint" was used for the design of the digital prototypes.

The samples were divided into three groups based on their spatial orientation during printing. The normal vector to the surface formed an angle with the printing platform surface as follows: 0° for Group A; 45° for Group B; and 90° for Group C.

The different spatial orientations during the production of the test specimens led to structural differences corresponding to the angles of 0°, 45°, and 90°.

Cylindrical test specimens were printed with these orientations, each with dimensions of 9 mm in diameter and 4 mm in height (Fig. 1A). After printing, each specimen was cleaned by soaking in 96% alcohol and brushing to remove any excess material. Final polymerization was carried out using a UV post-curing unit, the LC-3DPrint Box (NextDent, USA), for 30 min (Fig. 1B).

For the test procedure, dentin plates (Fig. 2) with a thickness of 2.5 mm were prepared from natural extracted teeth with intact crowns, using a microtome. The dentin plates were embedded in epoxy resin.

The bonding of the test specimens to the dentin blocks was carried out using the composite cement RelyX Unicem (3M) according to the following protocol:





.

Figure 1. Printing and post-curing of the test specimens.



Figure 2. Dentin plates.

- The surface of the specimens was abraded by sandblasting with aluminum oxide (Al₂O₃) particles with a size of 110 µm.
- The specimens were cleaned with alcohol and dried.
 - The dentin surface was rinsed and air-dried.
- The required amount of composite cement was applied onto the prepared specimens.
- The specimens were initially fixed to the dentin blocks.
- A universal testing machine for physical-mechanical testing (MultiTest 2.5-i) was used to apply a weight of 50 N during fixation (Fig. 3).
- After the application of the weight to the specimens fixed to the dentin blocks, light polymerization was performed for 5 sec to achieve primary curing and to remove the excess material.
- Final light polymerization was applied for 20 sec.

The shear bond strength tests were conducted using a universal testing machine for physical-mechanical testing (MultiTest 2.5-i) (Fig. 4). The device consists of a monolithic construction with an integrated lead screw drive, to which a strain gauge load cell is attached, measuring the force applied at one end. Depending on the attachments used, the



Figure 3. Fixation by applying a weight of 50 N.

system allows testing of materials under tension, compression, bending, and shear.



Figure 4. Shear bond strength testing using the MultiTest 2.5-i universal testing machine.

The attachment used for shear bond strength testing consists of two metal plates sliding against each other in a single plane. One plate serves as a "frame" with a pentagon-shaped opening, while the other, known as the "blade," is beveled. The test specimens are fixed at three support points within the stationary frame, with the plane of the cemented bond positioned precisely at the boundary between the "blade" and the "frame" (i.e., between the two metal plates). The movement of the blade is pre-

programmed; during the test, the blade encounters a resistive force, which is continuously and automatically recorded until failure of the material occurs.

Statistical methods used

- Descriptive statistics:
- Mean (Average) a measure of central tendency;
- Median a measure of the middle value;
- Standard deviation (SD) a measure of dispersion;
- Lower control limit (LCL) and upper control limit (UCL) – the boundaries within which the true mean of the population lies;
- Absolute values (N) a measure of the number of cases;
- Minimum and maximum values the smallest and largest observed measurements.
 - o Hypothesis testing:
- Nonparametric test for differences among "k" independent samples (Kruskal-Wallis test);
- Post-hoc test to determine between which of the "k" independent groups the significant differences occur.

All hypothesis testing was performed with a significance level (alpha) set at 5%.

The statistical analyses were carried out using IBM SPSS Statistics 26, and graphical representations were prepared with Excel 2010.

RESULTS

The present study included a total of 45 test specimens, evenly distributed into three groups (A, B, and C), according to the angle of the normal vector to the surface of the printing platform (angles of 0°, 45°, and 90°, respectively). The shear bond strength of the specimens was measured in megapascals (MPa).

The measured average shear bond strength of the tested samples was 1.293 MPa, with a standard deviation of ± 0.951 MPa.

The lowest recorded shear bond strength was 0.100 MPa, and the highest was 3.000 MPa, both values observed in the specimens from Group C. In Group A, the highest recorded value was 2.400 MPa, while in Group B it was 2.000 MPa.

Half of the specimens had a shear bond strength below 1.100 MPa, while the other half exhibited higher values (Table 1).

Upon examining and comparing the shear bond strength among the different groups of specimens, the results showed that the highest shear bond strength was observed in Group C (1.840 MPa ± 1.093 MPa), while the lowest was recorded in Group B (0.780 MPa ± 0.718 MPa). Group A exhibited a mean shear bond strength of 1.260 MPa, with a standard deviation of ± 0.728 MPa.

Table 1. Summary of the statistical characteristics of the sample. Unit of measurement: MPa

	Shear bond
Mean	1.293
Median	1.100
Std. dev.	0.951
Min	0.100
Max	3.000
LCL/UCL	1.015/1.571
№	45

The differences between the groups are graphically presented (Fig. 5).

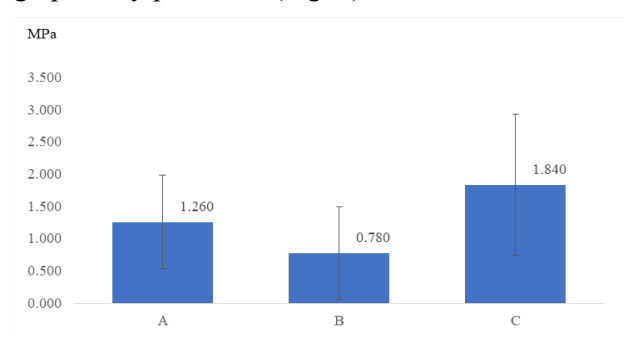


Figure 5. Differences in shear bond strength between the groups (MPa).

Table 2. Results from the test of differences in shear bond strength between the three groups.

Test group	Chars.	Groups under test			
Char. under test		A	В	C	
Shear bond	Mean	1.260 AB	0.780 A	1.840 ^B	
	SD	±0.728	±0.718	±1.093	
	N	15	15	15	
Kruskal- Wallis test	P-value	P=0.018			

The significance level obtained from the test [p = 1.8%] is lower than the accepted risk of error of 5%. Therefore, the alternative hypothesis is accepted, stating that there is a statistically significant difference in the shear bond strength of the test specimens between the groups. To determine more specifically between which groups the differences are significant, a post-hoc test (Least Significant Difference test) was performed. This analysis revealed that a significant difference exists between the shear bond strength of Group B and Group C, with the strength being higher in favor of the specimens from Group C. This conclusion can be stated with 95% confidence. The difference between

Groups A and C is also very close to being statistically significant, but it reaches significance only at a 10% risk of error.

DISCUSSION

The present study clearly demonstrates a marked dependence between the orientation of the test specimens relative to the printing platform and their shear bond strength. Dividing the specimens into three groups based on the angle of the normal vector (0°, 45°, and 90°) allowed for tracking the influence of the printing angle on the mechanical properties of the material.

The highest mean shear bond strength was recorded in Group C (90°) - 1.840 MPa ±1.093 MPa. This result is likely due to the horizontal orientation of the structural layers located at the surface bonded to the dentin blocks. In Group B (45°) , the lowest mean shear bond strength was observed - 0.780 MPa ±0.718 MPa, which may be explained by the less favorable arrangement of the material layers at a 45° angle, leading to a weaker adhesive bond. Group A (0°) demonstrated an intermediate mean shear strength - 1.260 MPa ±0.728 MPa - suggesting that a vertical spatial orientation of the layers is the least favorable for achieving an effective adhesive bond.

Both the lowest (0.100 MPa) and highest (3.000 MPa) individual values among all tested specimens were recorded in Group C. This variability may be attributed to technological factors during the manufacturing process or the presence of microdefects in the material's structure.

The result of the hypothesis test (p = 1.8%) is below the accepted significance level of 5%, which necessitates the rejection of the null hypothesis and acceptance of the alternative hypothesis—that is, there is a statistically significant difference in shear bond strength among the groups. This difference was specifically established between Groups B and C, in favor of Group C, indicating that specimens with horizontally oriented layers demonstrate superior mechanical properties, with 95% confidence. Although a difference between Groups A and C also exists, it would only reach statistical significance at a risk level higher than 10%.

The results of the laboratory study regarding the influence of this spatial orientation during printing on the shear strength are in accordance with those reported by Khanlar *et al.* [52] The results of their study confirm that the horizontal orientation of the layer (90°) leads to a higher shear strength, which corresponds to the values observed in Group C at the core of our study. In [52], lower values for shear strength are observed at angles of 0° and 45°, confirming our hypothesis that the structure of the

layer of the material is a key factor for the adhesive bond.

In the review article by Liang *et al.* [53] regarding the influence of parameters on printing, including spatial orientation, the authors emphasized that optimization of the layers is of key importance to achieve better mechanical quality of the material, which confirms the conclusion of the study.

CONCLUSION

The spatial orientation of the test specimens relative to the printing platform of the 3D printer has an influence on the mechanical properties of the material, particularly on shear bond strength. The results from the conducted laboratory tests support the recommendation that, during the digital design and fabrication of constructions made from the CROWNTEC material (SAREMCO, Switzerland), zones subjected to high mechanical loads should have a horizontally oriented structural layer arrangement.

The long-term clinical success of permanent fixed prosthetic restorations is directly dependent on the quality of the adhesive bond between the restorations and the dental tissues. Effective adhesion not only contributes to the stability and durability of prosthetic structures but also reduces the risk of micro-movements and the development of secondary caries, thereby ensuring long-term oral health for patients.

Acknowledgement: The data presented in this study are subject to investigation in the Research Project Competition "Grant-2024," entry number 132/29.05.2024, at the Medical University - Sofia.

REFERENCES

- D. Shopova, D. Bakova, S. Yordanova, M. Yordanova, T. Uzunov, *Appl. Sci.*, 13, 4335 (2023).
- Z. Tomova, Y. Zhekov, G. Alexandrov, A. Vlahova, E. Vasileva, *Aust. Dent. J.*, 68, 294 (2023).
- 3. M. Dimitrova, A. Vlahova, R. Kazakova, B. Chuchulska, M. Urumova, *J. IMAB Annu. Proc.* (Sci. Pap.), **29**, 4939 (2023).
- 4. H. Hubálková, I. Linetskiy, *Prague Med. Rep.*, **107(2)**, 149 (2006).
- 5. M. Dimova-Gabrovska, Y. Brusarska, Sci. Works Union Sci. Bulg.-Plovdiv Ser. G Med. Pharm. Dent. Med., XXXI, 118 (2024).
- M. Dimova-Gabrovska, T. Uzunov, A. Gusiyska, D. Shopova, I. Taneva, I. Gerdzhikov, S. Rangelov, Appl. Sci., 14(9), 3923 (2024).
- 7. J. P. M. Tribst, G. K. R. Pereira, C. J. Kleverlaan, *J. Clin. Med.*, **13(5)**, 1225 (2024).
- 8. A. Vlahova, S. Zlatev, CAD/CAM technologies in prosthetic dentistry, 2021.

- 9. W. Grzebieluch, P. Kowalewski, D. Grygier, M. Rutkowska-Gorczyca, M. Kozakiewicz, K. Jurczyszyn, *Materials*, **14(17)**, 4919 (2021).
- S. Yanakiev, S. Velikov, N. Kostova-Kamburova, M. Moskova, E. Micheva, *Health Sci.*, 1–2(049–050), 195 (2023).
- S. Yanakiev, S. Velikov, N. Kostova-Kamburova, M. Moskova, E. Micheva, *Health Sci.*, 3–4(047–048), 48 (2022).
- 12. M. Dimitrova, M. Corsalini, R. Kazakova, A. Vlahova, G. Barile, F. Dell'Olio, Z. Tomova, S. Kazakov, S. Capodiferro, *J. Compos. Sci.*, **6(7)**, 201 (2022).
- 13. G. Vico, A. B. Rossi, M. R. Rodrigues, A. L. B. Almeida, A. D. Costa, A. F. Silva, *Oral Implantol.* (*Rome*), **1(3–4)**, 104 (2008).
- 14. M. J. Calheiros-Lobo, T. Vieira, R. Carbas, L. F. M. da Silva, T. Pinho, *Materials*, **16(8)**, 2996 (2023).
- A. Wiegand, L. Stucki, R. Hoffmann, T. Attin, B. Stawarczyk, Clin. Oral Investig., 19(8), 2007 (2015).
- N. Krajangta, A. Klaisiri, S. Leelaponglit, N. Intralawan, P. Tiansuwan, N. Pisethsalasai, *Dent. Mater. J.*, 43(3), 386 (2024).
- 17. A. Mine, M. K. Sato, T. O. Honda, N. Ueda, S. Ueno, *J. Dent. Sci. Rev.*, **55(1)**, 41 (2019).
- 18. P. Suksuphan, N. Krajangta, P. P. Didron, T. Wasanapiarnpong, T. Rakmanee, *J. Prosthodont. Res.*, **68**(2), 23 (2023).
- I. Katreva, T. Dikova, M. Abadzhiev, T. Tonchev, D. Dzhendov, M. Simov, S. Angelova, D. Pavlova, M. Doychinova, Scr. Sci. Med. Dent., 2(1), 7 (2016).
- B. Yang, S. Wang, G. Wang, X. Yang, J. Mech. Behav. Biomed. Mater., 124, 104859 (2021).
- 21. H. Cai, X. Xu, X. Lu, M. Zhao, Q. Jia, H.-B. Jiang, J.-S. Kwon, *Polymers (Basel)*, **15(10)**, 2405 (2023).
- 22. D. Shopova, M. Yordanova, S. Yordanova, *Eur. J. Dent.*, **16**, 815 (2022).
- 23. I. Taneva, 3D-Printed Splints for the Prevention of Complications in Bruxism Experimental and Clinical Study, Sofia, 2022.
- 24. D. Shopova, M. Yordanova, S. Yordanova, *Open Access Maced. J. Med. Sci.*, **10**, 6 (2022).
- 25. I. Anastassov, Y. Yoshida, T. Dragev, Dental Materials, 2013.
- 26. J. Manappallil, Basic Dental Materials, 2015.
- 27. O. E. Pecho, R. Ghinea, E. A. N. do Amaral, J. C. Cardona, A. Della Bona, M. M. Pérez, *Dental Materials*, **32(5)**, e105 (2016).
- 28. X. Z. Liu, P. J. Lu, Y. Wang, *J. Peking Univ. Health Sci.*, **40(6)**, 654 (2008).
- 29. M. Dimitrova, A. Vlahova, Y. Kalachev, S. Zlatev, R. Kazakova, S. Capodiferro, *Polymers (Basel)*, **15(23)**, 4525 (2023).
- 30. Permanent 3D printed crowns CROWNTEC, https://saremco.ch/en/products/crowntec.
- 31. Instruction for Use I saremco print CROWNTEC I US-version,

- https://saremco.ch/en/pages/document/gebrauchsan weisungen.
- 32. C. D'Arcangelo, L. Vanini, M. Casinelli, M. Frascaria, F. De Angelis, M. Vadini, M. D'Amario, *Compend. Contin. Educ. Dent.*, **36(8)**, 570 (2015).
- 33. R. Vladova, T. Petrova, E. Kirilova, B. Boyadjiev, A. Apostolov, W. Becker, A. Moravski, *Acta Polytechnica CTU Proceedings*, **50**, 94 (2024).
- 34. J. Perdigão, J. Dent. Sci. Rev., 56(1), 190 (2020).
- 35. D. Damyanova, I. Georgieva, *Am. J. Eng. Res.*, **6**, 130 (2017).
- 36. I. Georgieva, D. Damyanova, M. Miteva, *Int. J. Sci. Res.*, **6**, 566 (2017).
- 37. D. McLean, E. Meyers, V. Guillory, K. Vandewalle, *Oper. Dent.*, **40(4)**, 410 (2015).
- 38. D. Damyanova, Int. J. Eng. Res. Appl., 6, 68 (2016).
- 39. B. Van Meerbeek, M. Yoshida, H. Inoue, H. Van Landuyt, F. Fredrickson, *Oper. Dent.*, **28(3)**, 215(2003).
- 40. Y. Nagasawa, Y. Eda, H. Shigeta, M. Ferrari, H. Nakajima, Y. Hibino, *Odontology*, **110(1)**, 70 (2022).
- 41. Z. Zhao, Q. Wang, J. Zhao, B. Zhao, Z. Ma, C. Zhang, Front. Mater., 7, 615225 (2021).
- 42. T. Petrova, Bulg. Chem. Commun., **55(3)**, 349 (2023).
- 43. D. Damyanova, R. Andreeva-Borisova, *Int. J. Public Health Sci.*, **10**, 241 (2021).
- 44. S. Duma, N. Ilie, *J. Funct. Biomater.*, **13(4)**, 217 (2022).
- 45. A. Chin, M. Ikeda, T. Takagaki, T. Nikaido, A Sadr, Y. Shimada, J. Tagami, *Materials*, **14(22)**, 7058 (2021).
- A. Heboyan, A. Vardanyan, M.I. Karobari, A. Marya,
 T. Avagyan, H. Tebyaniyan, M. Mustafa, D. Rokaya,
 A. Avetisyan, *Molecules*, 28(4), 1619 (2023).
- 47. Instruction for Use, RelyX U200 Self-Adhesive Resin Cement, https://multimedia.3m.com/mws/media/1278181O/3 m-relyx-u200-and-ultimate-clicker-easy-use-guide-for-zirconia-and-glass-ceramic-crowns.pdf
- 48. J. Fehrenbach, E. A. Münchow, C. P. Isolan, L. P. Brondani, C. D. Bergoli, *Int. J. Adhes. Adhes.*, **107**, 102863 (2021).
- 49. R. F. Rodrigues, C. M. Ramos, P. A. S. Francisconi, A. Flávia, S. Borges, *J. Prosthet. Dent.*, **113(3)**, 220 (2015)
- 50. T. Rojpaibool, C. Leevailoj, *J. Prosthodont.*, **26(2)**, 141 (2017).
- 51. M. Le, E. Papia, C. Larsson, *BDJ Open*, **10(1)**, 44 (2024).
- 52. L. Nasiry Khanlar, M. Revilla-León, A.B. Barmak, M. Ikeda, Q. Alsandi, J. Tagami, A. Zandinejad, *J. Prosthet. Dent.*, **129(5)**, 788 (2023).
- 53. X. Liang, B. Yu, Y. Dai, Y. Wang, M. Hu, H.-J. Zhong, J. He, *Materials*, **18(10)**, 2202 (2025).

Calcium carbonate nanoparticles as a filler for gelatin-based biofilms: preparation, characterization and properties

D. S. Kiryakova^{1*}, A. S. Ilieva², G. R. Kolchakova¹

¹Department of Materials Science, Burgas State University "Prof. Dr. Assen Zlatarov", 1, Y. Yakimov Str., Burgas 8010, Bulgaria

Received: May 02, 2025; Revised: May 14, 2025

Gelatin-based biofilms filled with calcium carbonate nanoparticles (NPs), synthesized from *Rapana Venosa* shells, were prepared by the solvent casting technique. The content of NPs in the films ranged from 0.5 to 5.0%. The water content, water absorption, solubility in water, tensile properties, and biodegradation were investigated and compared with those of the control gelatin film. Results showed that the addition of 5.0% of calcium carbonate nanofiller reduces the solubility in water and water absorption of the films by 58% and 64%, respectively. In contrast to the initial gelatin film, the incorporation of CaCO₃ NPs into the materials, regardless of the amount, increases the values of the elongation at break. The reinforcing effect of the nanofiller on the gelatin samples was manifested when 5.0% of NPs were added. These materials have a maximum tensile strength and Young's modulus of 7.16 and 70.3 MPa, respectively. It was proven that the NPs make the films more resistant and less susceptible to degradation after exposure to the surface of compost soil for a period of 6 months and could be used to extend the service life of biofilms.

Keywords: calcium carbonate nanoparticles, gelatin, biofilms, solution casting, properties

INTRODUCTION

Gelatin films, as thin-layer biopolymer materials, have attracted significant attention, especially in the fields of food packaging, pharmaceuticals, and biomedical engineering [1–3]. These films exhibit advantageous properties such as biodegradability and biocompatibility, however, pure gelatin films have insufficient mechanical strength, high moisture sensitivity, and limited barrier properties, which restrict their practical applications [4]. To overcome these limitations, researchers incorporate various nanofillers into gelatin matrices to improve their functional properties [5].

Nanocellulose significantly improves the mechanical properties of the gelatin films, enhancing their tensile strength and elasticity [6]. However, its hydrophilic nature can lead to increased water absorption, which is undesirable for applications requiring moisture resistance [7]. The layered structure of nanoclays gives them exceptional barrier properties that significantly reduce the permeability of biopolymer films [8]. The addition of metal and metal oxide nanoparticles into gelatin matrices is primarily due to their antimicrobial and UVblocking properties [9–11]. They effectively inhibit microbial growth, extending the shelf life of food

products when used in packaging applications. A disadvantage of their use is the concern about potential toxicity and migration into food products [11].

Nano calcium carbonate, extracted from various waste materials, is a sustainable option for incorporation into gelatin matrices. Industrial byproducts such as eggshells, mussels, and limestone waste serve as rich sources of calcium carbonate [12–14]. The small particle size and high surface area [13] make it an attractive option for enhancing the mechanical properties of gelatin-based materials. Additionally, nano calcium carbonate has been shown to have antimicrobial properties [15], which could further extend the shelf life of food products when used in packaging.

The aim of the present study is to prepare, characterize and determine the main properties of plasticized gelatin biofilms filled with calcium carbonate NPs. For this purpose, films combining gelatin, calcium carbonate nanofiller in amounts from 0.5 to 5.0% and glycerol as a plasticizer were obtained by the solution casting method. The properties of the biofilms were evaluated in terms of the influence of the additive on them and compared with those of a control film of pure gelatin.

²Department of Chemical Technologies, Burgas State University "Prof. Dr. Assen Zlatarov", 1, Y. Yakimov Str., Burgas 8010, Bulgaria

^{*} To whom all correspondence should be sent: E-mail: \(dskiryakova@abv.bg \)

EXPERIMENTAL

Materials

Animal gelatin powder (type A) was purchased from the local market in Burgas, Bulgaria. Glycerol $C_3H_8O_3$ (molecular weight 92.10 g/mol, density 1.26 g/cm³), used as a plasticizer of the films, was purchased from Marvin Ltd, Dimitrovgrad, without further purification. Biogenic calcium carbonate with a particle size of \sim 40 nm, synthesized from *Rapana Venosa* shells, was provided by the Laboratory of Aquaculture and Biotechnology, Prof. Assen Zlatarov University. Distilled water was used as a solvent for preparing filmogenic solutions.

Film preparation

The gelatin-CaCO₃ NPs -based films were obtained by the traditional solution casting technique. Distilled water (40 mL) was mixed with 4 g of gelatin for each film. The resulting solutions were heated at 80°C for 15 min under stirring. 1.5 g of glycerol plasticizer (37.5% by weight of gelatin basis) was added, and the resulting mixtures were stirred for additional 5 min at the same temperature. Then 0.5, 1.0, 2.0, 3.0, and 5.0% of CaCO₃ NPs (based on total gelatin in dry state) were added to the mixtures and sonicated using a Branson 8510 ultrasonication bath for 30 min. The film-making solutions containing the indicated amounts of the nanofiller were placed into acrylic mould dishes (diameter: ~130 mm), kept at room temperature for 24 h, and dried in an oven at 40°C for a day to dry up properly. After drying, mould dishes were kept at room temperature for 24 h. Before being characterized, the dried films were removed from the dishes and kept at room temperature for a week. Specimens prepared were designated as control gelatin (G) film, G-0.5 CaCO₃, G-1.0 CaCO₃, G-2.0 CaCO₃, G-3.0 CaCO₃, and G-5.0 CaCO₃ according to the content of CaCO₃ NPs in the biofilms.

Characterization of the gelatin-based biofilms

Thickness

A micrometer thickness gauge was used to measure each gelatin biofilm sample's thickness with a 0.0001 mm precision. The average value of the thickness of each film measured at five different locations was taken as the thickness.

• Water content

The biofilm samples were cut into 20×20 mm pieces, and their initial weight (W_0 , g) was measured. They were then dried in an oven at 70°C for 24 h and reweighed (W_f , g). To calculate the water content (WC, %), expressed as a percentage, the following formula was used:

Water content (%) =
$$[(W_o - W_f)/W_f] \times 100$$
 (1)

• Water absorption

Initially, gelatin-biofilm samples were dried in an oven at a temperature of 70°C for a day to get their initial weight (W_0 , g). The samples were then immersed in distilled water and kept at room temperature for 210 min. For each measurement, specimens were removed from the water, wiped off, and reweighed (W_f , g) to a precision of 0.0001 g. The following Eq. (2) was used to determine the water absorption (WA, %):

Water absorption (%) =
$$[(W_f - W_g)/W_g] \times 100$$
 (2)

• Water solubility

To calculate the water solubility (WS, %) of the gelatin-based biofilms, 20×20 mm sizes of the samples were dried (70° C, 24 h) and weighed (W_{\circ} , g). Then each sample was immersed in distilled water and stored at a temperature of $22\pm3^{\circ}$ C for a period of 24 h. The residual insoluble part of the films was removed, dried in an oven for 24 h at 70° C, and weighed again ($W_{\rm f}$, g). Eq. (3) was used to calculate the G-CaCO₃ NPs biofilm's solubility in water:

Water solubility (%) =
$$[(W_0 - W_f)/W_0] \times 100$$
 (3)

• Tensile properties

The tensile strength, elongation at break, and Young's modulus of control G film and G-CaCO₃ NPs biofilms were determined at room temperature according to EN ISO 50527-1 using a universal testing machine dynamometer INSTRON 4203, England. The grip distance was set at 25 mm, and a crosshead speed of 50 mm/min was applied. The samples' thickness was measured prior to each test.

• Test for biodegradability

To assess the biodegradability of gelatin-based films with CaCO₃ NPs, from each film samples with dimensions of length 50 mm, width 4 mm, and gauge length 25 mm were cut. Then the samples were weighed (W_0 , g) and exposed to the surface of a compost soil for a period of 6 months. The compost soil media used had pH of 5.5-6.5 and electrical conductivity of 40 mS/m. After 6 months, the biofilms were removed from the compost soil and cleaned before being again weighed (W_f , g). The biofilms' biodegradability, or percentage weight loss, was calculated using Eq. (4):

Weight loss (%) =
$$\left[\left(W_{0} - W_{f} \right) / W_{0} \right] \times 100$$
 (4)

• Visual appearance of the films

The obtained dried control and gelatin-CaCO₃ NPs-based films after removal from the mould dishes were placed on a black base and photographed with a phone camera. To visually monitor the degradation of the samples before and

after exposure in a compost soil environment, the films were photographed again. All the photos taken, with a resolution of 739×1600 pixels, are reported in chronological order during the experiment in the Results and Discussion section.

• Hardness by Shore

The Shore A hardness of the resulting gelatinbased biofilms was determined on an apparatus "Stendal", Germany scale A and ASTM D-2240.

RESULTS AND DISCUSSION

*Visual appearance of gelatin-CaCO*₃ *NPs biofilms*

The films obtained by casting from aqueous solutions of mixtures of gelatin, glycerol (37.5%), and calcium carbonate nanoparticles have good filmogenicity and are easily removed from the casting moulds. They are homogeneous, with a smooth surface and no visible bubbles or air inclusions (see Fig. 1).

As can be seen, the control gelatin film has high transparency and a pale yellow hue due to the gelatin. At a low concentration of NPs (0.5%), the dispersion of particles with a size of ~ 40 nm is good enough to obtain transparent films. However, the higher the amount of CaCO₃ NPs in the gelatin biofilms, the lower is the transparency of the samples. For example, the transparency of gelatin samples from G-1.0 CaCO₃ is slightly affected, with G-2.0 CaCO₃ being visually more opaque due to the higher concentration of nanoparticles which are

white in color. The use of nano CaCO₃ in higher amounts of 3.0 and 5.0% significantly increases the opacity of films compared to the control G film.

Thickness of gelatin-CaCO₃ NPs biofilms

Detailed data on the change in the thickness of cast gelatin films by the amount of $CaCO_3$ nanofiller are shown in Table 1. It is known that the thickness of G films is affected and can be increased by increasing the amount of NPs added to them [16, 17]. The data in the table confirm that compared to the control G film (356 μ m), the thickness of the filled G film is greater and increases from 358 μ m (for G-0.5 CaCO₃) to 382 μ m (for G-5.0 CaCO₃). A similar increase in the thickness of gelatin-based biofilms when using CuS or WO₃ nanoparticles has been found by other authors [18, 19].

Water content, water solubility and water absorption of gelatin-CaCO₃ NPs biofilms

Although gelatin films possess sufficiently good mechanical and barrier properties, they are sensitive to the action of moisture. This limits their use, especially in applications where water resistance and water insolubility are required. Therefore, to characterize the biofilms obtained with CaCO₃ NPs, the following indicators; moisture content, water absorption and water solubility were studied and compared with the same for the control film without additive.

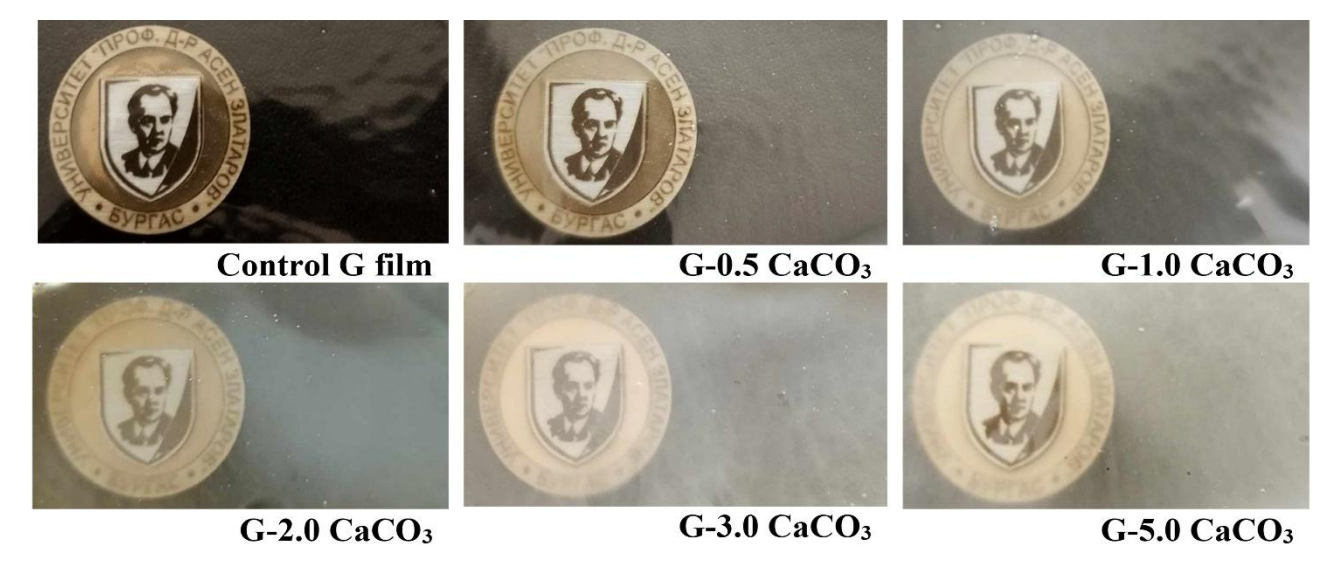


Fig. 1. Photographs of gelatin-based films with different contents of calcium carbonate NPs

Table 1. Thickness, water content, water solubility, Shore hardness and biodegradation of gelatin-based biofilms with calcium carbonate NPs.

Films	Thickness, µm	Water content,	Water solubility, %	Shore hardness	Biodegradation, %
Control G film	356	0.376	5.697	74.3	8.537
G-0.5 CaCO ₃	358	0.353	4.672	74.7	8.402
G-1.0 CaCO ₃	361	0.308	4.458	74.5	8.371
G-2.0 CaCO ₃	366	0.285	4.354	75.0	8.142
G-3.0 CaCO ₃	370	0.245	3.662	74.9	6.564
G-5.0 CaCO ₃	382	0.212	2.402	82.0	4.990

Table 1 shows the calculated water content (WC, %) and water solubility (WS, %) of the gelatin films. The trend observed is that both investigated parameters decrease after the addition of CaCO₃ NPs in amounts from 0.5 to 5.0%, the decrease in WC of the biofilms being weaker compared to the decrease in WS. The moisture content of the control G film is 0.376% and decreases to 0.353% and 0.353% for G-0.5 CaCO₃ and G-1.0 CaCO₃ samples, respectively. When using larger amounts of nano calcium carbonate, WC varies between 0.308 – 0.212%. The higher WC values for the control plasticized with glycerol G film are due to its sensitivity to water, due to its hygroscopic and hydrophilic nature [20]. The latter is the reason for the limited application of gelatin-based films in contact with food products with high moisture content [17, 21]. On the other hand, the CaCO₃ nanofiller is able to bind to the free hydroxyl groups by forming bonds with gelatin chains, which reduces their number and therefore lowers the WC and the sensitivity of NPs-based biofilms to water [22].

The water absorption curves of the control film and gelatin biofilms with nano calcium carbonate over time are illustrated in Fig. 2.

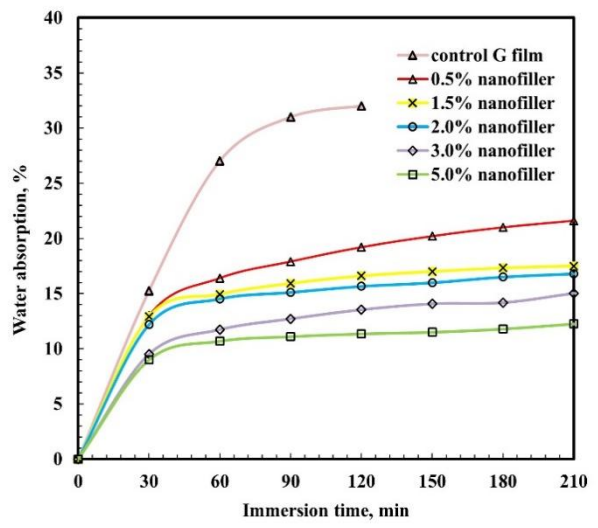


Fig. 2. Water absorption curves of gelatin-based biofilms on calcium carbonate nanofiller content

The highest water absorption (WA, %) of 32% is displayed by the control G film at a water immersion time of 120 min. With longer immersion, the plasticized gelatin film begins to dissolve in water [23] and it becomes impossible to determine its WA. The inclusion of nanoparticles in amounts up to 5.0% in the composition of the biofilms reduces the water absorption of the samples compared to that of the pure gelatin film. For example, for the control film after 90 min, WA is 31%. With the addition of filler, the water absorption of materials with 0.5, 1.0, 2.0, 3.0 and 5.0% CaCO₃ NPs decreases to 17.9, 15.9, 15.1, 12.7 and 11.1%, respectively. The tendency to decrease WA with increasing NPs concentration is maintained even at longer immersion times, probably due to the excellent barrier properties of these nanoparticles [24]. This means that the nano CaCO3 synthesized from Rapana Venosa shells successfully improves the water resistance and stability of gelatin-based biofilms in a high-humidity environment.

It was found that the addition of nanofiller also reduces the water solubility (WS, %) of the obtained plasticized films. Increasing the amount of CaCO₃ NPs from 0.5 to 3.0% gradually reduces WS and it is in the range from 4.672 to 3.662% (Table 1). The main reason for this is that CaCO₃ NPs make the structure of the G film more compact and thus limit the access of water molecules to the matrix [22, 25] and prevent its interaction with them [26]. That is why the smallest WS value of 2.402% is displayed by the G-5.0 CaCO₃ samples, which is almost 2.5 times lower compared to the control biofilm without nanofiller.

Tensile properties of gelatin-CaCO₃ NPs biofilms

To preserve the properties of biofilms during their use and eventual application, they should have appropriate strength and elasticity. Therefore, the tensile properties of the obtained biofilms were determined, namely, the tensile strength (Fig. 3), the elongation at break (Fig. 4), and the modulus of elasticity (Fig. 5).

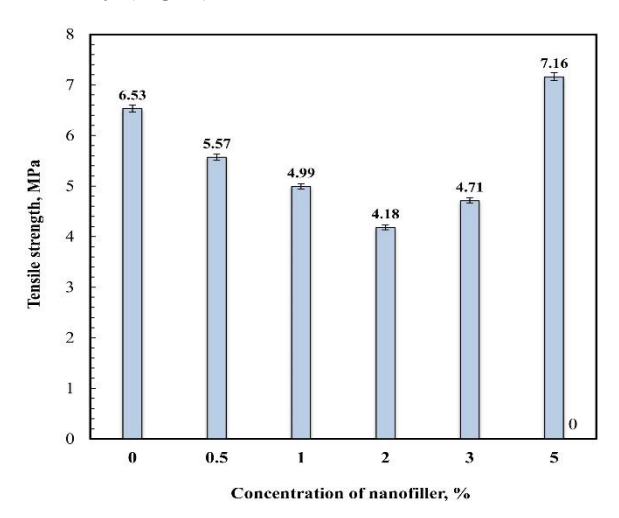


Fig. 3. Dependence of the tensile strength of gelatin-based biofilms on calcium carbonate nanofiller content

Fig. 3 shows the dependence of the tensile strength of gelatin films on the concentration of CaCO₃ NPs added. With an increase in the introduced calcium carbonate NPs to 2.0%, a decrease in the strength of the biofilms is observed. The reduced tensile strength of the films compared to the control G film can be due to the influence of NPs on the interactions in the gelatin matrix and the weakening of intermolecular bonds. Above the indicated amount, the strength slightly increases to 4.71 MPa but is still less than that of the initial biofilm without the additive. A similar decrease in strength for gelatin-based films when concentration of incorporated ZnO NPs was increased has also been found by Sahraee et al. [27]. The reinforcing effect of nanofiller on the gelatin samples is realized in the G-5.0 CaCO₃ film. A maximum tensile strength of 7.16 MPa was determined for it. The probable reason for this is that filling with 5.0% of nanoparticles reduces the mobility of G chains and enhances the interaction between them, resulting in an increase in the tensile strength of biofilms at this concentration of NPs.

The opposite tendency was seen in elongation at break of the obtained biofilms. With increasing NPs concentration from 0.5 to 1.0%, the elongation at break of the films (Fig. 4) increased from 124.6 for control G film to 205.1% for G-1.0 CaCO₃. When using larger amounts of the filler, the studied indicator decreased to 141.6% for G-5.0 CaCO₃ samples. However, all films, regardless of the amount of added biogenic nano calcium carbonate, showed higher values of elongation compared to the initial gelatin film without an additive.

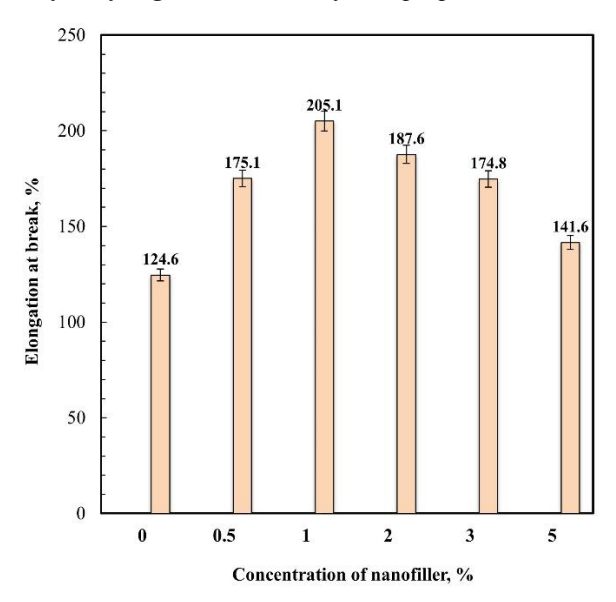


Fig. 4. Dependence of the elongation at break of gelatin-based biofilms on calcium carbonate nanofiller content

An increase in elongation at break over that of control G film by the addition of NPs was also found by other authors [28].

Similar to the tensile strength, the dependence of Young's modulus of biofilms on the addition of NPs of calcium carbonate follows the same course (see Fig. 5).

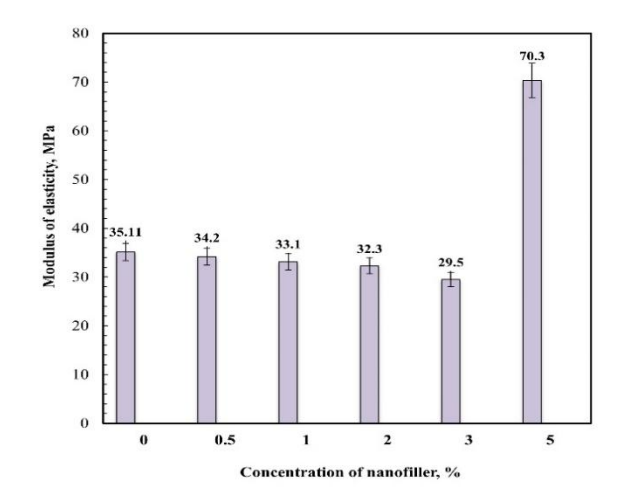


Fig. 5. Dependence of Young's modulus of gelatin-based biofilms on calcium carbonate nanofiller content.

When the amount of nanofiller is lower (up to 3.0%), the modulus smoothly decreases from 35.11 to 29.5 MPa for control G film and G-3.0 CaCO₃, respectively. With a further increase in the amount of the additive in the samples to 5.0%, its influence becomes apparent, and the Young's modulus has a maximum value of 70.3 MPa. The high modulus found for cast G-5.0 CaCO₃ films is associated with the higher tensile strength (Fig. 3) and hardness (Table 1).

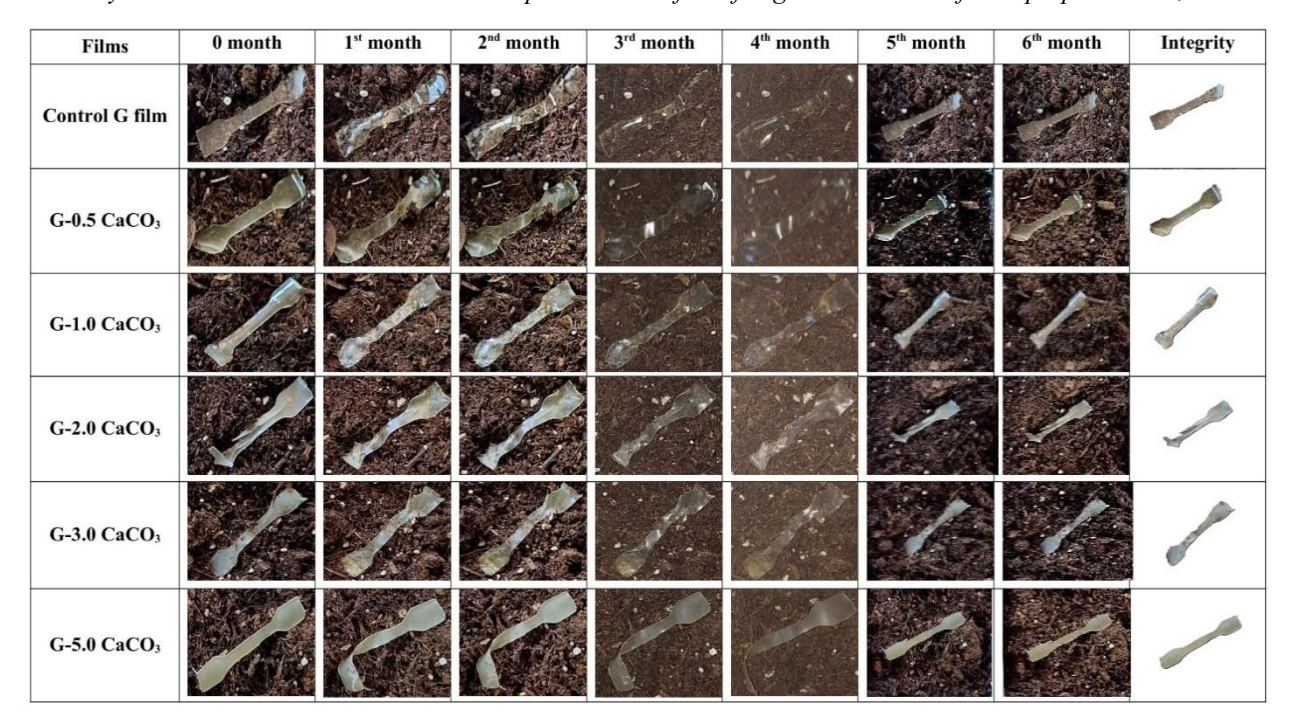


Fig. 6. Changes in the appearance of gelatin films before and after 6 months of exposure to compost soil surface

For all gelatin-based samples, both those without and those with NPs the measured hardness (from 74 to 82) is in full accordance with the results observed for the tensile strength and modulus of biofilms. This, according to the Shore A hardness scale, places the biofilms casted as medium hard.

Biodegradability of gelatin-CaCO₃ NPs biofilms

The visual change that gelatin films undergo is one of the first signs of the degradation process [29]. Already in the first month, the samples changed their original shape, and after the third month, the changes in the color and appearance of the biofilms with CaCO₃ NPs are obvious (see Fig. 6). With increasing the amount of NPs from the fourth month onwards, the opacity of the biofilms increases, especially for those with over 1.0% nanofiller. At the 6th month of the experiment, the films still show no signs of disintegration, but only changes at the edges of the samples and traces of degradation. The G-5.0 CaCO₃ film retained its shape and dimensions to a greater extent, despite the change in color and transparency after a period of 6 months on the surface of compost soil. This is probably due to structural changes occurring in the samples, which is the reason for the decrease in biodegradability, estimated by weight loss (Table 1). When comparing the biodegradability of the control G film to the biodegradability of those with the additive, it is seen that the addition of CaCO₃ NPs in the films in amounts from 0.5 to 5.0% slows down the degradation process (Table 1). The determined weight loss of the control G film is

8.537% after exposure to the surface of compost soil for 6 months. The weight loss of the biofilms with a nanofiller content of up to 2.0% is close to that of the gelatin film without the additive - from 8.402 to 8.142%. When increasing the amount of CaCO₃ NPs to 3.0%, a slowdown in the degradation process is observed. The G-5.0 CaCO₃ film undergoes the least degradation (4.990%) after 6 months of exposure to the surface of compost soil. It is assumed that the inclusion of nanoparticles in the matrix stabilizes the structure and reduces the degree of biodegradation due to an increase in the crystallinity of the biofilms [17]. Furthermore, the reduced water absorption of the nano calcium carbonate materials (Fig. 2) also hinders degradation, as the presence of water in the gelatin films is crucial to accelerate the process. The above is an evidence that the used additive of CaCO₃ NPs in the gelatin films makes them more resistant and less susceptible to degradation after exposure to the surface of a compost soil for a period of 6 months and therefore can increase the service life of biofilms.

CONCLUSIONS

Films combining gelatin, calcium carbonate nanofiller in amounts from 0.5 to 5.0% and glycerol as a plasticizer were obtained by the solution casting method, and their main properties were determined. The results for the properties of the plasticized gelatin biofilms filled with nanoparticles were monitored in terms of the influence of the additive on them and compared with those of a control film of pure gelatin. It was found that the nano calcium

carbonate used reduces the water solubility and water absorption of the films, increases the thickness and the elongation at break, and the films with 5.0% of the filler have the best tensile strength and modulus of elasticity. It has been proven that calcium carbonate nanofiller successfully slows down the biodegradation process of gelatin-based biofilms, and after exposure to the surface of compost soil for 6 months, they retain their integrity.

Acknowledgement: This work was supported by the Scientific Research Center at Prof. Assen Zlatarov University under the contract № 495/2024.

REFERENCES

- 1. S. Hajji, H. Kchaou, I. Bkhairia, R. Ben Slama-Ben Salem, S. Boufi, F. Debeaufort, M. Nasri, *Food Hydrocoll.*, **116**, 106639 (2021).
- S. Al-Nimry, A. A. Dayah, I. Hasan, R. Daghmash, Mar. Drugs, 19, 145 (2021).
- 3. I. Zulkiflee, M. B. Fauzi, *Biomedicines*, **9**, 979 (2021).
- 4. A.A. Tyuftin, J.P. Kerry, *Food Packag. Shelf Life*, **29**, 100688 (2021).
- 5. Z. Yang, S. Chaieb, Y. Hemar, *Polym. Rev.*, **61**, 765 (2021).
- P.O. Onyeaka, H. Dai, X. Feng, H. Wang, Y. Fu, Y. Yu, H. Zhu, H. Chen, L. Ma, Y. Zhang, Food Hydrocoll., 144, 108972 (2023).
- 7. I. Surya, C. M. Hazwan, H. P. S. Abdul Khalil, E. B. Yahya, A. B. Suriani, M. Danish, A. Mohamed, *Polymers*, **14**, 4147 (2022).
- 8. P. Trigueiro, J. P. D. L. Pereira, M. G. Ferreira, L. B. Silva, L. Neves, R. R. Peña-Garcia, *Minerals*, **14**, 613 (2024).
- D. Lin, Y. Yang, J. Wang, W. Yan, Z. Wu, H. Chen,
 Q. Zhang, D. Wu, W. Qin, Z. Tu, *Int. J. Biol. Macromol.*, 154, 123 (2020).
- 10. M. Abbas, M. Buntinx, W. Deferme, R. Peeters, *Nanomaterials*, **9**, 1494. (2019).
- 11. W. Zhang, J. W. Rhim, Food Packag. Shelf Life, **31**, 100806 (2022).

- 12. N.S. Ahmed, F.H. Kamil, A.A. Hasso, A.N. Abduljawaad, T.F. Saleh, S.K. Mahmood, *J. Mech. Behav. Mater.*, **31**, 1 (2022).
- 13. A.I. Hussein, Z. Ab-Ghani, A. N. Che Mat, N. A. Ab Ghani, A. Husein, I. Rahman, *Appl. Sci.*, **10**, 7170 (2020).
- 14. S. El-Sherbiny, S. El-Sheikh, A. Barhoum, *Powder Technol.*, **279**, 290 (2015).
- P. Fadia, S. Tyagi, S. Bhagat, A. Nair, P. Panchal, H. Dave, S. Dang, S. Singh, *Biotech.*, 11, 457 (2021).
- S. Kundu, A. Das, A. Basu, M. F. Abdullah, A. Mukherjee, *Carbohydr. Polym.*, 170, 89 (2017).
- M.R. Khan, M.B. Sadiq, *Polymer Bulletin*, 78, 4047 (2021).
- 18. S. Roy, J-W. Rhim, Appl. Sci., 11, 6307 (2021).
- 19. K. Rubini, A. Menichetti, M. C. Cassani, M. Montalti, A. Bigi, E. Boanini, *Gels*, **21**, 354 (2024).
- 20. P.V. Pulla-Huillca, A. Gomes, A.M.Q.B. Bittante, R.V. Lourenco, P.J. do Amaral Sobral, *J. Food Eng.*, **297**, 110480 (2021).
- P. Bergo, I.C.F. Moraes, P.J.D.A. Sobral, Food Hydrocoll., 32, 412 (2013).
- 22. R. Huang, A. Yao, Y. Yan, J. Wang, Q. Li, K. Li, Y. Tian, S. Wang, J. Wu, *eFood*, **5**, e179 (2024).
- M.I.J. Ibrahim, S.M. Sapuan, E.S. Zainudin, M.Y.M. Zuhri, A. Edhirej, in: Advanced Processing, Properties, and Applications of Starch and Other Bio-Based Polymers, Faris M. Al-Oqla, S.M. Sapuan (eds.), Elsevier, 2020, p. 35.
- 24. H. He, J. Yang, W. Huang, M. Cheng, *Adv. Polym. Tech.*, **37**, 1022 (2016).
- 25. J. Chen, L. Luo, C. Cen, Y. Liu, H. Li, Y. Wang, *Int. J. Biol. Macromol.*, **220**, 462 (2022).
- 26. Y. Wang, A. Liu, R. Ye, X. Li, Y. Han, C. Liu, *Int. J. Food Prop.*, **18**, 2442 (2015).
- 27. S. Sahraee, B. Ghanbarzadeh, J.M. Milani, H. Hamishehkar, *Food Bioprocess Technol.*, **10**, 1441 (2017).
- 28. P. Soo, N.M. Sarbon, *Food Packag. Shelf Life*, **15**, 1 (2018).
- S.H. Othman, N.D.A. Ronzi, R.A. Shapi'i, M. Dun, S.H. Ariffin, M.A.P. Mohammed, *Coatings*, 13, 777 (2023).

Application of Me-PAN nanocomposite membrane in two-stage ultrafiltration of industrial wastewater

M. P. Miteva^{1*}, V.O. Raikova²

Received: May 11, 2025; Revised: June 07, 2025

Membrane technologies and processes present a viable technological solution to address modern industrial and ecological challenges related to water resources. In this, the potential application of polyacrylonitrile (PAN) membranes and PAN membranes modified with a surface-deposited Fe-Cr-Ni nano layer (Me) was explored in the ultrafiltration process. These membranes were tested individually and in combination for the purification of industrial wastewater resulting from the hydrodistillation of oil-bearing roses, which contained 15.80 mgEmKMnO₄/ml of total organics. The transport and separation characteristics of the membranes were analyzed based on pressure changes and their structural morphology response. The permeability values ranged from 19 l/m².h for the unmodified membrane to only 3.7 l/m².h for the metallized membrane. The process was optimized using a combined approach, where ultrafiltration was conducted sequentially and continuously in two stages: 1. Ultrafiltration through a PAN membrane to obtain permeate (P1); 2. Ultrafiltration of P1 using the Me-PAN membrane to obtain permeate (P2). It was found that in the two-stage ultrafiltration process, the permeability remained the same for the first stage, but increased to 13 l/m².h at 0.5 MPa for the second stage. The total organics content in P2 was reduced to 1.74 mgEmKMnO₄/ml, resulting in a 89% rejection and purification of the wastewater. This not only rehabilitated the treated wastewater but also provided an opportunity for the targeted utilization of the separated unique and valuable bio-resources present in the wastewater from the oil-bearing roses processing.

Keywords: Ultrafiltration, metal nano layer coating, nanometalized polymer membrane, nanocomposite membrane, industrial wastewater treatment, recovery of bio-resources

INTRODUCTION

Membrane separation technology and its capabilities have been implemented in industry on the largest scale through the baromembrane processes of microfiltration (MF), ultrafiltration (UF), nanofiltration (NF) and reverse osmosis (RO). This is due to their simplicity and accessibility, capital profitability, ease of maintenance and control, technological and ecological efficiency, and the possibility to use them in hybrid processes. Pressure-driven membrane processes implemented for separation, purification, concentration, and disinfection of liquid systems of various natures and origins, and also provide an opportunity for the rehabilitation of substances and resources. The areas of application of these processes are related to potable and wastewater treatment in pharmaceutical, biotechnological, foodprocessing industries, as well as in processes of renewable energy storage and conversion [1]. What is common to the baromembrane processes in addition to the driving force is the semipermeable

membrane, which, apart from being a key element, is also a specific selective barrier. Conventional membranes used in these processes are synthetic, preferably made of polymer materials. Each of the processes has its specific requirements towards the membrane properties, which are permeability and rejection [2]. As technological challenges to ensure quality water resources increase, so does the demand for and exploitation of UF processes and membranes [3]. PAN membranes have proven their effectiveness in ultrafiltration process. Moreover, they are also an object that allows for manipulation of their properties by means of various modification techniques. Using such an opportunity, selective structural control of the membranes is purposefully achieved, with a significant effect on their performance [4-6]. An innovative approach to PANmembranes modification is the fixation of a metal coating on the active membrane surface. Various methods of metal coating deposition can be used, the choice depending on the properties of the host polymer matrix, the type of metal, the preliminary modification of the polymer surface, the mechanism

¹ Department of Technology, Materials and Materials Science, Faculty of Technical Sciences, Burgas State University "Prof. Dr. Assen Zlatarov", Burgas, Bulgaria

² Food Technologies in Household and Tourism Sections, Technical University of Sofia - Faculty and College of Sliven, Sliven, Bulgaria

^{*} To whom all correspondence should be sent: E-mail: *rmkpetrovi@abv.bg*

and conditions of applying the coating [7, 8]. Surface morphology of the PAN membrane can be easily controlled by the use of vacuum metallization [9]. The process consists of magnetron sputtering of a metal (or metals) in a vacuum environment with subsequent mechanical deposition on the chemically activated polymer surface of the membrane. Metallized membranes are a promising option for achieving sustainability in water systems treatment [10, 11]. Applied alone or in combination with other types of membranes, they can increase the efficiency of membrane technologies [12]. The aim of the present work is to conduct a laboratory study of the application of polyacrylonitrile and metallized polyacrylonitrile membranes in an ultrafiltration process for treating industrial wastewater-obtained as a result of oil-bearing rose hydrodistillation.

Studying the process of ultrafiltration, which uses membranes with different properties, will clarify their application potential for the purification of biocontaminated industrial wastewater and recovery of bio-resources, as well as the peculiarities in the particular membrane behavior and the adaptation of the process conditions to the object under treatment [13, 14]. The development and introduction of sustainable technologies will allow the industry to become more environmentally friendly by facilitating waste materials recycling and utilization of resources [3, 15].

EXPERIMENTAL

The PAN membrane used in the experiment had a molecular weight cut-off (MWCO) of 25 kDa and was formed from a polyacrylonitrile solution in dimethyl sulfoxide (DMSO) solvent, a product of Fluka, Germany. After filtration and deaeration, a film was drawn from the polymer solution onto a calendered polyester substrate attached to a glass plate. The polyester mat brand FO-2403, produced by Velidon Filtren, Germany, has a density of $100 \pm$ 5 g/m² and a thickness of 2 ± 0.1 nm. Within 15 sec of pouring the solution, the plate was immersed in a lab bath of distilled water at a temperature of 25 \pm 1°C. Through the method of phase inversion in a water coagulation bath non-solvent induced phase separation (NIPS), an asymmetric membrane structure was formed, which was then thoroughly washed with water until the solvent was completely removed.

Pieces of the membrane with an area of 100 cm² were prepared for modification by depositing a metallizing layer after preliminary activation of the membrane surface with alkaline solutions of SnCl₂.2H₂O. The metal coatings were obtained in a

vacuum installation BUP-5 (Russia), by sputtering a flat target made of iron-chromium-nickel alloy with dimensions ø 100×10 mm, at a target (M)/substrate (N) distance L $_{\text{M-N}} = 180$ mm and specific sputtering power Np = 5.4 W/cm². Magnetron deposition of the iron-chromium-nickel alloy was carried out with an initial vacuum in the working chamber Pn= 1.10^{-3} Pa, Ar working gas medium of 99.99~% purity, working pressure in the chamber Pp = 4.10^{-2} Pa and coating deposition time (exposure time) of 25~s. After the deposition process was completed, the membranes were cooled to normal temperature.

The efficiency of the membranes and membrane processes was studied based on the parameters of rejection and permeability. Rejection is expressed as a retention parameter and characterizes the separation ability. Permeability is characterized by a parameter called flux through the membrane. The values were calculated by the following equations:

$$R = \frac{c_2 - c_1}{c_2} \cdot 100, \% \tag{1}$$

where C_2 – concentration of the retained substance in the flow over the membrane, kg/m³; C_1 concentration of the same substance in the flow through the membrane kg/m³;

$$J = V/(S.\tau), l/m^2. h$$
 (2)

where V – volume of the liquid which passed through the membrane, l; S – membrane effective area, m^2 ; τ – time, h.

The membrane-treated object was industrial wastewater, a by-product of hydrodistillation of oilbearing rose flowers in Bulgarian rose oil production, provided by the Institute of Roses, Essential and Medical Cultures (EMLK), Kazanlak. The quantitative content of total organic matter in the hydrodistilled wastewater and in the permeate (filtrate) was determined by the method of permanganate oxidizability and presented as a potassium permanganate equivalent (mgEm KMnO₄) [16].

RESULTS AND DISCUSSION

UF PAN membranes are formed and used as polymer composites. The membrane structure is supported by a polymer substrate made of various types of polymers. A composite asymmetric structure is created (Fig. 1), in which the supporting porous polymer aids in to the mechanical stability when external pressure is applied to achieve an ultrafiltration process.

The membrane is then further modified as a metal-polymer nanocomposite, also incorporating a functional metal layer of chromium-nickel alloy [17]. Consequently, the modified membrane gains new properties.

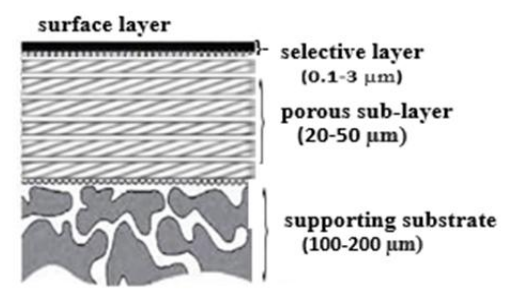


Fig. 1. Schematic diagram of an asymmetric composite membrane in-depth

The membrane metalized in the experiment for 25 min, and the non-modified one were individually used in a membrane process, carried out in a laboratory research barofiltration installation. The filtration focused on bio-contaminated wastewater from the rose flowers of the *Rosa damascena* Mill. f. trigintipetala Dieck (R.D.) variety, with a total organic content of 15.80 mgEm KMnO₄/ml. The permeability results, as shown in Figure 2, pertain to the wastewater and illustrate the minimal effectiveness of the modified membrane in this particular approach.

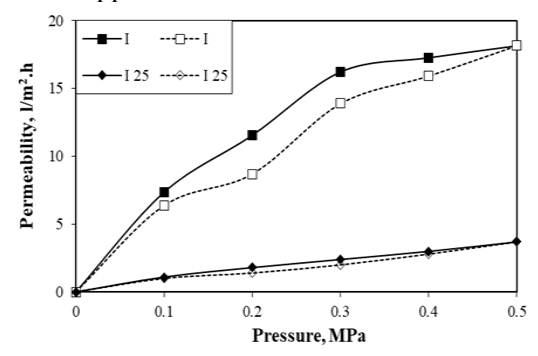


Fig. 2. Hysteresis curves of permeability for a PAN membrane and a metallized membrane for 25 min

The permeability of the two types of membranes differs not only in the range, with the non-modified membrane reaching up to 19 l/m².h and the metallized one only reaching 3.7 l/m².h, but also in the response of the structural morphology to pressure changes. This difference is due to the unique characteristics of the selective layer of the metallized membrane, which consists of many small and similarly sized pore openings. This is supported by AFM visualization [17] and the minimal change in permeability values with increasing force impact from applied pressure (Fig. 2). The expectation that smaller sized pores would be included in the process with each 0.1 MPa step is not confirmed. Despite the extended metallization time, the mechanical stability of the membrane was maintained in the processing of a real object. We can assess this by visually

comparing the shape and size of the hysteresis areas (Fig. 2), which provide an indication of the material's mechanical behavior under cyclic loading [18]. An explanation for the unsatisfactory results is that ultrafiltration, during the solvent preferentially through the membrane, causing an increase in viscosity of the retentate and preconcentration of dissolved substances in the boundary layer of the membrane. Consequently, the driving force and process speed decrease, which is a prerequisite to the formation of aggregates in the retentate and eventually their precipitation on the membrane surface, reducing its effective area [19]. For the process to function properly, it is necessary to optimize the correlation between membrane properties and fluid concentration.

Based on the results obtained, a combined treatment approach was implemented for wastewater to enhance the efficiency of the ultrafiltration process and explore the potential of the metal-polymer membrane. The process involved two stages. The first stage included ultrafiltration of the wastewater through the PAN-membrane. The second stage involved subjecting the permeate from the first stage (P1) to ultrafiltration through the metal-polymer membrane to obtain the final permeate (P2) for the two-stage process. It was observed that the permeability of the metallized membrane to P1 differed when compared to direct filtration of wastewater through the same membrane (Fig. 2).

The graphical representation in Figure 3 illustrates the permeability change in the two-stage process. Permeability values are expected to increase with increasing pressure. During the first stage, when the PAN-membrane is used, the permeability values remain the same. However, when the metallized membrane is used, the permeability values increase from 3.7 l/m².h for normal ultrafiltration to 13 l/m².h for the two-stage ultrafiltration at 0.5 MPa.

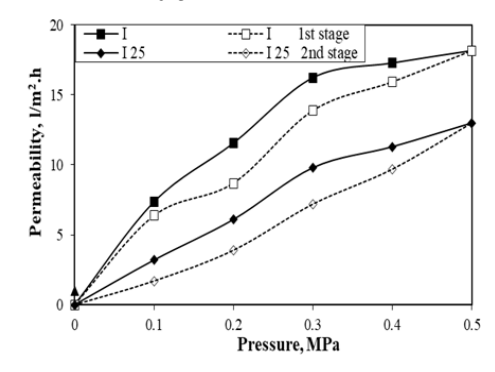


Fig. 3. Hysteresis curves of the PAN membrane permeability relative to wastewater for the 1st stage and of the Me-PAN membrane relative to permeate P1 for the 2nd stage of a two-stage ultrafiltration process.

In the first stage, the PAN-membrane shows the same rejection rate as in individual ultrafiltration (Table 1) and releases wastewater with a decrease to 8.85 mgEm KMnO₄/ml of total organics.

The lower concentration of organic matter in P1 compared to the initial concentration is the reason for the facilitation of the flow passage. This assumption is based on the specific processes occurring on the surface of a metal-polymer membrane during its individual use.

Table 1. Rejection of the two-stage ultrafiltration process relative to the total organics (mgEm KMnO₄/ml) when treating wastewater from *Rosa Damascena* hydrodistillation

Membrane	Stage R, %	Final R, %
Ι	56	89
I25	75	89

As a result, the permeability of the metal-polymer membrane to P1 significantly increases at all pressure levels (as shown in Fig. 3) with a rejection rate of 75%. The total organics content in the final filtrate P2 after the two-stage ultrafiltration treatment is only 1.74 mgEm KMnO₄/ml, and the total rejection achieved is 89%.

CONCLUSIONS

The potential of applying both a PAN membrane and a surface-modified Me-PAN membrane in an ultrafiltration process for the purification of industrial wastewater from oil-bearing rose hydrodistillation was investigated.

The performance characteristics of the membranes were determined, showing that when used sequentially in a two-stage ultrafiltration process and depending on the operating conditions, the permeability of the Me-PAN membrane increased from 3.7 l/m².h to 13 l/m².h.

It was demonstrated that more effective purification of industrial wastewater is achieved in the two-stage ultrafiltration process with the retention of bioorganic substances up to 89%. The total organic substance content in the purified water decreases from 15.80 mgEm KMnO₄/ml to 1.74 mgEm KMnO₄/ml, providing an opportunity for their valorization through the resulting retentate.

Acknowledgement: This study was financially supported by the Burgas State University through the Scientific Research Sector—Project No 478/2024. The promotion of this research is supported by the

Institute of Chemical Engineering (ICHE) of the Bulgarian Academy of Sciences (BAS), Sofia and Organizing committee with the financial support of the National Science Fund by contract № KP-06-H57/3/15.11.2021 under the project "Optimal safety loads and geometry for layered nanocomposites under thermo-mechanical loading". The authors would like to thank Prof. Stoiko Petrov for his scientific advices and assistance.

REFERENCES

- 1. X. Tan, D. Rodrigue, *Polymers*, **11**(7), 1160 (2019).
- R. W. Baker, Membrane Technology and Applications (2nd edn.), Chichester, John Wiley & Sons Ltd., 2004.
- 3. S. Al Aani, T. N. Mustafa, N. Hilal, *J. Water Process Eng.*, **35**, 101241 (2020).
- 4. D. Christova, M. Staneva, S. Ivanova, M. Alexandrova, Ph. Ublekov, M. Dencheva-Zarkova, J. Genova, I. Tsibranska, B. Tylkowski, *J. Phys.: Conf. Ser.* 2436 012024 (2023).
- S. Arefi-Oskoui, A. Khataee, S. Jabbarvand Behrouz, V. Vatanpour, S. H. Gharamaleki, Y. Orooji, M. Safarpour, Sep. Purif. Technol., 280, 119822 (2022).
- 6. T. Petrova, E. Kirilova, R. Vladova, A. Apostolov, B. Boyadjiev, A. Moravski, *Bulg. Chem. Commun.*, **56** (3), 333 (2024).
- 7. M. J. Detisch, T. J. Balk, M. Bezold, D. Bhattacharyya, *J. Mater. Res.*, **35**(19), 2629 (2020).
- 8. R. Melentiev, A. Yudhanto, R. Tao, T. Vuchkov, G. Lubineau, *Mater. Des.*, **221** 110958 (2022).
- 9. A. H. Mostafavi, A. K. Mishra, F. Gallucci, J. H. Kim, M. Ulbricht, A. M. Coclite, S. S. Hosseini, *J. Appl. Polym. Sci*, **140**(15), e53720 (2023).
- N. Li, Y. Fu, Q. Lu, C. Xiao, *Polymers*, 9(10), 524 (2017).
- 11. A. Sahu, R. Dosi, C. Kwiatkowski, S. Schmal, J.C. Poler, *Polymers*, **15**, 540 (2023).
- 12. H. Abdallah, D.N. Abd-Elshafy, M. Shalaby et al., *Appl. Water Sci.*, *14*, 245 (2024).
- 13. J. Luo, L. Ding, B. Qi, M. Y.Jaffrin, Y. Wan, *Bioresour. Technol.*, **102**(16), 7437 (2011).
- Z. Rizki, M. Ottens, Sep. Purif. Technol., 315, 123682 (2023).
- B. Muñoz-Palazon, S. Gorrasi, A. Rosa-Masegosa, M. Pasqualetti, M. Braconcini, M.Fenice, *Molecules*, 28(1), 314 (2023).
- 16. BDS 17.1.4.16:1979. https://bds-bg.org/en/project/show/bds:proj:21368
- 17. V. Slavova, M. Miteva, S. Petrov, *IJRAT*, **4**(11), 24 (2016).
- 18. K. V. Kurada, M. Mukherjee, S. De, Sep. Purif. Technol., **227**, 115736 (2019).
- 19. N. AlSawaftah, W. Abuwatfa, N. Darwish, G. Husseini, *Water*, **13**(9), 1327 (2021).

Nanofiller concentration in PMMA-nanocomposites for preliminary dental restorations

M. Dimova-Gabrovska^{1*}, R. Moskova², A. Vlahova³, S. Rangelov¹

¹Department of Prosthetic Dental Medicine, Faculty of Dental Medicine, Medical University – Sofia, 1, Sv. Georgi Sofiyski Str., Sofia 1431, Bulgaria

²Faculty of Dental Medicine, Medical University – Sofia, 1 Sv. Georgi Sofiyski Str., Sofia 1431, Bulgaria ³Department of Prosthetic Dental Medicine, Faculty of Dental Medicine, Medical University -Plovdiv, 3, Hr. Botev Blvd., Plovdiv 4000, Bulgaria

Received: May 30, 2025; Revised: June 17, 2025

Digital dentistry has significantly transformed patient perceptions regarding various dental procedures by emphasizing high precision, enhanced comfort, personalized treatment plans, and reduced treatment times. This systematic review aims to identify and categorize the most commonly used nanocomposites in the 3D printing of provisional restorations, based on representative results from tests such as flexural strength and elastic modulus measurements. An English-language literature search was conducted using keywords including nanocomposites, provisionals, safe load, 3D printing, and geometry across multiple databases: PubMed, Google Scholar, ScienceDirect, and Scopus. The selection and categorization of relevant studies were carried out in accordance with the Preferred Reporting Items for Systematic Reviews and Meta-Analyses (PRISMA) 2020 guidelines. A total of 231 articles were initially identified based on their titles. Selected articles were then analyzed according to the following criteria: historical developments in dental materials; applications of nanotechnology in dentistry; and the use of polymethyl methacrylate (PMMA) in the fabrication of provisional and preliminary fixed restorations. In conclusion, while the full potential of nanomaterials in dentistry is still being uncovered, ongoing advancements are expected to further enhance their properties and applications.

Keywords: nanocomposites, provisional restorations, PMMA, 3D printing, digital dentistry

INTRODUCTION

One of the major branches of contemporary dentistry is digital dentistry which involves the integration of digital technologies into routine clinical practice. This includes tools such as intraoral scanners, Computer-Aided Design (CAD) and Computer-Aided Manufacturing (CAM) systems, three-dimensional (3D) printing, and digital radiographic imaging [1]. Digital dentistry has significantly shifted patient perceptions of dental procedures by emphasizing high precision, increased comfort, case-specific customization, and expedited treatment timelines [1].

technology CAD/CAM involves preformed blocks of material into desired forms such as veneers, crowns, bridges, and other restorations. This approach enables high precision in the planning and fabrication of provisional restorations, largely due to the seamless connection between the digital impression and the restoration design. Consequently, this minimizes processing and fabrication time [2]. 3D printing represents another vital component of digital dentistry. This technique employs additive manufacturing to construct objects layer by layer, offering high precision, reduced material waste, and rapid production times [2, 3].

Despite these advantages, digital dentistry also presents challenges. These include high initial costs, the need for frequent technological updates, and the requirement for specialized training of personnel [4]. Furthermore, the materials used in digital workflows often differ from those in conventional methods, necessitating specific handling protocols and testing procedures [4].

Digital dentistry is closely associated with the fabrication of provisional restorations, which require exceptional precision, particularly in marginal fit. Technologies such as CAD/CAM and 3D printing are well-suited to meet these requirements, though the cost of production and implementation remains a limitation. Within the Bulgarian scientific community, various authors have investigated the integration of digital technologies and materials in the fabrication of provisional restorations. Notably, Dimova *et al.* (1998) explored patient perspectives on preliminary restorations [5]. Additional studies have highlighted pediatric cases where treatment

Both CAD/CAM and 3D printing provide several advantages, including shorter times for diagnosis, planning, and restoration fabrication; seamless integration of various tools (e.g., scanners, printers, milling units); and enhanced patient comfort and involvement [4].

^{*} To whom all correspondence should be sent: E-mail: *marianadimova@abv.bg*

with crowns presents unique challenges due to agerelated factors. In such situations, digital dentistry can facilitate more efficient treatment planning and execution, ultimately improving outcomes and reducing patient stress [6, 7].

Dental materials used in digital workflows differ significantly from their analog counterparts, requiring specialized testing and performance characteristics for each application. Composites are among the most commonly used materials for provisional restorations. These materials vary in their polymerization behavior and in the exothermic reactions they produce during curing [8]. Digital dentistry enables the effective incorporation of CAD/CAM technologies in the fabrication process, offering consistent quality and reproducibility [9].

An important contemporary development in dental materials is nanodentistry. Nanotechnology—or molecular engineering—focuses on the design and production of materials and structures with particle dimensions ranging from 0.1 to 100 nanometers. Nanocomposites are created by embedding nanoscale inorganic filler particles into an organic or hybrid matrix, often using a coupling agent to enhance adhesion between the matrix and the filler phase [10, 11].

Nanocomposites have a wide range of applications in dentistry, including caries-preventive restorative materials, reinforced resin bases for dentures, and provisional restorations [10, 12]. In Bulgaria, several authors have explored the properties of these materials. Ivanova *et al.* examined the delamination tendencies at the interface of bi-layered materials, identifying potential weaknesses in such structures [13]. Other research teams have analyzed the structural characteristics and mechanical parameters of nanocomposites, contributing to a deeper understanding of their performance [14–20].

Polymethyl methacrylate (PMMA) is one of the most widely used matrix materials in nanocomposites. PMMA is a hard, thermoplastic polymer known for its high Young's modulus and excellent scratch resistance [21]. Its flexural strength exceeds that of polyethyl methacrylate, making it a preferred choice for provisional and long-term restorations [22].

AIM

The aim of this systematic review is to identify and categorize the most commonly used nanocomposites in the 3D printing of provisional dental restorations, based on representative data from mechanical tests such as flexural strength and elastic modulus measurements.

MATERIALS AND METHODS

A survey was conducted in English based on keywords such as nanocomposites, provisionals, safe load, 3D print, and geometry, in different articles in the following databases: PubMed, Google Scholar, Science Direct, and Scopus. To select and categorize the collected information followed the Preferred Reporting Items for Systematic reviews and Meta-Analyses (PRISMA) 2020 guidelines.

Study selection

A survey was conducted in English based on keywords such as nanocomposites, provisionals, safe load, and geometry, in different articles in the following databases: PubMed, Google Scholar, Science Direct, and Scopus. Inclusion criteria consist of full-text articles, systematic reviews, and meta-analyses. Abstracts, patents, and short communications were excluded. Of 231 scientific research articles, 103 meet the inclusion criteria and are included in this article.

Analysis

A specific form in Microsoft Office Excel was used to systematize the extracted data and analysis. Duplicates were eliminated.

RESULTS

Initially, 231 articles were identified based on their titles in the database mentioned. The articles were published up to December 2024. Duplicate entries were removed. 192 articles remained. Therefore, an abstract review was made. Out of the 192 studies mentioned, 103 met the inclusion criteria. 89 were excluded from the survey due to insufficient data or different tests used. Figure 1 depicts the selection process using the PRISMA flow chart as a graphical representation of the evaluation process.

DISCUSSION

Historical review

The conceptual origins of nanotechnology can be traced back to 1960, when physicist Richard Feynman delivered his now-famous lecture, "There's Plenty of Room at the Bottom."

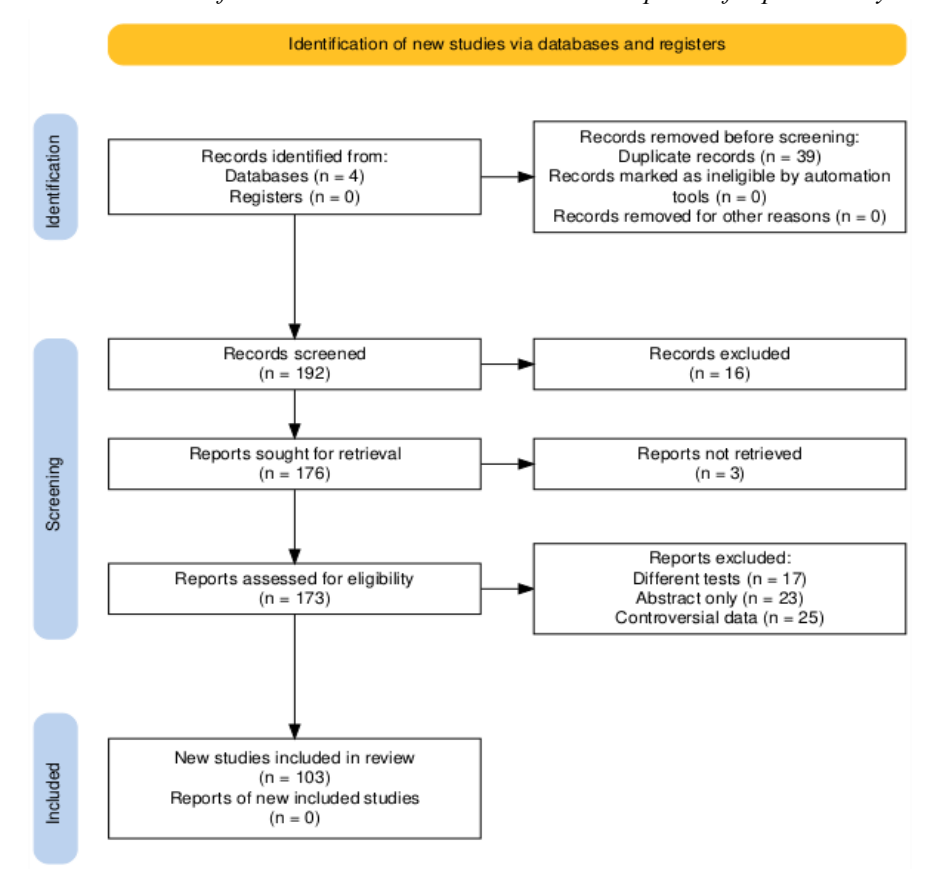


Figure 1. PRISMA flow chart.

In his visionary address, Feynman outlined a future in which scientists could manipulate individual atoms and molecules to create materials with unprecedented properties and performance [23]. Although the technical feasibility of such manipulation was purely theoretical at the time, Feynman is now recognized as one of the foundational thinkers behind the atomic theories that underpin modern nanomaterial science.

It would take several decades for these ideas to evolve into tangible scientific progress. By the early 2000s, the rapid advancement of molecular engineering and nanofabrication technologies had brought many of Feynman's predictions closer to reality. Notably, in the year 2000, Robert A. Freitas Jr. expanded upon Feynman's vision in an article published in the Journal of the American Dental Association, where he introduced the concept of nanodentistry [24]. Freitas proposed futuristic applications of nanotechnology in dental care, such as the use of dental nanorobots for targeted anesthesia, reduction of dentin hypersensitivity, and other microscale therapeutic interventions. At the time, these suggestions seemed far-fetched-much like Feynman's did in the 1960s—but they foreshadowed innovations that are now being actively explored or developed.

Today, nanotechnology is recognized as a cornerstone of innovation across multiple scientific disciplines, including medicine and dentistry. It plays a vital role in the design and fabrication of nanomaterials, which are now widely used in dental composites, coatings, drug delivery systems, and regeneration. Nanodentistry, once theoretical field, has grown into a distinct and impactful area of dental research and clinical application. The ongoing integration nanotechnology into digital workflows, such as 3D printing and CAD/CAM fabrication, solidifies its relevance in modern dental practice.

Nanotechnology in dentistry

In 2003, Ure *et al.* noted that while nanotechnology was largely regarded as a scientific discipline, its practical applications in dentistry—collectively termed nanodentistry—were still in their early stages of development [25]. Since then, the field has experienced significant growth, and various nanostructures are now being explored and implemented in dental applications. These include nanoparticles (ranging in size from 0.1 to 100 nanometers), as well as nanorods, nanospheres, nanotubes, nanofibers, dendrimers, and dendritic copolymers [12].

The fabrication of these nanostructures typically follows one of two primary methods: the bottom-up or top-down approach. The bottom-up approach involves constructing nanoparticles from atomic or molecular units through techniques such as desolvation, emulsification, spray drying, and freeze drying [26]. This method allows for precise control particle over size. distribution. surface characteristics, and overall purity. For example, Mitra et al. developed a synthetic chemical process in which molecules are assembled in a stepwise fashion to form nanoscale filler particles suitable for dental applications [27]. In contrast, the top-down approach starts with bulk materials that are subsequently broken down into nanosized particles using mechanical or physical methods, including etching, homogenization, milling, ultrasonication [28]. While this method is more straightforward and often less expensive, it generally results in lower control over particle size and uniformity, and can compromise the surface integrity and mechanical properties of the nanoparticles [12, 29, 30].

In the context of dentistry, the bottom-up approach is generally preferred for the synthesis of nanocomposites due to its superior control over morphology and enhanced mechanical and optical properties of the final product. These characteristics are critical in achieving high-performance materials for restorative and prosthetic dentistry.

Beyond restorative materials, nanotechnology is also being extensively researched for other dental applications. For instance, nanoengineered coatings for dental implants have shown promise in promoting osseointegration, while nanoscale bone graft materials are being investigated for their potential to accelerate bone regeneration [31–33].



Figure 2. Applications of nanotechnology in dentistry (Shalini *et al.*, 2020 [33]).

Furthermore, nanotechnology is playing a transformative role in drug delivery systems, periodontal therapy, caries prevention, and tissue

engineering. An overview of current and potential applications of nanoengineering in dentistry is provided in Figure 2 illustrating the breadth and future direction of the field.

Nanocomposites in dentistry

Nanocomposites are a primary nanotechnological application in dentistry, used for provisional restorations and definitive restorative materials [33, 34]. They comprise nanosized inorganic fillers dispersed in organic or inorganic matrices, connected *via* coupling agents that reduce nanocluster formation and enhance mechanical properties [10, 11, 35].

PMMA for provisional restorations

Provisional restorations are vital for maintaining vertical occlusion, preventing tooth migration, and ensuring temporomandibular joint and muscular during treatment [36]. Polymethyl stability methacrylate (PMMA) is commonly used due to affordability, aesthetic acceptability, ease of manipulation, and polishability. However, PMMA exhibits high polymerization shrinkage, causing marginal inaccuracies that risk periodontal disease and restoration failure [38-43]. PMMA is also durable and widely employed in denture bases [39, 43–45]. The requirements and desired characteristics of PMMA are summarized in Fig. 3. Balkenhol et al. compared self-curing PMMA (Trim) with dualcuring composites, showing superior flexural strength and modulus in composites over time [46]. Similarly, Barqawi et al. (2024) reported that lighturethane dimethacrylate (UDMA) outperforms chemically activated PMMA in chair time and periodontal outcomes [47]. These findings highlight the need to improve PMMA-based materials, notably via nanoparticle incorporation [48].

PMMA nanocomposites for provisional fixed restorations

Nanocomposites enable enhanced control over physical, mechanical, thermal, and biological properties compared to conventional materials lacking fillers (e.g., polymers, ceramics, metal alloys). PMMA's poor impact and fracture toughness necessitate reinforcement with synthetic or natural fillers like fibers, ceramics, and metal particles [49, 50]. Chen *et al.* (2010) suggested that increasing nanofiller concentration reduces resin matrix content, thereby decreasing shrinkage and improving mechanical properties [10]. Recent improvements in PMMA-based nanocomposites have broadened their clinical applications [51].

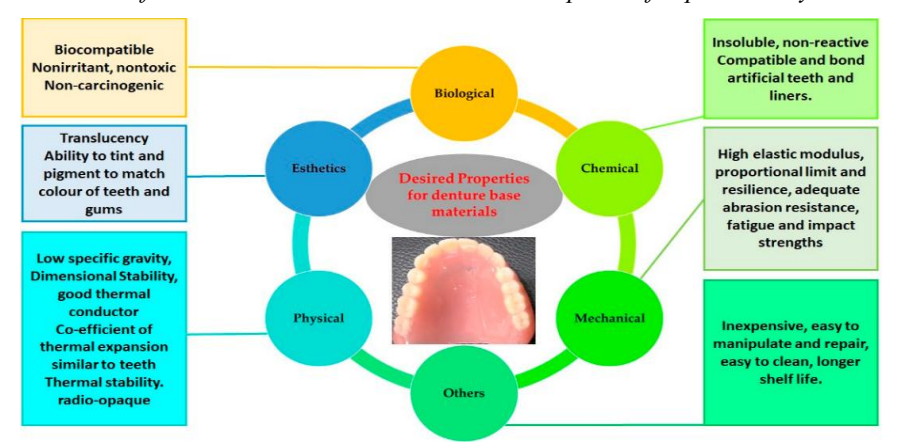


Figure 3. Desired characteristics of PMMA (Zafar, 2020 [45]).

Standardized tests to evaluate these materials include:

Flexural strength (FS) is a critical parameter in determining the longevity of prosthodontic appliances and their resistance to masticatory forces. It characterizes the performance of dental materials when subjected to bending forces. The International Organization for Standardization (ISO) and the American Society for Testing and Materials (ASTM International) have established guidelines for testing materials used in everyday dentistry. Among the essential parameters assessed is flexural strength [52-54]. Although alternative methods, such as biaxial testing, have been proposed, the ISOapproved three-point bending test remains the standard due to its reliability and widespread adoption [55, 56]. Table 1 summarizes findings from various studies that explore the relationship between nanoparticle concentration and flexural strength [55, 63-73]. Most studies indicate that increasing nanoparticle concentration enhances strength up to an optimal threshold, beyond which a slight decline is observed. Nevertheless, all modified specimens demonstrate superior FS compared to their unmodified counterparts.

This decrease at higher concentrations is likely attributed to nanoparticle agglomeration, forming larger clusters that reduce the material's efficiency. Surface modification of nanoparticles—such as silanization—can mitigate this effect by preventing excessive agglomeration. The extent of required surface treatment, such as silane application, is influenced by the nanoparticles' size and surface area. Jasim *et al.* (2014) [75] concluded that a direct correlation exists: larger surface areas demand higher silane concentrations to ensure adequate coverage and performance.

Gad *et al.* (2019) [76] conducted a systematic review on PMMA denture base materials modified with TiO₂ nanoparticles. Their findings underscore the need for further *in vivo* research to validate the 44

promising mechanical and clinical properties observed *in vitro*. These results align with earlier conclusions made by Gad *et al.* in 2017 [77].

Coupling agents such as silanes significantly enhance the bond between the polymer matrix and fillers, improving overall mechanical performance. However, some studies present differing views. Leão *et al.* (2019) [78] reported that silanization had no statistically significant effect on the mechanical properties of ZrO₂-filled composites, although they acknowledged improvements in flexural strength from nanoparticle incorporation.

Lohbauer *et al.* (2013) [79] suggested that limitations in mechanical properties often stem from deficiencies within the matrix itself, which can potentially be addressed through chemical modification of the composite. Akova *et al.* (2006) [80] investigated the impact of food-simulating solutions on provisional materials, finding that ethanol exposure significantly reduced flexural strength. These results highlight the influence of the oral environment and its dynamic conditions—such as dietary and masticatory functions—on the performance of provisional dental materials.

- ✓ <u>Hardness and microhardness</u> (MH) assess resistance to plastic deformation, critical for clinical wear resistance [81]. The Vickers microhardness test is widely used, following ISO and ASTM protocols [82, 83]. Most studies (Table 2) demonstrate that nanoparticle incorporation improves MH [57, 58, 63, 65, 66, 70, 73, 84–87]. Akova *et al.*'s findings on ethanol's deleterious effect on hardness further underline oral environment impacts [80].
- ✓ <u>Fracture toughness</u> (FT) indicates resistance to crack propagation under stress, essential for prosthesis durability [81]. Testing standards align with those for FS, with limited alternative method use [54-56, 88, 89]. Table 3 compiles data showing nanoparticle-enhanced FT in PMMA nanocomposites [66, 70, 72, 84, 90–93].

M. Dimova-Gabrovska et al.: Nanofiller concentration in PMMA-nanocomposites for preliminary dental restorations

Table 1. Studies comparing flexural strength of nanocomposites.

Author Test		Materials tested	Key findings		
Rodrigues et al 3 - point bending test 2008a [55]		Specimens of the composites Filtek Z250 TM and Filtek Supreme TM are light-cured.	Flexural strength of the microfilled composite Filtek $Z250^{TM}$ showed higher values than the one of the nanofilled composite Filtek Supreme TM .		
Hata et al 2022 [57]	3 - point bending test	PMMA-based resin with nanoporous silica filler particles. Specimens were obtained after light-curing in sizes 14 x 4 x 2 mm.	The specimens with added nanoporous silica filler have improved flexural strength property.		
Kim et al 2002 [58]	3 - point bending test	Different direct composites with varying morphologies of fillers were put in metal molds. Specimens were obtained after light-curing in sizes 2 x 2 x 25 mm.	Polymerized fillers lead to the lowest mechanical properties. Round fillers presented the highest flexural strength. However, increasing the filler concentration does not improve the mechanical properties.		
Orsi et al 2010 [59]	3 - point load test	Different PMMA-based composites were used in the study: Dencor, Duralay, and Trim Plus II. Specimens were obtained in sizes 65 x 10 x 3 mm. Sixty were loaded with glass fibers, and sixty were used as a control group.	The flexural strength of the specimens was not improved by adding glass filler fibers.		
Rodrigues et al 2008b [60]	4 - point bending test	Filtek Z250 tm .Z2 (microhybrid) and Filtek Supreme TM .SU (nanofill) composite specimens were compared.	The flexural strength of the specimens showed similar results - the nanofil composite presented a slightly lower result.		
Kumari et al 2024 [61]	3 - point bending test	PMMA with MgO nanoparticles with different particle concentrations is compared to non-modified PMMA. Specimens are in dimensions 1.3 cm (diameter) x 9 cm (length).	Nanofilled composite specimens showed improvement in the fracture toughness compared to the non-modified PMMA. The highest result was presented by 5 wt% MgO.		
Saen et al 2016 [62]	3 - point bending test 4 - point bending test	Bis-GMA/TEGDMA (70/30 wt%/wt%) and the corresponding nanocomposite containing 50 wt% of silanized Aerosil OX-50 silica. Nanosilica particles were silanised with γ-MPS.	Flexural strength is generally improved in the modified specimens. Another parameter was added in the testing technique speeding up of the test. A critical value is presented, after which flexural strength decreases.		
Jamel et al 2023 [63]	3 - point bending test	PMMA non-modified and modified with glass fibers (GF) and ZrO ₂ nanoparticles specimens are prepared in sizes 2 x 2 x 25 mm. The concentration of the different groups is as follows: group 1 (0% GF + 0% ZrO ₂), group 2 (0% GF + 5% ZrO ₂), group 3 (1% GF + 4% ZrO ₂), group 4 (2% GF + 3% ZrO ₂), group 5 (2.5% GF + 2.5% ZrO ₂), group 6 (3% GF + 2% ZrO ₂), group 7 (4% GF + 1% ZrO ₂), group 8 (5% GF + 0% ZrO ₂).	Flexural strength is generally improved in the modified specimens. The highest values are recorded in group 8 (5% GF + 0% ZrO ₂). A correlation between the increase in GF concentration and improvement of mechanical properties is observed.		
Balos et al 2020 [64]	3 - point bending test	PMMA non-modified and modified with nanosilica specimens are prepared in 0, 0.02, 0.05, 0.1, 0.2, 0.5, 0.7, 1, 1.5, 2, 2.5, 3, 5 wt%	Flexural strength is improved in the modified specimens, A peak mechanical performance is presented in the 0.05 and 2 wt%. An increase in nanoparticle concentration leads to a decrease in flexural strength. Therefore, the lowest mechanical properties are in the non-modified and the 5 wt% group.		
Alshahrani et al 2024 [65]	3 - point bending test	Auto-polymerizing acrylic resin is mixed with nano-SiO ₂ and nano-TiO ₂ with concentrations of 0, 1, 2.5 wt%.	Low nano-SiO ₂ addition shows improvement in the flexural strength. However, the 2.5 wt% of nano-SiO ₂ and both 1 and 2.5 wt% nano-TiO ₂ did not improve nor deprove the mechanical propertis.		
Zidan et al 2019 [66]	3 - point bending test	PMMA modified with ZrO ₂ specimens are prepared in a concentration of 0, 1.5, 3, 5, 7, 10 wt%.	An improvement in the flexural strength is presented in 1.5, 3, and 5 wt% groups, with a peak performance in the 3 wt% group. By increasing the concentration of the nanoparticles further a decrease in the mechanical property is presented.		
Barapatre et al 2022 [67]	3 - point bending test	PMMA modified with 3 wt% ZrO ₂ , 3 wt% Polyetheretherketone (PEEK), or 1.5 wt% ZrO ₂ and 1.5 wt% PEEK specimens are prepared in sizes 65 x 10x 2.5 mm.	The flexural strength improved in all modified specimens. The highest performance is shown in the hybrid group of 1.5 wt% ZrO_2 and 1.5 wt% PEEK.		
Gad et al 2016 [68]	3 - point bending test	Repair resin is modified with nanoparticles of ZrO ₂ with 2.5, 5, 7.5 wt% concentration.	The addition of ZrO_2 nanoparticles improved the flexural strength of the repair resin. The peak performance value is found in 7.5 wt% ZrO_2 .		
Ai et al 2016 [69]	3 - point bending test	Bis-GMA/TEGDMA composite is modified with 4- 10 wt% of polydopamine (PDA) - coated hydroxyapatite (HA) and added Ag nanoparticles (HA-PDA-Ag)	A significant improvement of the flexural strength is presented in the modified group.		
Thomaidis et al 2013 [70]	3 - point bending test	Specimens of the composites Filtek Z250, Filtek Ultimate, Admira and Majesty Posterior are compared.	Filtek Z-250 is presented with the highest flexural strength		
Kumar et al 2013 [71]	biaxial flexural strength	Different composites are compared after 1-week dry, 1-week wet, and 13-week wet storage. The specimens are in sizes 12 mm (diameter) and 1 mm (thickness).	Flexural strength declined in the modified nanocomposites after 1-week dry storage. Higher deformation is connected to the addition of nanofiller.		
Atai et al 2011 [72]	3 - point bending test	Microfilled, sintered nanosilica composite and Filtek Supreme composite are compared. Specimens are in sizes 2 x 2 x 25 mm and light-cured.	Both Filtek Supreme and nanosilica composite showed improved flexural strength compared to the microfilled composite.		
Alhavaz et al 2017 [73]	3 - point bending test	PMMA is reinforced with untreated Zr nanoparticles. Specimens are divided into groups of 0, 1, 2.5, 5 wt% Zr nanofiller.	Flexural strength is generally improved by adding untreated zirconia. It reaches a maximum at 2.5 wt% and a slight decline is visible in the 5 wt% group.		

 $\overline{\mbox{Abbreviations: wt\% - weight percentage; Bis-GMA - Bis-[4-(methacryloxypropoxy)-phenyl]-propane, TEGMA - triethyleneglycoldimethacrylate, γ-MPS - 3- Methacryloxypropyltrimethoxy-silane}$

M. Dimova-Gabrovska et al.: Nanofiller concentration in PMMA-nanocomposites for preliminary dental restorations

Table 2. Studies comparing hardness and microhardness of nanocomposites.

Author Test		Materials tested	Key findings		
Hata et al 2022 [57]	Vickers microhardness tester	PMMA-based resin with nanoporous silica filler particles. Specimens were obtained after light-curing in sizes 14 x 4 x 2 mm.	Microhardness in the modified specimens is improved compared to the non - modified ones.		
Kim et al 2002 [58]	Vickers microhardness tester	Different direct composites with varying morphologies of fillers were put in metal molds. Specimens were obtained after light-curing in sizes 5 x 1 mm.	Polymerized fillers lead to the lowest mechanical properties. Round fillers presented the highest flexural strength. However, increasing the filler concentration does not improve the mechanical properties.		
Jamel et al 2023 [63]	Vickers microhardness tester	PMMA non-modified and modified with glass fibers (GF) and ZrO ₂ nanoparticles specimens are prepared in sizes 9 (diameter) x 3 mm (thickness). The concentration of the different groups is as follows: group 1 (0% GF+ 0% ZrO ₂), group 2 (0% GF + 5% ZrO ₂), group 3 (1% GF + 4% ZrO ₂), group 4 (2% GF + 3% ZrO ₂), group 5 (2.5% GF + 2.5% ZrO ₂), group 6 (3% GF+ 2% ZrO ₂), group 7 (4% GF + 1% ZrO ₂), group 8 (5% GF + 0% ZrO ₂).	Microhardness is generally improved in the modified specimens. The highest values are recorded in group 8 (5% GF + 0% ZrO ₂). A correlation between the increase in GF concentration and improvement of mechanical properties is observed.		
Alshahrani et al 2024 [65]	Vickers hardness tester	Auto-polymerizing acrylic resin is mixed with nano-SiO ₂ and nano-TiO ₂ with concentrations of 0, 1, 2.5 wt%. Specimes are molded in sizes of $10 \times 10 \times 3.4$ mm.	Hardness is improved in all modified groups compared to non-modified resin.		
Zidan et al 2019 [66]	Vickers microhardness tester	PMMA modified with ZrO ₂ specimens are prepared in a concentration of 0, 1.5, 3, 5, 7, 10 wt%. Specimens are divided into two groups: 0-day dried, 7-day water immersion, and 45-day water immersion.	A direct correlation of the increase of the mechanical properties and the concentration of nanoparticles is found in the 0-day group. After water immersion a decrease in the hardness is found.		
Thomaidis et al 2013 [70]	Brinell hardness test	Specimens of the composites Filtek Z250, Filtek Ultimate, Admira and Majesty Posterior are compared.	Majesty Posterior is presented with the highest Brinell hardness.		
Alhavaz et al 2017 [73]	Vickers microhardness tester	PMMA is reinforced with untreated Zr nanoparticles. Specimens are divided into groups of 0, 1, 2.5, 5 wt% Zr nanofiller.	Microhardness is improved by adding nanofiller reinforcement in the PMMA base material.		
Balos et al 2014 [84]	Vickers microhardness tester	PMMA-based materials (Triplex Hot, Plyhot, Biocryl) with different dispersions of nanoparticles (0.023%, 0.046%, 0.091%, 0.23%, 0.46%, 0.92%). Specimens were cut in sizes 50 x 50 x 4 mm, using metalographic abrasive cutting machine and silicone carbide paper. A micrometer with an accuracy of 0.01 mm confirmed the sizing.	Microhardness has two peaks of performance at 0.023% and 0.91%. Overall, all modified specimens have improved microhardness compared to the original non-modified. The authors concluded that the results are obtained due to nanoparticle agglomeration formation, which increases the risk of cracks.		
Raj et al 2018 [85]	Durometer (ASTM)	PMMA/ZnO composite specimens were obtained in sizes 60 x 10 mm. The specimens have different concentrations of ZnO particles: 0, 1, 2, 5, 10, 15 wt %.	Hardness was improved in the 1 wt %, howevere, there was a slight decrease in the mechanical property for the others. In general, 2, 5 wt% groups showed improvements, 10 wt% - similar results to the control group and 15 wt% presented a decrease in the hardnes compared to the control group.		
Ayad et al 2008 [86]	Vickers microhardness tester	PMMA modified with ZrO ₂ rectangular models are prepared in sizes 30 x 10 x 2.5 mm.	The results of this study show similar statistical valueas of microhardness for non-modified and modified specimens.		
Elkhouly et al 2022 [87]	Vickers microhardness tester	PMMA reinforced nanocomposites with date seed nanoparticles (DSNP) and TiO ₂ nanoparticles are compared. The fillers are divided into groups with different concentrations of nanoparticles: 0, 0.3, 0.6, 0.9, 1.2 and 1.5 wt%.	1.2 wt% DSNP PMMA nanocomposite showed the highest mechanical properties compared to the TiO_2 .		

Abbreviations: wt% - weight percentage

Table 3. Studies comparing fracture toughness of nanocomposites.

Author	Test	Materials tested	Key findings	
Zidan et al 2019 [66]	Single-edge-notched bending method	PMMA modified with ZrO ₂ specimens are prepared in a concentration of 0, 1.5, 3, 5, 7, 10 wt%.	A decrease in the fracture toughness is presented in almost all groups is presented compared to the non-modified group. The 5 wt% group shows similar result as the control group.	
Thomaidis et al 2013 [70]	Single-edge-notched bending method	Specimens of the composites Filtek Z250, Filtek Ultimate, Admira and Majesty Posterior are compared.	Filtek Z-250 is presented with the highest fracture toughness.	
Atai et al 2011 [72]	Single-edge-notched bending method	Microfilled, sintered nanosilica composite and Filtek Supreme composite are compared. Specimens are in sizes 5 x 2 x 25 mm and light-cured.	Sintered nanosilica composite showed improved fracture toughness compared to the microfilled and Filtek Supreme composites.	
Balos et al 2014 [84]	4 - point bending test	PMMA-based materials (Triplex Hot, Plyhot, Biocryl) with different dispersions of nanoparticles (0.023%, 0.046%, 0.091%, 0.23%, 0.46%, 0.92%). Specimens were cut in sizes 50 x 50 x 4 mm, using metalographic abrasive cutting machine and silicone carbide paper. A micrometer with an accuracy of 0.01 mm confirmed the sizing.	Fracture toughness improved with 0.023% addition of nanosilica particles compared to the initial non - modified material. The three different PMMA - based materials showed simillar results. By increasing the value of nanoparticles the fracture toughness decreases. The authors conclude that the mair reason for the results of the study is the particle agglomeration which leads to crack formation. Alverall, all modified specimens have improved their fracture toughness compared to the non-modified one.	
Topouzi et al 2017 [90]	3 - point bending test (single-edge notched method)	PMMA modified with silica nanoparticles samples are prepared with size 3 x 6 x 25 mm with a pre-crack perpendicular to the length and depth of 3 mm. Silica nanoparticles are devided into non-modified (SIL) and modified with trietoxyvinylsilane (T-SIL). Each group consists of specimens with 0.25%, 0.50%, 0.75% and 1 wt%.	An improvement in fracture toughness is recorded in the modified PMMA. PMMA/T-SIL with 0.25% nanoparticles presented the highest mechanical properties.	
Xu et al 2002 [91]	Single-edge-V- notched beam method	Seven silica powders with ratio of whiskers:silica mass 0:1, 1:5, 1:2, 1:1, 2:1, 5:1, 1:0 are silanised. They are mixed manually with Bis-GMA, TEGDMA and others	An improvement in fracture toughness is recorded in the specimens. The increase reached a constant plateau when the whiskers:silica ratio reached 1:0. It is deduced that this phenomenon is due to the agglomeration of whiskers. This can lead to a need for the prevention of the entanglement of the nanoparticles.	
Protopapa et al 2011 [92]	3 - point bending test (single-edge notched method)	PMMA reinforced with nanodiamonds specimens with concentrations of 0.10, 0.38, 0.50, 0.83% wt are tested.	An improvement in fracture toughness is recorded in the modified specimens. The highest results are shown in the 0.1 %wt group. Therefore, a lower nanodiamonds concentration leads to higher mechanical properties of PMMA-composites.	
Alhotan et al 2021 [93]	3 - point bending test (single-edge notched method)	PMMA reinforced with TiO ₂ and ZrO ₂ nanoparticles, and E-glass-fibres specimens with concentrations of 1.5, 3, 5, 7 wt % are tested. The sizes of the specimens were 40 x 8 x 4 mm	An improvement in fracture toughness is recorded in the modified specimens.	

Abbreviations: wt% - weight percentage

Biological characteristics. Nanocomposites affect oral microenvironment homeostasis and must exhibit biocompatibility, measured via cytotoxicity tests. Higher residual monomer correlates with increased cytotoxicity [54, 95]. Maintaining healthy gingiva and marginal integrity is critical for periodontal health and treatment success [96, 97]. Balos et al. observed decreased cell viability at higher nanoparticle concentrations, indicating potential inflammation risks [64]. Conversely, modifications with antibacterial agents (e.g., silver nanoparticles) can enhance antimicrobial effects while maintaining low cytotoxicity [69]. Zhang et al. demonstrated that silanized nano-hydroxyapatite improves **PMMA** biocompatibility osteointegration stimulation [98, 99]. De Castro et al. reported ion release proportional to AgVO₃ concentration, suggesting controlled filler levels

reduce cytotoxicity [100]. Surface protein adsorption modulates cellular response; nanohydroxyapatite doping improves surface texture and adhesion, favoring periodontal health [99, 101]. Nanocomposites also display antimicrobial activity against cariogenic bacteria (*S. mutans, L. acidophilus*), though simultaneous cytotoxicity evaluation remains essential [102]. Hydrophobic glass nanofillers reduce water sorption, influencing aesthetics and material longevity [103].

✓ <u>Digital technologies.</u> Additive manufacturing (3D printing) and subtractive CAD/CAM technologies enable rapid, precise fabrication of provisional restorations [2]. Some 3D-printed resins (e.g., Saremco print - CROWNTEC, Temp PRINT) exhibit superior mechanical properties over conventional analog materials, though variations exist [104]. Nanoparticle reinforcement, such as

ZrO₂ doping, improves microhardness and flexural modulus but may alter aesthetics [105–107]. Mechanical performance depends on base resin and filler characteristics [108, 109]. Production methods affect mechanical properties; digital light processing (DLP) and stereolithography (SLA) yield improved flexural strength compared to conventional or subtractive methods [110, 111]. Build orientation influences strength and elastic modulus, with 0° preferred for flexural strength and 90° for elasticity [111]. Food-simulating solutions impact 3D-printed resin properties, necessitating further study [112]. Compared to milled CAD/CAM restorations, 3Dprinted materials often show superior wear resistance and surface smoothness, though findings inconclusive overall [113–116]. restorations typically offer better marginal fit, essential to periodontal health, which can be optimized by adjusting layer thickness in 3D printing [117–120].

CONCLUSIONS

Based on the comprehensive review and analysis of the current scientific literature, several essential conclusions can be drawn regarding the role of PMMA-based and other nanocomposites in contemporary dentistry, particularly in the fabrication of preliminary restorations.

Firstly, PMMA-based nanocomposites are fundamental to modern dental materials science. Their widespread application in prosthodontics, especially in temporary restorations, is attributed to their favorable handling properties, aesthetics, and cost-effectiveness. However, pure PMMA presents notable limitations, including poor mechanical performance, high polymerization shrinkage, and suboptimal biological compatibility. The incorporation of nanoparticles addresses many of these shortcomings, providing a viable pathway for performance enhancement.

Secondly, nanoengineering has emerged as a transformative approach in the development of dental materials. The addition of various nanofillers-such as TiO₂, ZrO₂, silver, hydroxyapatite, and glass can significantly improve mechanical properties like flexural strength, hardness, and fracture toughness. Furthermore, biological behaviors such as cytocompatibility and antibacterial activity can be tailored by modifying the filler composition and surface characteristics. Nevertheless, the optimization of filler concentration and surface treatment (e.g., silanization) is critical to avoid issues like agglomeration and increased cytotoxicity.

Thirdly, the exploration of nanotechnology's full potential in dentistry is still ongoing. While promising results have been observed *in vitro*, there remains a need for more *in vivo* and clinical studies to validate the long-term effectiveness and safety of these materials. Digital manufacturing technologies, including CAD/CAM and 3D printing, further expand the application of nanocomposites by improving production accuracy, reducing clinical chair time, and enhancing patient outcomes.

In conclusion, PMMA-based nanocomposites represent a dynamic and evolving area of dental materials research. Their continued development, driven by advancements in nanoscience and digital fabrication, holds significant potential for improving the quality, durability, and biological performance of provisional restorations. As new discoveries emerge, these materials are likely to become even more integral to personalized, efficient, and patient-centered dental care.

REFERENCES

- O. Schierz, C. Hirsch, K. F. Krey, C. Ganss, P.W. Kämmerer, M. A. Schlenz, *Journal of Evidence-Based Dental Practice*, 24(1), 101946 (2024).
- Y. Tian, C. Chen, X. Xu, J. Wang, X. Hou, K. Li, H.B. Jiang, *Scanning*, 2021(1), 9950131 (2021).
- 3. A.A. Balhaddad, I.M. Garcia, L. Mokeem, R. Alsahafi, A. Majeed-Saidan, H.H. Albagami, M.A.S. Melo, *Clinical Oral Investigations*, **27(6)**, 2465 (2023).
- 4. M. Jeong, K. Radomski, D. Lopez, J.T. Liu, J.D. Lee, S. J. Lee, *Dentistry Journal*, **12(1)**, 1 (2023).
- M. Dimova, *Folia Medica*, Plovdiv, Tomus XXXX A, 3, 145 (1998).
- 6. D. Dimitrova, M. Dimova-Gabrovska, L. Maksimovskaya, *Comptes rendus de l'Académie bulgare des Sciences*, **74(2)**, 300 (2021).
- 7. M. Dimova-Gabrovska, D. Dimitrova, B. Yordanov, M. Yankova, T. Peev, *Journal of IMAB–Annual Proceeding Scientific Papers*, **25(3)**, 2675 (2019).
- 8. M. Dimova, *Pharmacology online*, **(3)**, 524 (2011).
- 9. M. Dimova-Gabrovska, *Comptes rendus de l'Académie bulgare des Sciences*, **74(5)**, 784 (2021).
- 10. M.H. Chen, *Journal of Dental Research*, **89(6)**, 549 (2010).
- 11. A.M. Asiri, A. Mohammad (eds.), Applications of nanocomposite materials in dentistry, 11 Nanocomposites: Past, present, and future of dentistry, Woodhead Publishing, 2018, p. 181.
- 12. S.A. Saunders, *Clinical*, *Cosmetic and Investigational Dentistry*, **1**, 47 (2009).
- 13. J. Ivanova, V. Valeva, T. Petrova, W. Becker, Water and Environmental Systems (SDEWES), September 22-27, (2013), Dubrovnik, Croatia, 0929-1-0979-12.
- 14. J. Ivanova, V. Valeva, A. Yanakieva, T. Petrova, W. Becker, *Journal of Sustainable Development of Energy, Water and Environment Systems*, **4(1)**, 23 (2016).

- 15. E. Kirilova, T. Petrova, W. Becker, J. Ivanova, *ZAMM J. Appl. Math. Mech.*, **97(9)**, 1136 (2017).
- 16. E. Kirilova, W. Becker, J. Ivanova, T. Petrova, *CE/papers*, **1(4)**, 438 (2017).
- 17. T. Petrova, W. Becker, E. Kirilova, J. Ivanova, *CE/papers*, **1(4)**, 487 (2017).
- 18. J. Ivanova, T. Petrova, E. Kirilova, W. Becker, *Engineering Transactions*, **65(1)**, 97 (2017).
- 19. E. Kirilova, T. Petrova, W. Becker, J. Ivanova, *IOP Conference Series: Materials Science and Engineering (MSE)*, **461(1)**, 012029-1-012029-8, (2018).
- 20. T. Petrova, E. Kirilova, W. Becker, J. Ivanova, *IOP Conference Series: Materials Science and Engineering (MSE)*, **461(1)**, 012067-1-012067-8 (2018).
- 21. U. Ali, K.J.B.A. Karim, N.A. Buang, *Polymer Reviews*, **55(4)**, 678 (2015).
- D. Astudillo-Rubio, A. Delgado-Gaete, C. Bellot-Arcís, J.M. Montiel-Company, A. Pascual-Moscardó, J.M. Almerich-Silla, *PLoS One*, 13(2), e0193162 (2018).
- 23. R.P. Feynman, *Engineering and Science*, **23(5)**, 22 (1960).
- 24. R.A. Freitas Jr, *The Journal of the American Dental Association*, **131(11)**, 1559 (2000).
- 25. D. Ure, J. Harris, *Dental update*, **30(1)**, 10 (2003).
- 26. S. Kumar, P. Bhushan, S. Bhattacharya, in: Environmental, chemical and medical sensors, Singapore, Springer Singapore, 2017, p. 167.
- 27. S.B. Mitra, D. Wu, B.N. Holmes, *The Journal of the American Dental Association*, **134(10)**, 1382 (2003).
- 28. R. Indiarto, L.P.A. Indriana, R. Andoyo, E. Subroto, B. Nurhadi, *European Food Research and Technology*, **248(1)**, 1 (2022).
- 29. N. Abid, A.M. Khan, S. Shujait, K. Chaudhary, M. Ikram, M. Imran, M. Maqbool, *Advances in Colloid and Interface Science*, **300**, 102597 (2022).
- 30. R. Vijayalakshmi, S. Kumar, *Indian Journal of Dental Research*, **17(2)**, 62 (2006).
- 31. O.E. Ogle, N. Byles, *The West Indian Medical Journal*, **63(4)**, 344 (2015).
- 32. G. Dipalma, A.D. Inchingolo, M. Guglielmo, R. Morolla, I. Palumbo, L. Riccaldo, F. Inchingolo, *Journal of Clinical Medicine*, **13(17)**, 5268 (2024).
- 33. A. Shalini, R.D. Denin, *Int. J. Prostho Rehabil.*, **1**, 14 (2020).
- 34. A. Besinis, T. De Peralta, C.J. Tredwin, R.D. Handy, *ACS nano*, **9(3)**, 2255 (2015).
- 35. B. Ali Sabri, M. Satgunam, N. M. Abreeza, N.A. Abed, *Cogent Engineering*, **8(1)**, 1875968 (2021).
- 36. S. Miura, M. Fujisawa, F. Komine, T. Maseki, T. Ogawa, J. Takebe, Y. Nara, *Journal of Oral Science*, **61(2)**, 195 (2019).
- 37. P. Ford, G. Seymour, J.A. Beeley, F. Curro, D. DePaola, D. Ferguson, N. Claffey, *European Journal of Dental Education*, **12**, 40 (2008).
- 38. M. Shetty, H. Alva, A. Prasad, *Journal of Health and Allied Sciences NU*, **2(02)**, 72 (2012).

- 39. M.C. Hacker, A.G. Mikos, *In: Principles of Regenerative Medicine*, 2nd Edition, Academic Press, San Diego, Synthetic Polymers, 2011, p. 587.
- D.R. Federick, The Journal of Prosthetic Dentistry, 34(5), 520 (1975).
- 41. M. Patras, O. Naka, S. Doukoudakis, A. Pissiotis, *Journal of Esthetic and Restorative Dentistry*, **24(1)**, 26 (2012).
- 42. S.D. Miller, *The Journal of Prosthetic Dentistry*, **50(4)**, 516 (1983).
- 43. D. Agop-Forna, P.S. Popa, G.V. Popa, *Medicine and Materials*, **4(2)**, 77 (2024).
- 44. J.G.E. Hendriks, J.R. van Horn, H.C. van der Mei, H. J. Busscher, *Biomaterials*, **25(3)**, 545 (2004).
- 45. M.S. Zafar, *Polymers*, **12**, 2299 (2020).
- 46. M. Balkenhol, M.C. Mautner, P. Ferger, B. Wöstmann, *Journal of Dentistry*, **36(1)**, 15 (2008).
- 47. L. Barqawi, S. Kanot, Cureus, 16(6), e63455 (2024).
- 48. A.P.P. Fugolin, C.S. Pfeifer, *Journal of Dental Research*, **96(10)**, 1085 (2017).
- 49. M.R. Mohammed, A.N. Hadi, *American Scientific Research Journal for Engineering, Technology, and Sciences (ASRJETS)*, **78(1)**, 165 (2021).
- 50. R. Yadav, A. Meena, A. Patnaik, *Polymers for Advanced Technologies*, **33(6)**, 1762 (2022).
- 51. A. Burcea, A.M. Bănățeanu, C.V. Poalelungi, N. Forna, C.N. Cumpătă, *Romanian Journal of Oral Rehabilitation*, **16(4)**, 11 (2024).
- 52. International Organization for Standardization. (2019). ISO 178:2019 Plastics Determination of flexural properties. ISO. https://www.iso.org/standard/70513.html
- 53. ASTM International. (2022). ASTM C78/C78M-22: Standard test method for flexural strength of concrete (using simple beam with third-point loading). West Conshohocken, PA: ASTM International. https://doi.org/10.1520/C0078 C0078M-22
- 54. M. Hassan, M. Asghar, S.U. Din, M.S. Zafar, in: Materials for Biomedical Engineering, Elsevier, 2019, p. 273.
- 55. S.A. Rodrigues Jr, J.L. Ferracane, A. Della Bona, *Dental Materials*, **24(3)**, 42:6 (2008a).
- 56. S.M. Chung, A.U.J. Yap, S.P. Chandra, C.T. Lim, *Journal of Biomedical Materials Research Part B: Applied Biomaterials*, **71(2)**, 278 (2004).
- 57. K. Hata, H. Ikeda, Y. Nagamatsu, C. Masaki, R. Hosokawa, H. Shimizu, *Journal of Functional Biomaterials*, **13(1)**, 32 (2022).
- 58. K.H. Kim, J.L. Ong, O. Okuno, *The Journal of Prosthetic Dentistry*, **87(6)**, 642 (2002).
- 59. I.A. Orsi, R.G. Soares, C.A. Villabona, H. Panzeri, *Gerodontology*, **29(2)**, e63 (2012).
- 60. S.A. Rodrigues Jr, S.S. Scherrer, J.L. Ferracane, A. Della Bona, *Dental Materials*, **24(9)**, 1281 (2008b).
- 61. S. Kumari, R.K. Mishra, S. Parveen, S.K. Avinashi, A. Hussain, S. Kumar, M. Banerjee, J. Rao, R. Kumar, R.K. Gautam, C. Gautam, *Scientific Reports*, **14(1)**, 2128 (2024).
- 62. P. Saen, M. Atai, A. Nodehi, L. Solhi, *Dental Materials*, **32(8)**, e185 (2016).

- 63. R.S. Jamel, M.A. Al-Murad, E.F. Alkhalidi, *The Saudi Dental Journal*, **35(6)**, 707 (2023).
- 64. S., Balos, T. Puskar, M. Potran, B. Milekic, D. Djurovic Koprivica, J. Laban Terzija, I. Gusic, *Coatings*, **10(6)**, 583. (2020).
- 65. F.A. Alshahrani, M. AlGhamdi, D. Alghamdi, H. Alshammary, S. Akhtar, S.Q. Khan, A.A. Mahrous, F. Alzoubi, A.N.M. Emam, M.M. Gad, *Prosthesis*, **6(4)**, 952 (2024).
- S. Zidan, N. Silikas, A. Alhotan, J. Haider, J. Yates, *Materials*, 12(8), 1344 (2019).
- 67. D. Barapatre, S. Somkuwar, S. Mishra, R. Chowdhary, *European Oral Research*, **56(2)**, 61 (2022).
- 68. M.M. Gad, A. Rahoma, A.M. Al-Thobity, AS. *International Journal of Nanomedicine*, 5633 (2016).
- 69. M. Ai, Z. Du, S. Zhu, H. Geng, X. Zhang, Q. Cai, X. Yang, *Dental Materials*, **33(1)**, 12 (2017).
- 70. S. Thomaidis, A. Kakaboura, W.D. Mueller, S. Zinelis, *Dental Materials*, **29(8)**, e132 (2013).
- 71. N. Kumar, A. Shortall, *Journal of Investigative and Clinical Dentistry*, **5(3)**, 237 (2014).
- 72. M. Atai, A. Pahlavan, N. Moin, *Dental Materials*, **28(2)**, 133 (2012).
- 73. A. Alhavaz, M. Rezaei Dastjerdi, A. Ghasemi, A. Ghasemi, A. Alizadeh Sahraei, *Journal of Esthetic and Restorative Dentistry*, **29(4)**, 264 (2017).
- K.S. Chan, Y.D. Lee, D.P. Nicolella, B.R. Furman,
 S. Wellinghoff, R. Rawls, *Engineering fracture mechanics*, 74(12), 1857 (2007).
- 75. B.S. Jasim, I.J. Ismail, *Journal of Baghdad College of Dentistry*, **26(2)**, 18 (2014).
- 76. M.M. Gad, R. Abualsaud, *International Journal of Biomaterials*, **2019(1)**, 6190610 (2019).
- M.M. Gad, S.M. Fouda, F.A. Al-Harbi, R. Näpänkangas, A. Raustia, *International Journal of nanomedicine*, 12, 3801 (2017).
- 78. R. de Souza Leão, S.L.D. de Moraes, J.M. de Luna Gomes, C.A.A. Lemos, B.G. da Silva Casado, B.C. do Egito Vasconcelos, E.P. Pellizzer, *Materials Science and Engineering: C*, **106**, 110292 (2020).
- 79. U. Lohbauer, R. Belli, J.L. Ferracane, *Journal of Dental Research*, **92(7)**, 584 (2013).
- 80. T. Akova, A. Ozkomur, H. Uysal, *Dental materials*, **22(12)**, 1130 (2006).
- 81. N. Ilie, T.J. Hilton, S.D. Heintze, R. Hickel, D.C. Watts, N. Silikas, J.W. Stansbury, M. Cadenaro, J.L. Ferracane, *Dental Materials*, **33(8)**, 880 (2017).
- 82. International Organization for Standardization. (2019). ISO/TS 19278:2019 Plastics Instrumented micro-indentation test for hardness measurement. https://www.iso.org/standard/64253.html
- 83. ASTM International. (2022). ASTM E384-22: Standard test method for microindentation hardness of materials. https://doi.org/10.1520/E0384-22
- 84. S. Balos, B. Pilic, D. Markovic, J. Pavlicevic, O. Luzanin, *The Journal of Prosthetic Dentistry*, **111(4)**, 327 (2014).

- 85. I. Raj, M. Mozetic, V.P. Jayachandran, J. Jose, S. Thomas, N. Kalarikkal, *Nanotechnology*, **29(30)**, 305704 (2018).
- N.M. Ayad, M. F. Badawi, A.A. Fatah, Revista Clínica de Pesquisa Odontológica, 4(3), 145 (2008).
- 87. H.I. Elkhouly, E.M. Ali, M.N. El-Sheikh, A.E.S.M. Hassan, *Scientific Reports*, **12(1)**, 16416 (2022).
- 88. International Organization for Standardization. (2018). ISO 13586:2018 Plastics Determination of fracture toughness (GIC and KIC) Linear elastic fracture mechanics (LEFM) approach (2nd edn.). ISO. https://www.iso.org/standard/71194.html
- 89. ASTM International. (2018). ASTM E1820-18: Standard test method for measurement of fracture toughness. https://doi.org/10.1520/E1820-18
- 90. M. Topouzi, E. Kontonasaki, D. Bikiaris, L. Papadopoulou, K.M. Paraskevopoulos, P. Koidis, *Journal of the mechanical behavior of biomedical materials*, **69**, 213 (2017).
- 91. H.H. Xu, J.B. Quinn, D.T. Smith, J.M. Antonucci, G.E. Schumacher, F.C. Eichmiller, *Biomaterials*, **23(3)**, 735 (2002).
- 92. P. Protopapa, E. Kontonasaki, D. Bikiaris, K.M. Paraskevopoulos, P. Koidis, *Dental Materials Journal*, **30(2)**, 222 (2011).
- 93. A. Alhotan, J. Yates, S. Zidan, J. Haider, N. Silikas, *Materials*, **14(15)**, 4127 (2021).
- A. Besinis, T. De Peralta, C.J. Tredwin, R.D. Handy, ACS nano, 9(3), 2255 (2015).
- 95. U. Kedjarune, N. Charoenworaluk, S. Koontongkaew, *Australian Dental Journal*, **44(1)**, 25 (1999).
- 96. S. Gracis, M. Fradeani, R. Celletti, G. Bracchetti, *Periodontology*, **27(1)**, 29 (2001).
- S.M. Pituru, M. Greabu, A. Totan, M. Imre, M. Pantea, T. Spinu, A.M.C. Tancu, N.O. Popoviciu, I.I. Stanescu, E. Ionescu, *Materials*, 13(13), 2894 (2020).
- 98. J. Zhang, J. Liao, A. Mo, Y. Li, J. Li, X. Wang, *Applied Surface Science*, **255(2)**, 328 (2008).
- 99. C.J. Wilson, R.E. Clegg, D.I. Leavesley, M.J. Pearcy, *Tissue Engineering*, **11(1-2)**, 1 (2005).
- 100.D.T. de Castro, M.L.D.C. Valente, C.P. Aires, O.L. Alves, A.C. Dos Reis, *Gerodontology*, **34(3)**, 320 (2017).
- 101.L.T. Allen, M. Tosetto, I.S. Miller, D.P. O'Connor, S.C. Penney, I. Lynch, A.K. Keenan, S.R. Pennington, K.A. Dawson, W.M. Gallagher, *Biomaterials*, 27(16), 3096 (2006).
- 102. A. Sodagar, S. Khalil, M.Z. Kassaee, A.S. Shahroudi, B. Pourakbari, A. Bahador, *Journal of Orthodontic Science*, **5(1)**, 7 (2016).
- 103.D.A. Prodan, C. Gasparik, D.C. Mada, V. Miclăuş, M. Băciuţ, D. Dudea, *Clinical Oral Investigations*, **19**, 867 (2015).
- 104.K.A. Tavuz, N.A.H. Husain, K.J. Mätzener, M.M. Ateş, T.F. Eyüboğlu, M. Özcan, *Journal of the Mechanical Behavior of Biomedical Materials*, **161**, 106817 (2025).
- 105.S. Aati Z. Akram H. Ngo A.S. Fawzy, *Dental Materials*, **37(6)**, e360 (2021).

- 106.A. Alshamrani, A. Alhotan, E. Kelly, A. Ellakwa, *Polymers*, **15(11)**, 2523 (2023).
- 107.M.A. AlGhamdi, F.M. Alatiyyah, R.F. Almedarham, Z.H. Al Dawood, F.Y. Alshaikhnasser, S.Y. Alboryh, S.Q. Khan, R. Abualsaud, M.M. Gad, *Nanomaterials*, **14(8)**, 665 (2024).
- 108.R.S. Saini, V. Gurumurthy, S.A. Quadri, S.S. Bavabeedu, K.M. Abdelaziz, A. Okshah, A.A.F. Alshadidi, L. Yessayan, S.A. Mosaddad, A. Heboyan, *BMC Oral Health*, **24(1)**, 66. (2024).
- 109.A. Tahayeri, M. Morgan, A.P. Fugolin, D. Bompolaki, A. Athirasala, C.S. Pfeifer, L.E. Bertassoni, *Dental Materials*, **34(2)**, 192 (2018).
- 110.S.M. Park, J.M. Park, S.K. Kim, S.J. Heo, J.Y. Koak, *Materials*, **13(18)**, 3970 (2020).
- 111.R.F. Almedarham, Z. H. Al Dawood, F.M. Alatiyyah, S. Akhtar, S.Q. Khan, A.C. Shetty, M. M. Gad, *The Saudi Dental Journal*, **36(11)**, 1417 (2024).
- 112.M. Eser, S.Ç. Öge, O. Ekren, *The International Journal of Prosthodontics*, **37(7)**, 71 (2024).
- 113. A. Besinis, T. De Peralta, C. J. Tredwin, R. D. Handy, *ACS nano*, **9(3)**, 2255 (2015).

- 114.S. Jain, M.E. Sayed, M. Shetty, S.M. Alqahtani, M.H. D. Al Wadei, S.G. Gupta, M.F. Sheayria, *Polymers*, **14(13)**, 2691 (2022).
- 115.E. Göncü Başaran, E. Ayna, P.K. Vallittu, L.V. Lassila, *Acta Odontologica Scandinavica*, **69(3)**, 144 (2011).
- 116.B. Stawarczyk, A. Ender, A. Trottmann, M. Özcan, J. Fischer, C. H. Hämmerle, *Clinical Oral Investigations*, **16**, 1669 (2012).
- 117.S.J. Alzahrani, M.S. Hajjaj, A.A. Azhari, W.M. Ahmed, H.E. Yeslam, R.M. Carvalho, *Bioengineering*, **10(6)**, 663 (2023).
- 118.S. Jain, M.E. Sayed, M. Shetty, S.M. Alqahtani, M. H.D. Al Wadei, S.G. Gupta, A.A.A. Othman, A.H. Alshehri, H. Alqarni, A.H. Mobarki, K. Motlaq, H.F. Bakmani, A.A. Zain, A.J. Hakami, M.F. Sheayria, *Polymers*, 14(13), 2691 (2022).
- 119.H. Al-Humood, A. Alfaraj, C.C. Yang, J. Levon, T.M.G. Chu, W.S. Lin, *Materials*, **16(5)**, 1996. (2023).
- 120.M. Hasanzade, N. Yaghoobi, P. Nematollahi, R. Ghazanfari, *Clinical and Experimental Dental Research*, **9(5)**, 832 (2023).

Thermal effects on concrete nanocomposites with central inclined cracks: Influence of crack geometry and nano-SiO₂ content

G. N. Nikolova*

Institute of Mechanics, Bulgarian Academy of Sciences, Sofia, Bulgaria

Received: May 03 2025; Revised: July 11, 2025

This study presents a parametric analysis of the energy release rate (ERR) in concrete nanocomposites containing nano-SiO₂ (1.0%, 1.5%, and 2.0%), with a centrally located crack of varying length and orientation angle (0°, 30°, 45°), under thermal loading. A mathematical model based on linear elastic fracture mechanics (LEFM) was developed, and numerical simulations were performed using Wolfram Mathematica. Thermal stresses were estimated under the assumption of fully constrained thermal expansion, where the temperature rise ΔT is considered as a local uniform increase with respect to a reference state. Only the magnitude of the thermal stress is used in ERR calculations. The study focuses on how ERR values respond to variations in crack geometry, temperature increase, and nanoparticle content. Results indicate that ERR increases with crack length and thermal load but decreases with crack inclination angle. The composite with 1.0% nano-SiO₂ generally exhibits the lowest ERR values in the tested configurations. Although fracture toughness is not experimentally determined in this work, the findings provide a preliminary basis for evaluating the influence of crack geometry and thermal stress on ERR, and for guiding the optimization of thermally resistant concrete nanocomposites.

Keywords: Concrete nanocomposite, 1%, 1.5% and 2% nano-SiO₂, Central crack, LEFM, Numerical results, SIF and ERR

INTRODUCTION

Concrete nanocomposites with added nano-SiO₂ are advanced construction materials that exhibit enhanced mechanical, thermal, and long-term performance compared to ordinary concrete. They are particularly relevant for sustainable and energy-efficient infrastructure, contributing to reduced resource consumption and extended service life [1]. In recent years, numerous studies have focused on the influence of nanoparticles on the mechanical and microstructural properties of concrete [2–8].

The addition of nano-SiO₂ to concrete mixtures leads to an increase in the elastic modulus and a decrease in the coefficient of thermal expansion, which improves the microstructure, enhances density, and reduces porosity, thereby increasing mechanical strength and resistance to cracking.

Thermal loading plays a significant role in crack formation and propagation in concrete structures. While many studies have explored the evaluation of SIF and ERR for various materials, there is still insufficient data on the thermal fracture behavior of nano-SiO₂-modified concrete under idealized thermal conditions, particularly in relation to crack geometry and particle concentration [6, 7, 9, 10].

In this study, thermal stresses are not derived from a real heat conduction problem but are estimated using an idealized approach assuming a uniform temperature increase ΔT throughout the volume, corresponding to a fully constrained expansion scenario. The value of ΔT is interpreted as a local temperature rise with respect to a reference state (e.g., room temperature), not as a vertical temperature gradient. This approximation allows for simplified evaluation of the magnitude of thermal stress and its effect on fracture parameters without resolving the detailed thermal field.

It is important to note that only the absolute value of thermal stress is used in the ERR and SIF calculations, and the influence of restraint conditions is represented in a conservative manner.

Crack geometry, including length and inclination angle, significantly affects stress distribution and crack growth tendencies in nanocomposites.

Analytical and numerical methods for determining stresses, strains, SIF, and ERR are essential for predicting crack initiation and growth, and for evaluating the thermal and mechanical reliability of concrete and other nanostructured materials [11–20].

Reference [11] is a foundational work introducing the concept of SIF and its application to cracks of various geometries. Reference [12] provides key principles of fracture mechanics, including stress concentration analysis and crack propagation. The book [13] discusses fracture mechanics under combined mechanical and thermal

^{*} To whom all correspondence should be sent: E-mail: gery@imbm.bas.bg

stresses, presenting key formulations. Publications [14] and [15] further develop analytical modelling in this field. The handbook [16] offers detailed formulas and examples for SIF calculation, including the effects of temperature-induced stresses. Reference [17] discusses different approaches to modelling thermal—mechanical interactions in cracked materials and computing corresponding SIF values.

Temperature gradients across concrete structures can generate internal thermal stresses that drive crack initiation and growth. Understanding how temperature influences SIF and ERR in nanomodified concrete is essential for assessing its structural reliability and long-term performance.

The formulation used in this study should be viewed as a simplified analytical model aimed at exploring parametric trends under thermal loading, rather than a full representation of thermomechanical coupling in real structures.

The aim of this study is to perform a parametric analysis of the influence of temperature, crack length, and orientation angle, along with different nano-SiO₂ contents, on thermal stress and energy release rate (ERR) in a concrete nanocomposite containing a centrally located inclined crack.

PROBLEM FORMULATION

The geometric model of a concrete nanocomposite with a central inclined crack under monotonic thermal loading ΔT is presented in Figure 1.

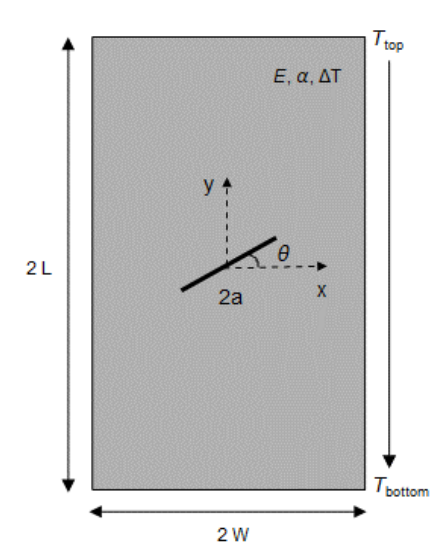


Figure 1. Geometric model of a concrete nanocomposite with a centrally located inclined crack under monotonic thermal loading ΔT .

The nanocomposite is modelled as a rectangular plate with width 2W, length 2L and a central crack with length 2a, oriented at an angle θ relative to the

horizontal x-axis. The x and y axes of the Oxy coordinate system used in the model are represented by dashed lines, with the origin positioned at the midpoint of the crack. The x-axis spans the width $(x \in [-W, W])$, and the y-axis spans the height of the plate $(y \in [-L, L])$, with the positive y-direction pointing upwards.

The thermal loading ΔT is defined as a temperature difference between the top surface (T_{top}) and the bottom surface (T_{bottom}) , i.e., $\Delta T = T_{top} - T_{bottom}$.

In the numerical model, this is treated as a vertical thermal gradient, which induces internal thermal stresses due to constrained thermal expansion of the material.

In contrast, the analytical model interprets ΔT as a local, uniform temperature rise at the crack location, relative to a reference state (e.g., ambient temperature). Under the assumption of fully restrained thermal expansion, this approximation allows for simplified estimation of the thermal stress magnitude and its effect on fracture parameters. This modelling approach is conservative and commonly used for preliminary parametric analysis. The direction of the temperature gradient is indicated in Figure 1.

The coordinate system is centered at the midpoint of the crack. In the case of a horizontal crack ($\theta=0^{\circ}$), the geometry is symmetric with respect to both axes. For inclined cracks ($\theta>0^{\circ}$), symmetry with respect to the x-axis is preserved, but the overall geometry becomes asymmetric, particularly in terms of heat transfer, which is considered in the numerical analysis.

The orientation angle θ is defined as the angle between the crack line and the horizontal axis (x-axis), measured in a counterclockwise direction. In this configuration, $\theta=0^\circ$ corresponds to a horizontal crack perpendicular to the vertical thermal gradient. In the present analysis, three angles are considered: $\theta=0^\circ$, 30°, and 45°, representing increasing crack inclination relative to the temperature gradient direction. These configurations are illustrated schematically in Figure 1.

BASIC EQUATIONS

Thermal stress

The thermal stress induced by the load is determined by Hooke's law using the following expression:

$$\sigma_T = E. \alpha . \Delta T$$
 (1)

where σ_T denotes the thermal stress, E is the modulus of elasticity of the concrete nanocomposite,

 α - the coefficient of linear thermal expansion, and ΔT is the difference in temperatures of the top and bottom surfaces of the concrete nanocomposite.

Equation (1) provides an approximate estimation of the thermal stress magnitude under the assumption that the entire body is fully constrained and cannot expand. In such a case, the total strain ε_{total} equals zero, and thermal stress develops internally due to restrained expansion. The full expression from elasticity theory, $\sigma = E(\varepsilon_{total} -$ $\alpha . \Delta T$), simplifies to equation (1) when $\varepsilon_{total} = 0$. In this study, only the magnitude of the thermal stress is used in the calculations of the stress intensity factor and energy release rate, the sign is not considered. This assumption corresponds to an idealized boundary condition commonly adopted in fracture mechanics analyses of massive concrete or ceramic structures under thermal loading. Although such full restraint may not occur in real engineering conditions, it provides a conservative estimate of internal stress and is widely used for parametric evaluation in early-stage modelling [13-16].

Stress intensity factor and energy release rate

• SIF calculation. The mathematical model for calculating the stress near the crack tip (SIF) as a function of the orientation angle of the central crack θ can be described using equations from LEFM, [11-15].

For a rectangular plate with finite dimensions (length 2L and width 2W), containing a central crack of length 2a and orientation angle θ relative to the load, the stress intensity factor K_I is determined by:

$$K_I = \sigma_T \cdot \sqrt{\pi a} \cdot Y(a, \theta) \tag{2}$$

where a is half the length of the crack, and $Y(a, \theta)$ is a geometric correction function that accounts for both the relative crack size and its inclination. While this formulation is traditionally derived for mechanical tensile loading, it is applied here by substituting the magnitude of the thermally induced stress σ_T , to allow for parametric comparison of thermal fracture behaviour. The correction function is expressed as:

$$Y(a,\theta) = \frac{1}{\sqrt{\cos(\frac{\pi a}{2W})}} \cdot F(\theta)$$
 (3)

This form is constructed by analogy with classical Mode I SIF formulations for finite-width plates under mechanical loading. The term $\frac{1}{\sqrt{cos(\frac{\pi a}{2W})}}$

is used to approximate the effect of finite plate geometry, while the angular factor $cos^2\theta$ represents the reduction in the Mode I opening component as

the crack becomes more inclined. Although these terms are not derived from thermal fracture theory, they enable a simplified parametric evaluation of the trends in thermal fracture behavior under varying geometries. This heuristic approach offers practical insight, but it should not be interpreted as a rigorous solution based on thermomechanical coupling. The angular correction factor $F(\theta)$ is given by:

$$F(\theta) = \cos^2 \theta \tag{4}$$

This expression is based on the projection of normal stress components acting perpendicular to the crack plane, and it is consistent with tensor transformation results for inclined cracks.

This angular correction factor is introduced heuristically in the present study and appears here for the first time in this specific thermal fracture context.

Equations (3) and (4) are valid only within certain geometric limits: for small crack lengths relative to the plate width $a \ll W$, and moderate inclination angles $\theta < 75^{\circ}$. For $a \to W$ or $\theta \to 90^{\circ}$, the correction function becomes singular or unphysical. These cases are therefore excluded from the present analysis.

By combining equations (1), (3), and (4), the final expression for the stress intensity factor becomes:

$$K_I = \sigma_T . \sqrt{\pi a} . \frac{1}{\sqrt{\cos(\frac{\pi a}{2W})}} . \cos^2 \theta \tag{5}$$

This allows evaluation of how crack length, orientation, and thermal loading affect the intensity of the local stress field near the crack tip.

Although the expression originates from tensile loading conditions, its use here with thermal stress serves as an approximation to analyze relative trends in fracture behavior under idealized thermal conditions.

It should be noted that the expression in eq. (5) is not a direct result from classical thermal fracture theory. Rather, it is constructed by analogy with mechanical LEFM models, using heuristic correction factors to account for finite geometry and crack inclination. This formulation represents the author's contribution for enabling a simplified parametric analysis under thermal loading conditions.

As the crack length increases, the SIF K_I grows approximately with a, modulated by the geometric correction factor. Similarly, the crack orientation reduces the effective stress component through the $\cos^2\theta$ term.

The addition of nano-SiO₂ modifies both the elastic modulus E and the thermal expansion coefficient α , which directly affects the value of σ_T ,

and thus influences both the SIF K_I and the energy release rate G.

Although inclined cracks generally experience mixed-mode loading (Modes I and II), in this study only the Mode I SIF is considered for simplicity, based on the assumption that the dominant contribution to crack propagation arises from opening mode stresses due to constrained thermal expansion.

• *ERR calculation*. The energy release rate (ERR) is a key parameter in fracture mechanics, reflecting the energy available for crack propagation. It represents the rate at which elastic strain energy is released per unit crack extension and is particularly relevant for assessing the potential for thermally induced fracture in brittle materials such as concrete nanocomposites.

Once the stress intensity factor K_I has been calculated, ERR can be determined using:

$$G = \frac{K_L^2}{E} \tag{6}$$

This relation is derived under the assumption of Mode I crack propagation and plane stress conditions, which are appropriate for thin plates or surface cracks. It provides a scalar measure of the energy concentration at the crack tip.

In this study, the ERR is not interpreted as an absolute criterion for crack growth, but rather as a comparative parameter to evaluate the influence of different input variables (crack length, orientation, thermal load, and nano-SiO₂ content).

It should be noted that fracture toughness - i.e., the critical value of *G* required for crack propagation - is not experimentally measured here. Therefore, the ERR values are not used to directly predict failure, but to identify parametric trends and material configurations that reduce the energy available for crack advancement.

This approach aligns with the theoretical objective of the work and supports the preliminary assessment of thermally resistant nanocomposite design.

ANALYTICAL AND NUMERICAL SOLUTIONS

A hybrid analytical - numerical methodology was used to calculate the thermal stress, the stress intensity factor K_I , and the energy release rate G in a concrete nanocomposite with a centrally located inclined crack under thermal loading.

In this context, 'hybrid' refers to the combination of analytical fracture mechanics expressions with numerically computed temperature fields. The analytical expressions are used to calculate fracture parameters (thermal stress, K_I , and G), while the

numerical model is employed solely to evaluate the temperature distribution and validate the assumptions about local thermal loading.

Analytical expressions based on linear elastic fracture mechanics (LEFM) were implemented in Wolfram Mathematica using custom-developed macros. These allow for systematic and automated evaluation of fracture-related parameters across a wide range of input variables, including crack length α , orientation angles θ , thermal gradients ΔT , and material parameters E and α , corresponding to 1.0%, 1.5%, and 2.0% nano-SiO₂ content.

Thermal stress was calculated under the idealized assumption of fully restrained thermal expansion, leading to conservative estimates of internal stresses. This approximation allows for simplified trend analysis without solving a full thermal—mechanical coupling problem.

The resulting values of K_I and G were determined using the corrected geometric functions and were interpreted for comparative purposes.

In parallel, numerical simulations were carried out to visualize the applied temperature field and to examine the effects of crack geometry and thermal loading on the fracture parameters.

The results were presented using 2D and 3D parametric plots, which illustrate how ERR depends on crack geometry, temperature variation, and material stiffness. This method provides an efficient and accessible tool for preliminary thermal fracture assessment in nanocomposite materials, avoiding the complexity of full-scale finite element modelling.

Mechanical and thermal properties of the concrete composite

The mechanical and thermal properties of the concrete nanocomposites with different nano-SiO₂ contents used in the calculations and simulations, are summarized in Table 1. These values are based on experimentally validated literature data and are assumed constant throughout the simulations [1-6].

Table 1. Mechanical and thermal properties of the concrete nanocomposite

Type of concrete nanocomposite	Elastic modulus, E [GPa]	Coefficient of thermal expansion, $\alpha [1/K]$	
with 1% nano-SiO ₂	40	9.5×10^{-6}	
with 1.5% nano-SiO ₂	42	9.3×10^{-6}	
with 2% nano-SiO ₂	43	9.2×10^{-6}	

These input parameters directly affect the computed thermal stress and thus influence the stress intensity factor and energy release rate.

Assumed values for the temperature ΔT and geometry

The geometric configuration and thermal loading parameters used in the simulations are summarized in Table 2. The rectangular concrete nanocomposite plate is assumed to have a centrally located inclined crack, with variations in both crack geometry and thermal input. These parameters are applied consistently in the analytical model (for calculating thermal stress, K_I and G) and in the numerical simulations (for evaluating the thermal field and geometric effects).

Table 2. Geometric and thermal parameters used in the simulations

Thermal load, $\Delta T [K]$	20 ÷ 100
Plate length, 2L [m]	1
Plate width, 2W [m]	0.5
Initial crack length, $2a [m]$	$0.01 \div 0.1$
Orientation angle, θ [°]	0 ÷ 45

The thermal loading ΔT is interpreted in two distinct but consistent ways: In the analytical approach, ΔT is considered a local uniform temperature rise relative to a reference state (e.g., ambient temperature), corresponding to a fully constrained thermal expansion scenario. In the numerical model, it is treated as a vertical temperature gradient applied from the top to the bottom of the plate, representing practical thermal loading conditions in structural elements.

These ranges ensure that the analytical formulas remain within valid geometric bounds, avoiding singularities in the correction functions for large $\frac{a}{W}$ or extreme values of θ . The selected parameter space enables the observation of key trends in energy release rate and fracture sensitivity under varying thermal and geometric configurations.

The range of ΔT is selected to encompass typical and elevated service conditions for concrete structures, ensuring that the model captures conservative thermal stress effects.

Temperature distribution at different orientation angles. Calculation of thermal stress

Numerical macros were developed in Wolfram Mathematica to simulate the temperature distribution in a cracked concrete nanocomposite with different crack orientation angles θ . In parallel, analytical calculations of the thermal stress were carried out using equation (1) under the assumption of fully constrained thermal expansion.

In the numerical model, the geometry of the rectangular plate (length 2L and width 2W) and the central crack (length 2a and orientation angle θ) are first defined. Material properties for the different nanocomposites, including Young's modulus and thermal expansion coefficient, are taken from Table 1. The applied thermal load corresponds to a temperature difference $\Delta T = 100 \ K$, as specified in Table 2.

The boundary conditions for the thermal model are defined as follows: fixed temperatures are applied to the top and bottom surfaces using Dirichlet conditions: $T[x, -L] = T_{bottom} = 400 \text{ K}$ and $T[x, L] = T_{top} = 300 \text{ K}$. This imposes a vertical temperature gradient along the y-axis. The lateral boundaries $x = \pm W$ are thermally insulated, represented by natural Neumann conditions (zero heat flux): $\frac{\partial T(x,y)}{\partial y} = 0$, at $x = \pm W$. At the crack surfaces $(x = \pm a)$, an adiabatic condition is assumed, meaning that the heat flux across the crack faces is zero: $\frac{\partial T(x,y)}{\partial y} = 0$ at $x = \pm a$. The steadystate temperature field is obtained by solving the Laplace equation using the finite element method $\frac{\hat{\partial}^2 T(x,y)}{\partial x^2} + \frac{\partial^2 T(x,y)}{\partial y^2} = 0.$ The numerical (FEM): solution of the Laplace equation was performed in Wolfram Mathematica using its built-in finite element method (FEM) framework. The domain was discretized using an adaptive unstructured mesh of second-order triangular elements (ElementOrder → 2), which provide higher accuracy for smooth solutions such as temperature fields. The mesh was refined near the crack zone to better capture local temperature gradients. Dirichlet and Neumann boundary conditions were directly imposed using the DirichletCondition and NeumannValue functions. The software's built-in NDSolveValue was used to solve the steady-state heat conduction problem.

The simulations are performed for a fixed crack length of $2a = 0.1 \, m$ and $\Delta T = 100 \, K$, while the crack orientation angle is varied ($\theta = 0^{\circ}, 30^{\circ}, 45^{\circ}$). In contrast, the analytical thermal stress is computed from the simplified expression $\sigma_T = E.\alpha.\Delta T$, assuming uniform temperature rise at the crack location with respect to a reference temperature. This approach provides an upper-bound estimate of internal stress under fully restrained expansion.

As shown in Figure 2, when the crack orientation is horizontal ($\theta = 0^{\circ}$), the temperature distribution in the nanocomposite remains relatively uniform, indicating a more balanced heat transfer and a lower concentration of thermal stresses near the crack.

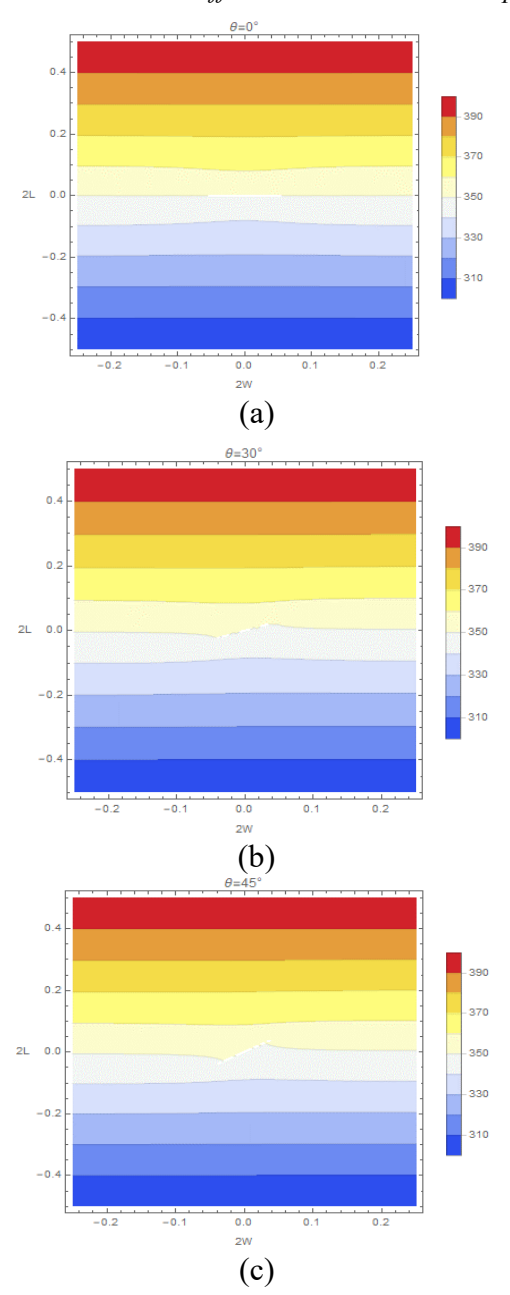


Figure 2. Temperature distribution in a concrete nanocomposite at different crack orientation angles: (a) $\theta = 0^{\circ}$; (b) $\theta = 30^{\circ}$; (c) $\theta = 45^{\circ}$

In contrast, for inclined cracks ($\theta > 30^{\circ}$), the temperature field becomes increasingly distorted in the vicinity of the crack. The inclination leads to asymmetric heat flow, which creates steeper local temperature gradients near the crack tips. These gradients are associated with higher thermal stresses due to restricted expansion in those regions. The numerical model presented here is used solely to compute the temperature field and to examine how crack orientation affects the local thermal distribution. It is not used to compute thermal stresses or fracture parameters. Instead, it serves as a visual justification for the use of a local ΔT assumption in the analytical solution near the crack

zone. It should be noted that the temperature value at the crack location (e.g., $\approx 350 \, K$ in Figure 2) reflects the mid-point of the linear temperature gradient between the top $(400 \, K)$ and bottom $(300 \, K)$ boundaries. This value is consistent with the global temperature difference $\Delta T = 100 \, K$ used in both the numerical and analytical models. In the analytical approach, ΔT is interpreted as a local uniform increase relative to a reference temperature, enabling estimation of thermal stress through equation (1).

The thermal stress σ_T increases linearly with temperature difference ΔT , according to eq. (1), and is used as input for subsequent SIF and ERR calculations. Adding a higher percentage of nano-SiO₂ to the concrete composite enhances its mechanical and thermal properties, including increased stiffness (elastic modulus) and improved thermal conductivity. However, this modification also intensifies the development of thermal stresses within the material. At elevated temperatures, the enhanced thermal conductivity leads to faster heat transfer, which steepens the internal temperature gradient. Under constrained conditions, this steeper gradient results in greater thermally induced stresses, especially near stress concentrators such as cracks.

Analytical and numerical solution for ERR

After obtaining the analytical solutions for the thermal stresses, macros were generated in the Wolfram Mathematica software to calculate both K_I and G for various crack configurations- specifically, different crack lengths a and orientation angles θ in a concrete nanocomposite with different percentages of nano-SiO₂.

Using the basic analytical equations, the fracture parameters were computed for each case. Additionally, 3D parametric plots were generated based on the analytical formula to study the dependence of ERR on crack length, orientation angle, K_I , elastic modulus E, and the thermal load ΔT . These simulations allowed for the systematic assessment of how changes in temperature gradient and material stiffness affect the energy release rate.

The results provide insight into the parametric influence of nano-SiO₂ content and thermal loading on thermal fracture behavior. Higher values of ΔT and crack inclination generally resulted in increased ERR, indicating greater risk of crack propagation under thermal stress.

• Analytical solution for ERR. Figure 3 illustrates the dependence of the energy release rate G on the stress intensity factor K_I for a concrete nanocomposite containing 1.0% nano-SiO₂. The values of K_I and G are calculated for a fixed

temperature difference $\Delta T = 50 \, K$, for various crack lengths $a = 0.005 \div 0.050 \, m$ and crack orientation angles $\theta = 0^{\circ}, 30^{\circ}, 45^{\circ}$.

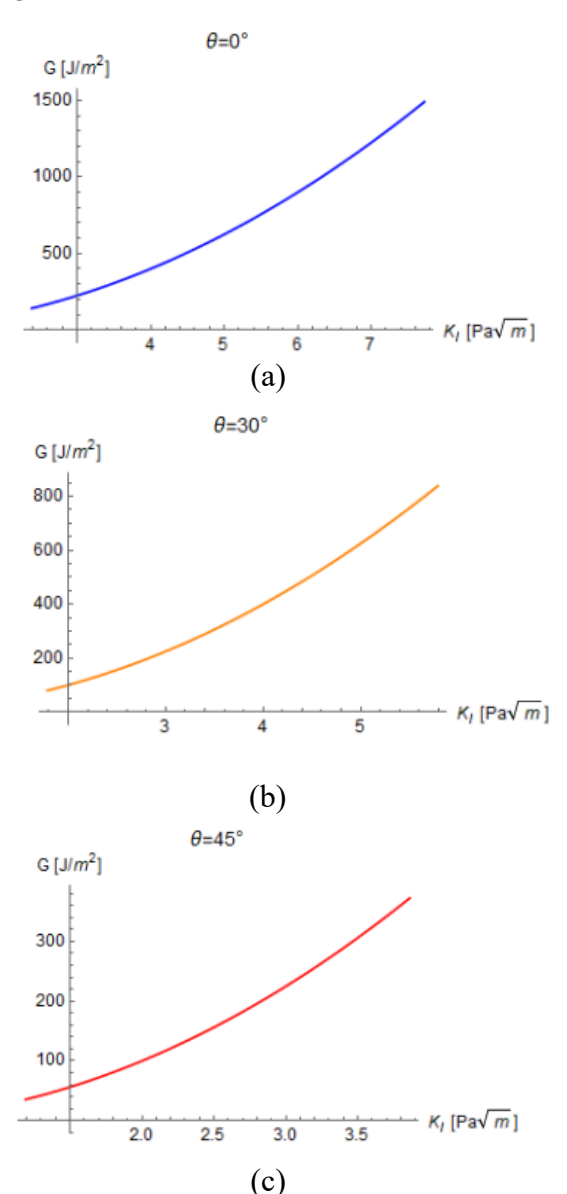


Figure 3. Dependence of the energy release rate G on the stress intensity factor K_I at different crack orientation angles: (a) $\theta = 0^{\circ}$; (b) $\theta = 30^{\circ}$; (c) $\theta = 45^{\circ}$

For a fixed crack orientation angle, both K_I and G increase with increasing crack length, following the square-root dependence on a and the geometric correction factors. Longer cracks concentrate higher thermal stresses at the crack tip, making them more susceptible to propagation under thermal loading. Conversely, for a fixed crack length, increasing the inclination angle θ leads to a noticeable decrease in both K_I and G. The lowest values are observed at $\theta = 45^\circ$, due to the reduced effective stress component acting normal to the crack plane. This behavior is consistent with fracture mechanics theory, where inclined cracks experience a reduced

driving force for Mode I opening under vertically directed thermal stress. This inverse relationship between crack angle and ERR highlights the importance of crack orientation in the design of thermally resistant nanocomposite structures.

• Numerical modelling of energy release rate at different crack angles and lengths. Figure 4 illustrates the variation of the energy release rate G for different crack orientation angles $\theta = (0^{\circ} \div 45^{\circ})$ and crack lengths $a = 0.005 \div 0.05m$, at a fixed temperature difference $\Delta T = 50 K$.

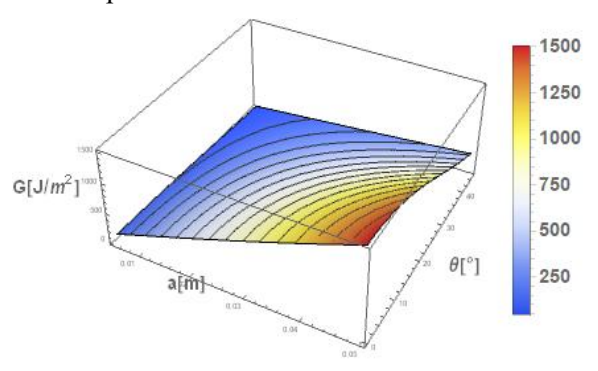


Figure 4. Dependence of *G* on crack orientation angle θ and crack length α at $\Delta T = 50$ K.

The results demonstrate that at a fixed crack angle θ , increasing the crack length a leads to a significant rise in G. Conversely, for a fixed crack length, increasing θ reduces the value of G, with minimum ERR observed at $\theta = 45^{\circ}$. This trend is consistent with the analytical form of the angular correction factor $F(\theta) = cos^2\theta$ which decreases with higher inclination angles, reducing the component of thermal stress acting normal to the crack.

These findings confirm that crack geometry - especially length and inclination - has a stronger effect on ERR than nano-SiO₂ content. Nevertheless, for composites with higher stiffness (e.g., 2.0% nano-SiO₂), ERR values remain higher due to increased thermal stress magnitudes under the same ΔT .

• 3D simulation of the dependence of ERR on SIF and the elastic modulus. With increasing nano-SiO₂ content (1.5% and 2%), the elastic modulus E of the concrete nanocomposite increases, resulting in higher thermal stresses under the same temperature gradient. Consequently, the stress intensity factor K_I and the energy release rate G also increase, as illustrated in Figure 5. However, the influence of crack orientation shows the opposite trend: for fixed crack length, increasing the inclination angle θ leads to a decrease in both K_I and G. This is due to the reduction in the normal component of thermal stress acting on the crack plane.

G. Nikolova: Thermal effects on concrete nanocomposites with central inclined cracks: Influence of crack geometry ...

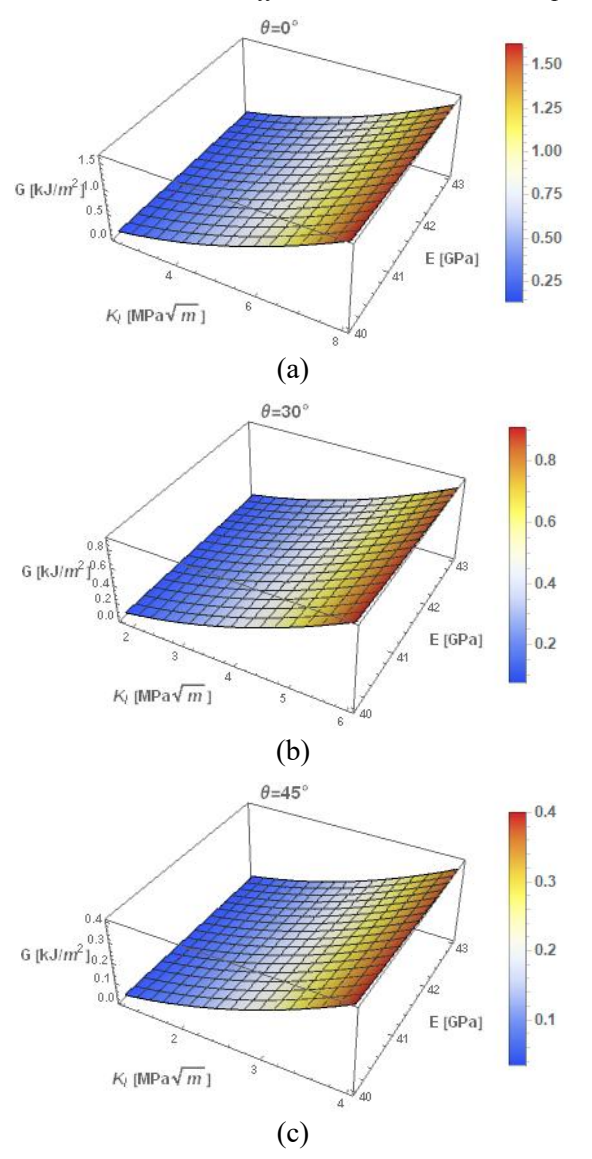


Figure 5. Dependence of *G* on K_I and *E* for $\Delta T = 50 K$.

Overall, higher nanoparticle content increases the material's stiffness and thermal stress, promoting crack propagation, while greater crack inclination angles tend to stabilize the crack by lowering the energy available for its growth.

• Numerical modelling of ERR at different ΔT . At temperature differences $\Delta T > 80 \, K$, the concrete nanocomposite with 2% nano-SiO₂ exhibits a pronounced increase in the energy release rate G, indicating a higher susceptibility to thermally induced crack propagation, Figure 6. This behavior reflects the increased stiffness of the material, which leads to higher thermal stresses under constrained conditions. In contrast, the composite with 1% nano-SiO₂ maintains the lowest values of G across the considered range of ΔT , suggesting improved resistance to thermal cracking.

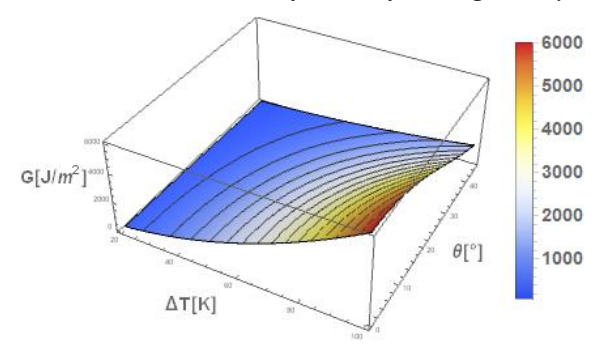


Figure 6. Dependence of G on ΔT and θ for a = 0.05 m

The influence of the crack inclination angle θ is also significant: for a fixed crack length, ERR values decrease with increasing angle, confirming the stabilizing effect of inclined cracks under thermal loading. The numerical results are in good agreement with the analytical model and support the conclusion that both thermal load intensity and crack geometry critically affect fracture behavior in nanomodified concrete.

INFERENCES FROM THE OBTAINED ANALYTICAL AND NUMERICAL RESULTS

Based on the conducted analytical and numerical study, the following conclusions can be drawn:

- The addition of nano-SiO₂ affects both the mechanical and thermal fracture behavior of concrete nanocomposites. At 1.0% content, the material demonstrates the lowest energy release rate values across a wide range of crack lengths and orientation angles, indicating improved thermal crack resistance.
- For fixed crack orientation angles, both the stress intensity factor K_I and the energy release rate G increase with crack length, and this growth is more pronounced at higher elastic moduli (i.e., higher nano-SiO₂ content). However, for fixed crack lengths, increasing the crack inclination angle leads to a significant reduction in both K_I and G, with the lowest values observed at $\theta = 45^\circ$, confirming the stabilizing effect of inclined cracks under thermal loading.
- Numerical simulations confirm the analytical predictions and provide detailed 2D and 3D visualizations of how ERR varies with crack length, angle, elastic modulus, and thermal load. The results highlight that crack geometry has a stronger influence on ERR than nanoparticle content under moderate thermal gradients.
- At elevated thermal loads ($\Delta T > 80 K$), concrete with 2.0% nano-SiO₂ shows a sharp rise in ERR, indicating increased brittleness and risk of thermal crack propagation despite its higher stiffness. This suggests a trade-off between stiffness

enhancement and fracture resistance at higher nanoparticle concentrations.

• For thermally and mechanically reliable design, it is crucial to optimize the nano-SiO₂ content. A 1.0% addition appears to provide a favorable compromise, especially for structures exposed to moderate thermal gradients and at risk of fracture initiation due to thermal loading.

It is important to note that the study is based on a simplified analytical model assuming fully constrained thermal expansion and using only the magnitude (not the sign) of thermal stress. No experimental fracture toughness measurements were conducted. The conclusions are therefore applicable to preliminary design and parametric assessment purposes and should be validated with further experimental data.

CONCLUSION

In this study, a mathematical model based on elastic fracture mechanics (LEFM) was developed to determine the energy release rate (ERR) in a concrete nanocomposite containing different percentages of nano-SiO₂ (1%, 1.5%, and 2%) under monotonic thermal loading. The analysis focused on evaluating the influence of crack length and orientation angle on thermally induced damage processes in concrete.

Thermal stress was estimated using a simplified analytical expression, assuming fully restrained thermal expansion and considering only the magnitude of the stress, without accounting for its sign. While this approach does not yield exact stress distributions, it provides a practical approximation suitable for comparative parametric analysis of ERR and SIF values.

Numerical simulations carried out in Wolfram Mathematica enabled the evaluation of ERR across a wide range of temperature differences and crack configurations. The results demonstrate that ERR increases with thermal load and crack length, but decreases with increasing crack inclination angle, especially beyond 30°. Among the studied compositions, concrete with 1.0% nano-SiO₂ exhibited the most favorable behavior, with the lowest ERR across most conditions. In contrast, higher nanoparticle contents (1.5% and 2%) were associated with higher ERR at large crack lengths, particularly under high temperature gradients, due to the increased elastic modulus and resulting thermal stresses.

The developed model provides a useful framework for the preliminary evaluation and design of thermally resistant concrete nanocomposites. However, it should be noted that the analysis does

not include experimental determination of fracture toughness, and the results are valid within the limitations of the adopted assumptions. Future work will focus on validating the proposed analytical model through comparison with experimental data and high-fidelity numerical simulations using commercial FEM software, to further assess the model's predictive capability.

REFERENCES

- M. Alvansazyazdi, F. Alvarez-Rea, J. Pinto-Montoya, M. Khorami, P. Bonilla-Valladares, A. Debut, M. Feizbahr, Sustainability, 15(21), 1 (2023).
- 2. M. Lezgy-Nazargah, S. Emamian, E. Aghasizadeh et al., *Sādhanā*, **43**, 196 (2018).
- 3. H. Hamadi, R. Atea, S. Badr, *International Journal of Applied Sciences and Technology*, **4(3)**, 234 (2022).
- 4. S. Aleem, M. Heikal, W. Morsi, *Construction and Building Materials*, **59**, 151 (2014).
- 5. G. Vasanth, K. Ramadevi, *International Journal of Advanced Research in Science, Communication and Technology*, 50 (2022).
- D. Syamsunur, L. Wei, Z. Memon, S. Surol, N. Yusoff, *Materials*, 15(20), 7073 (2022).
- 7. P. Brzozowski, J. Strzałkowski, P. Rychtowski, R. Wróbel, B. Tryba, E. Horszczaruk, *Materials*, **15(1)**, 166 (2022).
- 8. F. Sanchez, K. Sobolev, *Construction and Building Materials*, **24** (11), 2060 (2010).
- 9. A. Kizilkanat, N. Yüzer, N. Kabay, *Construction and Building Materials*, **45**, 157 (2013).
- 10. Q. Ma, R. Guo, Z. Zhao, Z. Lin, K. He, *Construction and Building Materials*, **93**, 371 (2015).
- 11. G. Irwin, *Journal of Applied Mechanics*, **24(3)**, 361 (1957).
- 12. T. Anderson, Fracture Mechanics: Fundamentals and Applications, 4th edn., CRC Press, 2017.
- 13. Z. Bazant, J. Planas, Fracture and Size Effect in Concrete and Other Quasibrittle Materials, 1st edn., Routledge, (1998).
- 14. P. Paris, F. Erdogan, *Journal of Basic Engineering*, **85(4)**, 528 (1963).
- 15. M. Williams, *Journal of Applied Mechanics*, **24(1)**, 10 (1957).
- H. Tada, P. Paris, G. Irwin, The Stress Analysis of Cracks Handbook, 3rd edn., ASME Press, 2000, p. 698.
- 17. G. Sih, Mechanics of Fracture, 1. Noordhoff International Publisher, Leyden, (1973).
- 18. A. Yanakieva, G. Nikolova, *Journal of Theoretical and Applied Mechanics*, **50**, 389 (2020).
- 19. A. Yanakieva, *International Journal of Mechanical and Production Engineering (IJMPE)*, **3(11)**, 47 (2015).
- 20. T. Petrova, *Bulgarian Chemical Communications*, **55(3)**, 349 (2023).

Analytical and numerical study of thermal stresses and stress intensity factors in a concrete nanocomposite with nano-SiO₂ under monotonically increasing temperature

G. N. Nikolova*

Institute of Mechanics, Bulgarian Academy of Sciences, Sofia, Bulgaria

Received: May 03, 2025, Revised: May 27, 2025

The analytical and numerical modelling of the behavior of a concrete nanocomposite under monotonically increasing temperature is presented. The research methodology includes analytical modelling based on linear elastic fracture mechanics (LEFM) to determine the thermal stresses and stress intensity factors (SIF) in a concrete nanocomposite with a symmetrically located central crack, considering the influence of both crack length and the temperature. The numerical solutions are obtained by using the specialized software product Wolfram Mathematica, including the generation of special macros to automate the calculations of the thermal stresses and temperature distribution in uncracked and cracked concrete composites, with or without the addition of nanoparticles. The obtained results show that for small cracks, the difference between the SIF values of the two materials (concrete composite without/with 2% nano-SiO₂) is minimal, while for larger cracks the SIF value of the nanocomposite is significantly higher, but not too large, which preserves the relative stability of the material. For example, at a crack length of 0.01 m, the SIF increases from 25.39 MPa·m¹/² (without nanoparticles) to 27.55 MPa·m¹/² (with nano-SiO₂), illustrating enhanced crack resistance. At the same time, total thermal stresses increase with temperature, reaching values of up to 12.8 MPa in nano-SiO₂ concrete compared to 10.9 MPa in standard concrete at $\Delta T = 100$ °C. The developed mathematical models provide a convenient tool for thermal and fracture analysis, which can be applied in the design of sustainable, durable, and thermally resistant concrete structures.

Keywords: Concrete nanocomposite, nano-SiO₂, central crack, SIF, analytical and numerical results, thermal stresses

INTRODUCTION

Motivation and significance of the study

Concrete is a basic construction material, but its resistance to thermal loads is limited due to its low tensile strength and its tendency to crack at high temperatures [1-3]. The addition of nano-SiO₂ significantly improves the mechanical and thermal properties of concrete by reducing porosity and increasing its thermal stability. Analytical modelling based on linear elastic fracture mechanics (LEFM) and numerical solutions obtained using the finite difference method (FDM) and finite element method (FEM) in Wolfram Mathematica software will be useful for more accurate determination of local and total thermal stresses and SIF values in a concrete nanocomposite with a central crack.

Literature review

Concrete nanocomposites are an innovative class of energy-efficient materials that are gaining increasing popularity in the construction industry due to their exceptional properties and environmental benefits. They combine traditional concrete with nanoparticles, leading to improved mechanical and thermal properties [4]. Nano-SiO₂ is one of the most nano-additives effective that: change microstructure of concrete – it reduces porosity and improves bonding between cement paste and aggregates; accelerates cement hydration - leads to faster hardening and increased strength; increases concrete resistance to cracking - increases tensile strength and compressive strength; improves thermal resistance - reduces thermal expansion and increases resistance to temperature loads [5, 6]. The greater strength of concrete with nano-SiO2 allows for the construction of thinner and lighter structures, which reduces the use of raw materials and leads to lower energy consumption during construction. Concrete nanocomposites with nano-SiO₂ are key materials for sustainable construction, as on the one hand they help reduce the carbon footprint and energy consumption, and on the other hand they increase the durability of buildings and structures [7-11].

During the operation of concrete structures, they are often subjected to temperature effects that can induce thermal stresses and accelerate the development of cracks in them. Understanding the influence of temperature, mechanical and thermomechanical loads on stresses and strains, stress

^{*} To whom all correspondence should be sent: E-mail: gery@imbm.bas.bg

intensity factors (SIF) and energy release rate (ERR) are essential for assessing the durability and reliability of concrete and other types of nanocomposites [12-23]. The classic work [13] investigates the stress concentration around crack tips using fracture mechanics methods such as stress intensity factor, energy approaches and fracture models to predict the resistance of materials to cracking. The works [14] and [15] analyze the stress distribution at the base of a fixed crack using different theoretical models for stress concentration estimation, critically reviewing existing crack propagation laws, and comparing different criteria for crack growth and resistance. The work [16] presents various analytical and numerical methods for studying crack problems, focusing on fracture mechanics, stresses around cracks and criteria for their propagation. The book [17] is related to fracture mechanics and describes the main guidelines for the analysis of stress concentration in cracks and their propagation. In [18] and [19], detailed formulas and examples for calculating SIF and the influence of various stresses, including temperature stresses, on cracks in materials are proposed. The book [19] also discusses the basic principles of fracture mechanics. In several publications, research has focused on estimating SIF and the rate of energy release for various composite materials, but there is a lack of sufficient data on the behavior of concrete nanocomposites with nano-SiO2 under temperature effects, [2, 3, 12, 20], etc.

The aim of this study is to supplement the available literature in this area by developing a complex analytical model that covers:

- Calculation of thermal stresses in a concrete composite with/without added 2% of nano-SiO₂ at monotonically increasing temperature.
- Determination of stress intensity factors at different lengths of the initial crack and at different temperature values.
- Analysis of the influence of added nanoparticles in concrete on the values of thermal stress and SIF.

PROBLEM FORMULATION

The concrete nanocomposite is modelled as a rectangular plate with width 2W, length 2L and a central symmetric crack with length 2a, Figure 1. The plate is subjected to a monotonically increasing temperature with a temperature difference $\Delta T = T_{high} - T_{low}$, where T_{high} and T_{low} are the temperatures of the upper and lower boundaries of the plate, respectively. The direction of the temperature gradient is also shown, namely from the upper to the lower surface. The center of the coordinate system

Oxy, used in the model, is in the middle of the crack. The x-axis is oriented horizontally (along the thickness of the plate) and is symmetric with respect to the crack, i.e., $x \in (-W, W)$. This axis measures the distances to the left and right of the center of the crack. The y-axis is oriented vertically (along the length of the plate) and is centered so that its positive part reaches the upper boundary, and the negative part reaches the lower boundary of the plate, i.e., $y \in (-L, L)$.

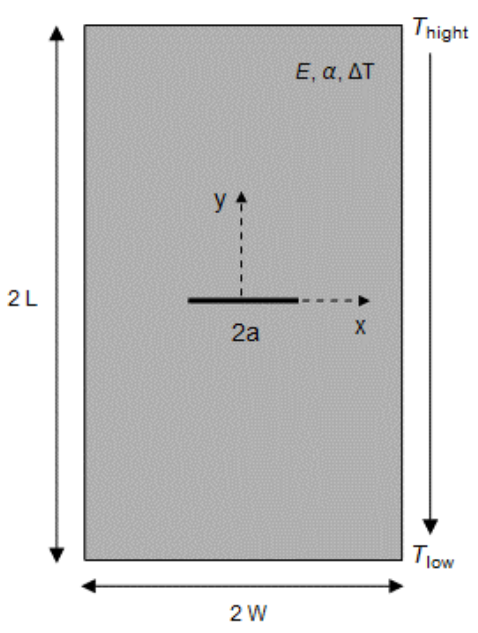


Figure 1. Geometric model of a concrete nanocomposite with a central crack under temperature monotonic loading ΔT

The choice of such a symmetric coordinate system facilitates analytical and numerical analysis and allows the application of simpler models and a clear understanding of the effects of the crack on the temperature distribution and the associated thermal stresses.

BASIC EQUATIONS AND ASSUMPTIONS

Thermal stress

Under monotonically increasing temperature, thermal stress is induced in the material and is determined by the following formula:

$$\sigma_T = E. \alpha . \Delta T \tag{1}$$

where E is the modulus of elasticity, α is the coefficient of linear thermal expansion, and ΔT is the total temperature difference from the upper to the lower boundary of the concrete nanocomposite.

Equation (1) is based on the general principles of thermal expansion theory [13-16] and provides an "average" or global value for the thermal stress that would develop if the entire concrete nanocomposite were subjected to a constant change in temperature ΔT .

The local thermal stress is determined using the temperature gradient (usually in the *y* direction, if the temperature field varies mainly in that direction) and is calculated by the formula:

$$\sigma_T(x,y) = E.\alpha.\frac{\partial T(x,y)}{\partial y}$$
 (2)

This stress depends on the position of (x, y) in the model and reflects the local rate of temperature change.

Stress intensity factor (SIF)

When analyzing SIF in a rectangular plate with finite dimensions (length 2L and width 2W) and with the presence of a central crack of length 2a, the general formula for calculating SIF is:

$$K_I = \sigma_T \cdot \sqrt{\pi a} \cdot f(a, W) \tag{3}$$

where σ_T are the thermal stresses, a is the crack radius (or half the crack length in the case of a central crack), W is half the plate width, and f(a, W) is a dimensionless correction function depending on the plate dimensions and the crack length.

For small crack lengths relative to the plate width $(\frac{a}{W} \ll 1)$, the correction function f(a, W) can be approximated by a Taylor series expansion of the function [18]:

$$f(a, W) \approx 1 + \frac{1}{2} \left(\frac{\pi a}{W}\right)^2 \tag{4}$$

For values of the ratio $\frac{a}{w} \le 0.01$, we get for the correction function that $f(a, W) \approx 1$, which on the one hand means that the geometric effect is negligible, but on the other hand will help to simplify the calculations. If $\frac{a}{W} \to \frac{1}{2}$ (the crack is almost half the width of the plate), then $f(a, W) \to \infty$, equation (5). When the ratio $\frac{a}{W}$ increases and becomes larger than 0.01, expression (4) becomes less accurate and a more precise correction function must be used [20], and the formula should be used:

$$f(a, W) = 1/\cos\left(\frac{\pi a}{W}\right) \tag{5}$$

Equations (2) and (3) are based on the classical linear elastic fracture mechanics (LEFM) theory developed in [17, 18]. When varying different crack lengths a, the value of K_I will vary linearly with $\sqrt{\pi a}$, which means that longer cracks will also lead to higher stress values. The addition of different nanoparticles to the concrete will change the values of E and α , which will also have an impact on the thermal stresses and ultimately on the value of K_I .

Basic assumptions

- *Homogeneity and isotropy*: The material is assumed to be homogeneous and isotropic.
- *Linear elasticity*: The material behavior remains within the linear elastic region.
- One-dimensional temperature change: The temperature change (temperature difference) ΔT is assumed to vary in one direction only (monotonically).
- Geometric simplicity: Cracks are modelled with simplified geometric parameters (length).
- Effect of nanoparticles: The inclusion of 2% of nano-SiO₂ in the concrete modifies the basic material parameters E and α .

ANALYTICAL AND NUMERICAL SOLUTIONS

Analytical modeling based on linear elastic fracture mechanics (LEFM) was performed and included the generation of special macros in the Wolfram Mathematica software for automation of calculations of thermal stresses and SIF in a concrete composite with or without added 2% of nano-SiO₂. The influence of temperature ΔT and crack length on SIF values was analyzed. A comparative analysis of the obtained results for SIF in a concrete composite with and without added 2% of nano-SiO₂ was also performed. Numerical simulations of thermal stresses and temperature distribution in uncracked and cracked concrete composite with or without added nanoparticles in it are also presented.

Mechanical and thermal characteristics of the concrete composite

The data in Table 1 for the mechanical and thermal characteristics of the concrete composites used for the calculations and simulations are taken from experimental studies published in works [5, 6, 9].

Table 1. Mechanical and thermal characteristics of concrete composites

Type of concrete composite	Elastic modulus, E [GPa]	Coefficient of thermal expansion, $\alpha [1/K]$
Without nanoparticles	28.149	10×10^{-6}
With nano- SiO ₂	30.655	9.8×10^{-6}

Assumed values of the temperature ΔT and geometry of the concrete composite structural element

The geometry of the rectangular plate (of concrete composites) with a central crack at varying values of the temperature ΔT is presented in Table 2.

Table 2. Assumed values of the temperature ΔT and geometry

Thermal load, $\Delta T [K]$	20 ÷ 200
Plate length, 2L [m]	1
Plate width, 2W [m]	0.5
Initial crack length, $2a [m]$	$0.001 \div 0.1$

Temperature distribution in a plate with and without a central crack

- Calculation of local and total thermal stress: Macros for numerical modelling using the finite difference method (FDM) and finite element method (FEM) of the temperature distribution in a concrete nanocomposite with and without a central crack, and macros for calculating the total thermal stress (equation (1)) and 2D visualization of the local thermal stress (equation (2)), were generated in the Wolfram Mathematica program. The macros include:
- Defining the parameters and region of the crack: First, the values of the main material parameters are defined and set, followed by those for the geometry of the plate and the crack, as shown in Table 2.
- Boundary conditions: The boundary conditions are set with fixed temperatures at the upper and lower boundaries T_{hight} and T_{low} using Dirichlet conditions: $T[x, -L] = T_{low} = 300 \ [K]$ and $T[x, L] = T_{hight} = 400 \ [K]$ and with isolated lateral boundaries (natural Neumann conditions), i.e., $\frac{\partial T(x,y)}{\partial y} = 0$ at $x = \pm W$. The boundary conditions for an isolated crack (with no heat exchange between its walls) are also set using the Dirichlet conditions, i.e., $\frac{\partial T(x,y)}{\partial y} = 0$ at $x = \pm a$. This means that the heat flux through the crack boundaries is zero (insulated walls).
- Finite element method: For numerical modelling, the command "NDSolveValue" is used with the option "Method" and type "FiniteElement", i.e., the finite element method is applied to solve the Laplace equation. The command "ContourPlot" is used to numerically model the temperature distribution for the two cases concrete nanocomposite without and with the presence of a

central crack with length 2a = 0.2[m], see Figure 2. It demonstrates that in an uncracked concrete composite, the temperature is distributed evenly, which means that there is a lower concentration of thermal stresses. When the composite material is cracked, heat transfer is disrupted and high temperature gradients appear around the edges of the crack, which leads to an increase in local thermal stresses.

• Calculation and visualization of thermal stresses: The total thermal stress is calculated by formula (1), and the local thermal stress is determined using the temperature gradient expressed by formula (2) for different $\Delta T = (20 \div 200) [K]$, Figure 3. The difference in the values of thermal stresses in a cracked concrete composite with and without added 2% of nano-SiO2 is minimal at low temperature differences as $\Delta T < 70$ [K], while at higher ones this difference increases significantly, as shown in Figure 3. The 2D graphs were generated for the local thermal stresses at $\Delta T = 100 [K]$ for both cases – concrete nanocomposite without and with the presence of a central crack with length 2a = 0.2[m], Figure 4. It clearly shows that the addition of nano-SiO2 to the concrete nanocomposite improves its mechanical and thermal properties, but also leads to an increase in thermal stresses in the material. This means that with temperature change, heat spreads faster, which increases the temperature gradient in the material and leads to higher local values of thermal stresses.

Calculation of SIF at different lengths of the central crack at a fixed value of the temperature difference

Special program codes were generated in the Wolfram Mathematica program to automate SIF calculations and to quickly assess the influence of the addition of nano-SiO₂ in the concrete composite (by changing the values of E and α) and the crack length on the values of the stress intensity factor at $\Delta T = 50 \ [K]$. The results are presented in Table 3. It shows that in the presence of temperature change, concrete composites with 2% of nano-SiO₂ added exhibit higher SIF values compared to ordinary concrete. This phenomenon is observed both at higher and lower temperature differences ΔT , but the effect may manifest itself differently depending on the intensity of the temperature gradient.

$G.\ N.\ Nikolova:$ Study of thermal stresses and stress intensity factors in a concrete nanocomposite with nano-SiO₂ ...

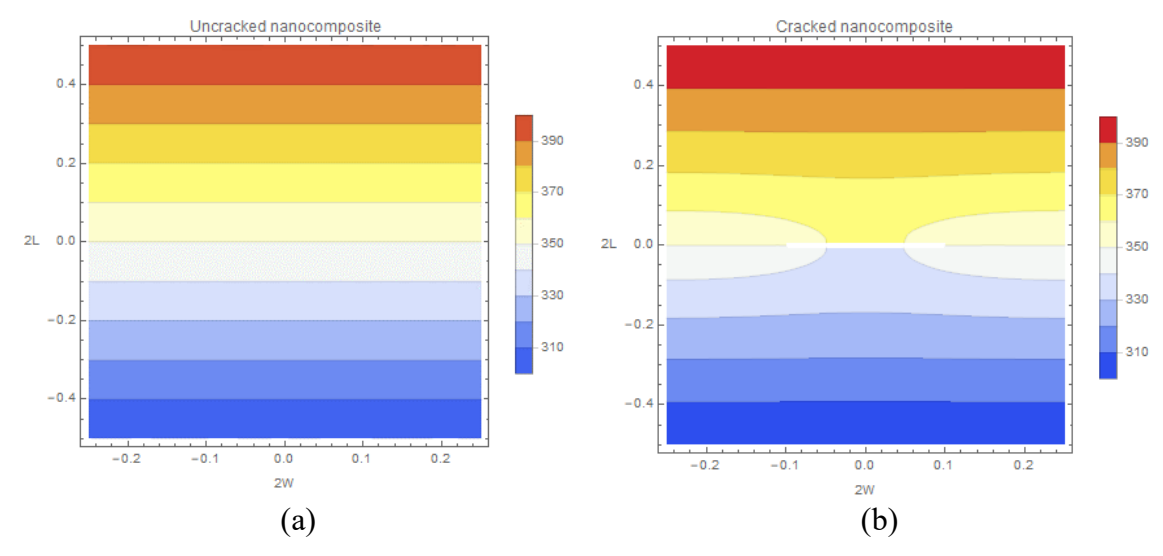


Figure 2. Temperature distribution in (a) Uncracked and (b) Cracked concrete nanocomposite at a fixed value of $\Delta T = 100 \, [K]$.

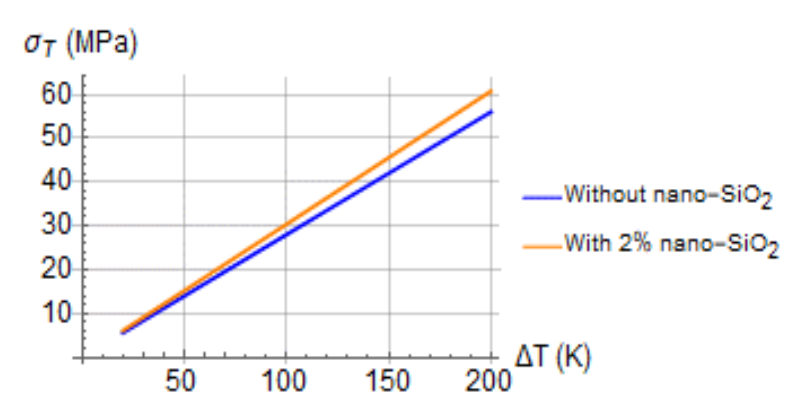


Figure 3. Dependence of the thermal stress on the temperature difference ΔT for cracked concrete composite with / without added 2% of nano-SiO₂.

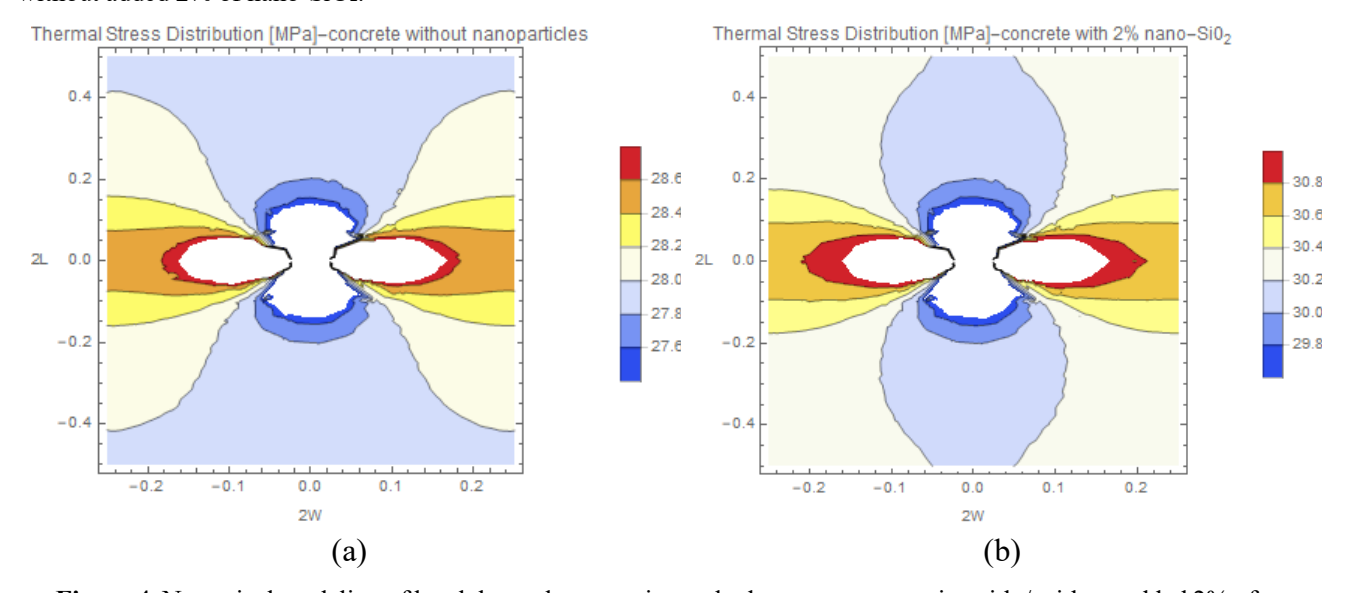


Figure 4. Numerical modeling of local thermal stresses in cracked concrete composite with / without added 2% of nano-SiO₂ at $\Delta T = 100 \ [K]$

Table 3. SIF calculations

	$K_{I}\left[MPa.m^{1/2}\right]$			
a [m]	Concrete without	Concrete with 2%		
	nanoparticles	of nano-SiO2		
0.0005	0.555	0.602		
0.001	0.785	0.851		
0.0015	0.961	1.043		
0.002	1.110	1.204		
0.0025	1.241	1.347		
0.003	1.360	1.476		
0.0035	1.469	1.594		
0.004	1.571	1.705		
0.0045	1.667	1.809		
0.005	1.758	1.908		
0.01	2.501	2.714		
0.05	6.859	7.441		
0.10	25.393	27.552		

As ΔT increases, the temperature gradient in the material becomes steeper, which leads to larger local thermal stresses around the crack tip.

INFERENCES FROM THE OBTAINED ANALYTICAL AND NUMERICAL RESULTS

The following conclusions were drawn:

- In uncracked concrete composite, the temperature is distributed evenly, and the concentration of thermal stresses is small. In a composite with a central crack, heat transfer disturbances occur, and high temperature gradients appear around the edges of the crack, which leads to an increase in local thermal stresses.
- Numerical analyses using the FEM confirm the analytical calculations by providing a better understanding of the distribution of thermal stresses in the area around the crack.
- The addition of nano-SiO₂ significantly improves the strength and durability of concrete, but also increases thermal stresses, especially under conditions of rapid temperature change. This means that when designing structures with nano-modified concrete, the increased sensitivity to thermally induced cracking must be considered, and appropriate measures for thermal compensation and temperature gradient control must be implemented.
- The high modulus of elasticity of nano-SiO₂ concrete means that it exhibits greater resistance to deformation, which further increases SIF values. As a result, K_I at high ΔT is larger for nanocomposite concrete compared to ordinary concrete, meaning that cracks are more likely to expand under high temperature loads.

- Adding nano-SiO₂ increases the strength of the concrete, allowing it to withstand higher stresses before cracking. A higher K_I value does not mean that the material is more easily damaged, but that it can accumulate more stress before reaching its critical failure value.
- Concrete with 2% of nano-SiO₂ accumulates higher thermal stresses, which increases the SIF value. However, it has significantly higher compressive strength and elastic modulus, which means that it can withstand higher loads before failure. It is stronger, more resistant to thermal expansion and mechanical stress, making it a better choice for long-lasting and thermally resistant structures.

CONCLUSION

In this study, an analytical and numerical approach is presented to determine the thermal stresses and stress intensity factors (SIFs) in a concrete nanocomposite with a central crack subjected to monotonically increasing temperature. By combining thermal and mechanical models, the influence of both crack length and addition of 2% nano-SiO2 on the temperature distribution, thermal stress development, and fracture behavior of concrete composites is evaluated. The results show that in uncracked concrete, the temperature distribution remains relatively uniform, resulting in lower thermal stress concentration. In contrast, the presence of a crack leads to localized temperature gradients and higher thermal stresses near the crack tip. Numerical modelling confirms that concrete composite with 2% of nano-SiO₂ accumulates higher thermal stresses due to its higher stiffness—reaching up to 12.8 MPa compared to 10.9 MPa in standard concrete at $\Delta T = 100$ °C. Similarly, SIF values are slightly higher in the nano-SiO2 composite: for a crack length of 0.01 m, the SIF increases from 25.39 MPa·m^{1/2} (without nanoparticles) to 27.55 MPa·m^{1/2} (with nanoparticles). Although higher SIF values indicate increased stress intensity at the crack tip, the improved strength and elasticity of nanocomposite ensure that it can sustain greater thermal and mechanical loads before failure.

The developed Mathematica-based macros allow for efficient simulation and analysis, contributing to the practical design of advanced, thermally resilient construction materials. Concrete nanocomposites with nano-SiO₂ are thus a promising solution for durable and energy-efficient structural applications.

REFERENCES

- 1. P. Mehta, P. Monteiro, Concrete: Microstructure, Properties, and Materials, 4th edn. New York: McGraw-Hill Education, 2014.
- 2. A. Kizilkanat, N. Yüzer, N. Kabay, *Construction and Building Materials*, **45**, 157 (2013).
- 3. Q. Ma, R. Guo, Z. Zhao, Z. Lin, K. He, *Construction and Building Materials*, **93**, 371 (2015).
- 4. F. Sanchez, K. Sobolev, *Construction and Building Materials*, **24** (11), 2060 (2010).
- M. Alvansazyazdi, F. Alvarez-Rea, J. Pinto-Montoya, M. Khorami, P. Bonilla-Valladares, A. Debut, M. Feizbahr, Sustainability, 15(21), 1 (2023).
- H. Wang, H. Mang, Y. Yuan, B, Materials, 12(17), 2689 (2019).
- 7. M. Lezgy-Nazargah, S. Emamian, E. Aghasizadeh et al., *Sādhanā*, **43**, 196 (2018).
- 8. H. Hamadi, R. Atea, S. Badr, *International Journal of Applied Sciences and Technology*, **4(3)**, 234 (2022).
- 9. S. Aleem, M. Heikal, W. Morsi, *Construction and Building Materials*, **59**, 151 (2014).
- D. Hein, S. Sullivan, in: Conference and Exhibition of the Transportation Association of Canada -Transportation: Innovations and Opportunities, Budapest, Fredericton New Brunswick, Canada, 2012, p. 13.
- 11. G. Vasanth, K. Ramadevi, *International Journal of Advanced Research in Science, Communication and Technology*, **2(1)**, 50 (2022).

- 12. D. Syamsunur, L. Wei, Z. Memon, S. Surol, N. Yusoff, *Materials*, **15(20)**, 7073 (2022).
- 13. G. Irwin, *Journal of Applied Mechanics*, **24(3)**, 361 (1957).
- 14. M. Williams, *Journal of Applied Mechanics*, **24(1)**, 10 (1957).
- P. Paris, F. Erdogan, *Journal of Basic Engineering*, 85(4), 528 (1963).
- 16. G. Sih, Mechanics of fracture I, Noordhoff International Publisher, Leyden, 1973.
- Z. Bazant, J. Planas, Fracture and Size Effect in Concrete and Other Quasibrittle Materials, 1st edn., Routledge, 1998.
- 18. H. Tada, P. Paris, G. Irwin, The Stress Analysis of Cracks Handbook, 3rd edn., Publisher: ASME Press, 2000, p. 698.
- 19. T. Anderson, Fracture Mechanics: Fundamentals and Applications, 4th edn., CRC Press, 2017.
- 20. P. Brzozowski, J. Strzałkowski, P. Rychtowski, R. Wróbel, B. Tryba, E. Horszczaruk, *Materials*, **15(1)**, 166 (2022).
- 21. A. Yanakieva, G. Nikolova, *Journal of Theoretical and Applied Mechanics*, **50**, 389 (2020).
- A. Yanakieva, International Journal of Mechanical and Production Engineering (IJMPE), 3(11), 47 (2015).
- 23. T. Petrova, *Bulgarian Chemical Communications*, **55(3)**, 349 (2023).

Microbial and catalytic degradation of synthetic dyes

N. Shukova^{1*}, N. Armenova¹, D. Uzun², A. Gigova², O. Dimitrov², M. Dimtrova², L. Ljutzkanov¹, E. Razkazova-Velkova¹

¹Institute of Chemical Engineering, Bulgarian Academy of Sciences, Acad. G. Bonchev Str., Bl.103, Sofia 1113, Bulgaria

2Institute of Electrochemistry and Energy Systems "Acad. Evgeni Budevski", Bulgarian Academy of Sciences, Acad. G. Bonchev Str., Bl.10, Sofia 1113, Bulgaria

Received: May 01, 2025; Accepted: June 05, 2025

The present work is dedicated to microbial and catalytic degradation of synthetic dyes. Methylene blue, congo red, methyl orange are used as model solution of dyes. A test for cytotoxicity is conducted using two bacterial strains *Pseudomonas putida 1046* and *Bradyrhizobium japonicum 273*. These bacterial strains show tolerance to the dyes up to concentrations of 250 mg/l. It is proved that *Bradyrhizobium japonicum 273* does not decolor the dyes, except for congo red. *Pseudomonas putida 1046* decolors methylene blue and congo red with concentration of 250 mg/l for 42 h up to 96% and 92%, respectively. A screening for an appropriate catalyst for dyes degradation is conducted among ZnO, TiO₂, ZrO₂ incorporated on a matrix of activated carbon and sole activated carbon. TiO₂ proved to be suitable for the process. Experiments with TiO₂ under different conditions are carried on. *Pseudomonas putida 1046* shows tolerance in the presence of TiO₂, so experiments for simultaneous microbial and catalytic degradation of methylene blue are conducted.

Keywords: Degradation of dyes, *Pseudomonas putida 1046, Bradyrhizobium japonicum 273,* ZnO-, TiO₂-, ZrO₂-catalysts.

INTRODUCTION

In recent decades, the pollution of water bodies by huge volumes of untreated industrial wastewater (e.g. paper, cosmetics, textiles, plastics, etc.) contaminated with organic dyes, is considered an ecological crisis with a dangerous impact. Wastewaters polluted with dyes are a major restriction for the sustainable development of many industries [1].

Azo dyes make up approximately 60 % of the total dye production per year [2]. They are a class of synthetic chemical compounds characterized by their azo group (-N = N-) and complex aromatic structures [3]. These groups impart vivid colors to the dyes that create strong desires for a number of industrial applications. Azo dyes present high chemical stability and persistence, increasing the challenges to their degradation. The azo dyes are characterized and compared based on their molecular structure and weight, water solubility, acid dissociation constant, n-octanol-water partition coefficient, and maximum absorbance. Congo red (CR) is a diazo dye [4]. Methylene blue (MB) is one of the most common cationic phenothiazine dyes. Methyl orange (MO) is an anionic azo dye, most commonly used for dyeing cotton, wood, and silk. Organic dyes MB and MO have poor biodegradability, meaning that they can remain in

natural water bodies for a long time [5-8].

The methods used for dye removal include chemical, physical and biological processes [9, 10]. Chemical treatments involve oxidation, reduction, and neutralization processes, while physical methods include adsorption, coagulation, and membrane filtration. Biological treatment, involving a combination of microorganisms that break down pollutants, offers a more sustainable and environmentally friendly alternative. Various physicochemical methods are used for treatment of textile wastewaters, but they generate large amounts of toxic sludges which require additional treatment and costs. Heterogeneous photocatalysis offers significant advantages over other methods, mainly low energy consumption, easy operation, no secondary pollution, and moderate reaction conditions. Therefore, the textile industry needs a wastewater treatment technology that removes toxic sludge, requires less energy and remains safe for the environment.

Various adsorbent materials have been tested for the effective removal of methylene blue (MB) including spent olive stones [11] and raw dolomite [12]. Activated lignin-chitosan extruded (ALiCE) pellets offer great potential for removing cationic organic pollutants from rivers and streams [13].

Heterogeneous photocatalysis, using metal oxide semiconductors as photocatalysts, offers a promising

^{*} To whom all correspondence should be sent: E-mail: nastemil@abv.bg

alternative for degrading toxic organic pollutants into harmless inorganic molecules. Metal oxide semiconductors such as TiO₂ [14], ZnO [15, 16], NiO [17, 18], CuO [19], MnO_x [20, 21] and Cr₂O₃ [22] are used as catalysts. They are promising materials due to their electronic structure, light absorption properties, and charge transport characteristics [23]. They have outstanding physical, chemical, and optical properties. They are costeffective and non-toxic catalysts that allow complete mineralization. The (Mn, Ni) co-doped ZnO catalyst is prepared using Stephania abyssinica leaf extract [16] and is used for degradation of MB dye under visible light. TiO₂-g-C₃N₄ heterojunction is employed as a photocatalyst for the sunlight-assisted photodegradation of CR dye [18]. Nickel-doped zinc oxide (Ni_{0.05}Zn_{0.95}O) nanoparticles are tested as a potential adsorbent and catalyst for the removal of specific dves, MO and tartrazine, from an aqueous solution [24]. Co₃O₄ nanocube-doped polyaniline nanocomposites have been successfully synthesized as an oxidant in acidic medium for efficient removal of MO from aqueous solution [25].

Different strains are reported to degrade azo dyes [26]. In [27] *Pseudomonas mt2* degrades MO dye. *Bradyrhizobium japonicum* and *Pseudomonas putida* are reported [28, 29] to degrade phenol and cathehin that are intermediate products of dye mineralization.

Many papers are dedicated to the decolorization of azo dyes in fuel cells [30, 31]. The microbial fuel cells (MFCs) combine physiochemical and

biological principles to convert chemical waste into electric energy and detoxify pollutants. Waste pomelo peel is used as the main raw material for preparation of iron-nitrogen-carbon nanocomposite as cathode catalyst for the degradation of CR in a fuel cell [30].

The aim of the present work is to study the catalytic and microbial degradation of MO, MB and CR. MO and CR are chosen as models of anionic azo dyes and MB as a cationic one. These are preliminary investigations in order to choose an appropriate catalyst and strain for further development of a fuel cell for dyes decontamination.

MATERIALS AND METHODS

The biomass concentrations read as optical densities (OD) and dye concentrations are determined spectrophotometrically on a VWR UV–1600 PC spectrophotometer at a wavelength of 600 nm for the biomass, 664 nm for MB, 498 nm for CR and 465 nm for MO. The rate of the decolorization is calculated by the following equation:

% decolorization =
$$\frac{A_0 - A_{\text{sample}}}{A_0} \times 100$$
, where

 A_{o} – absorption of the beginning solution; A_{sample} – absorption of the tested sample.

The experiments are conducted with dyes (Merck KGaA) dissolved in a phosphate buffer solution. Summarized information of the dyes is given in Table 1.

Table 1. Information about the investigated dyes

Name of the azo dye	Chemical formula	Molecule structure	Characteristic
Methylene blue (MB)	C ₁₆ H ₁₈ ClN ₃ S	S N N CI	Cationic azo dye
Methyl orange (MO)	C ₁₄ H ₁₄ N ₃ NaO ₃ S	N = N = N	Monoazo anionic acid dye
Congo red (CR)		NH ₂ NH ₂ N=N N=N N=N N=N N=N	Diazo anionic direct dye

Catalysts preparation

All catalysts are incorporated on a matrix of activated carbon. Their preparation method is a patented technology that includes impregnation of organic material with the corresponding precursor salt and subsequent pyrolysis with simultaneous activation [32]. ZnO, TiO2, ZrO2 incorporated on a matrix of activated carbon and sole activated carbon are used in this investigation. The organic material for the preparation of the catalysts are sunflower husks. The catalyst showing the best performance (namely TiO₂) is characterized by SEM, EDS, XRD, surface area by BET and iodine adsorption. BET studies are carried out employing a Quantachrome instrument Autosorb iQ (USA) that measures the quantity of gas adsorbed on or desorbed from a solid surface at an equilibrium vapor pressure by a static volumetric method. The investigations are carried out on NOVAtouch-Quantachrome instrument apparatus (USA) that measures adsorbed and desorbed volumes of gas at relatively low pressure (lower than 1). The obtained data after computer processing are presented as isotherms of adsorption and/or desorption from which are calculated specific surface area, pore volume, pore size and pore size distribution of the powder samples. X-ray diffraction (XRD) patterns are recorded utilizing a diffractometer using CuKa radiation $(\lambda=1.54178 \text{ Å}, 40 \text{ kV} \text{ and } 30 \text{ mA})$ with a scanning rate of 2° min⁻¹. The surface morphology of the samples is investigated by scanning electron microscopy (SEM) using a Zeiss Evo 10 microscope (Carl Zeiss Microscopy, Oberkochen, Germany). The images are taken in secondary electrons mode with accelerating voltage of 25 keV, and no additional conductive coating on the surface. The chemical composition of the samples is studied using the Oxford Ultim Max 40 electron dispersive spectroscopy (EDS) probe (Oxford Instruments, Abingdon, UK). The results are compiled with AZtec software (version 6.1 HF4).

Catalytic decolorization

The conditions for the catalytical decolorization are 200 ml dye solution and 0.1 g catalyst. Screening for the most appropriate catalyst is conducted. Different conditions are investigated as rpm, dark and light mode, etc.

Microbial strain and cultivation conditions

The bacterial strains *Pseudomonas putida* (NBIMCC 1046) and *Bradyrhizobium japonicum* 273, used for the decolorization assays, are obtained

from the Bulgarian National Bank for Industrial Microorganisms and Cell Cultures. The bacterial strains are maintained as a frozen liquid culture supplemented with 1:1 glycerol at -20 °C

The strain *P. putida* is cultured in 500 ml flasks with 100 ml of medium containing: peptone – 10 g/l, meat extract – 10 g/l, NaCl – 5 g/l. The inoculum for the experiments is developed up to $OD_{600} = 2$ at 30 °C per shaker and 100 rpm.

B. japonicum is cultured in 500 ml flasks with 100 ml. of YMA (yeast mannitol agar) medium containing - K₂HPO₄ - 0.2 g/l, MgSO₄ - 0.2 g/l, mannitol - 10 g/l, yeast extract - 0.3 g/l, NaCl -20 g/l for 7 days at 28 °C.

For the investigation for tolerance of the strains to different dye concentrations, the cultivation is conducted by adding 20 g/l agar to the abovementioned cultivation media.

Azo dyes with different concentrations (100 mg/l - 250 mg/l) are dissolved in phosphate buffer and sterilized trough 0.45 µm filter. The tolerance of the bacteria to azo dye is studied by the "hole method" in a Petri dish [33]. A sterilized cork borer is used to create the wells (8 mm in diameter). The azo dye solutions (80 µl) with different concentrations (100 mg/l - 250 mg/l) are introduced in the lateral 4 holes. Holes in the center of the agar plate filled with sterile phosphate buffer solution (80 µl) are used as control. Petri dishes are incubated in a thermostat for 24 h (P. putida) at +30 °C / or 7 days (B. japonicum) at +28°C. The inhibition diameter is measured and the minimum inhibitory concentration is determined. The experiments for dye decolorization are carried out with 10% (v/v) inoculation of the bacterial stains in 500 ml flasks with 200 ml of dye solution and the components of the respective cultivation media on a rotary shaker at 30 °C and a stirring speed of 100 rpm. Periodically samples for decolorization of the dyes are centrifuged (10 000 rpm, 5 min) and the absorbance of the supernatants is measured at 664 nm for MB, 498 nm for CR, 465 nm for MO.

Experiments for the tolerance of P. putida to the TiO_2 catalyst are performed using two parallel cultivations with and without catalyst. No inhibition of the growth in the presence of TiO_2 is observed. The quantity of the catalyst is the same as for the experiments for the catalytic decolorization.

RESULTS AND DISCUSION

The results for decolorization using different dyes and catalysts are summarized in Table 2. The experiments are carried out with dye concentration of 120 mg/l for 5 days without stirring at a temperature of 25 °C. It can be seen that TiO₂ and

ZnO have the best performance. In Table 3 a comparison of TiO₂ and ZnO for decolorization of MB at 25 °C for 4 days is given. The results are for dyes dissolved in buffer and in distilled water under stirring with different speeds and without stirring. The results show a slight dependence of the decolorization rate on the rotation speed and the solvent used.

Table 2. Comparison of different catalyst

Dye Catalyst, surface area, m²/g*	MO, % of decolorization	MB, % of decolorization
ZnO, 645	96.5	98.82
TiO ₂ , 798.	98	99.95
ZrO ₂ , 503	50	43
Activated carbon (AC), 310	43	39

^{*}Surface area by iodine adsorption

Table 3. Comparison of TiO_2 and ZnO catalysts at different conditions

	Decolorization of dye dissolved in water, %		Decolorization of dye dissolved in phosphate buffer, %			
	Without 100 150 stirring rpm rpm		Without stirring	100 rpm	150 rpm	
TiO ₂	94.40	98.2	99.96	97.85	95.1	99.6
ZnO	91.35	92.2	98,4	99.4	93.1	99.5

Fig. 1 represents the decolorization rate using TiO_2 and ZnO in light and dark mode. The initial concentration of the dyes is 100 mg/l. The solution is prepared in phosphate buffer. As it can be expected, the decolorization is slower at dark mode.

Once again, the performance characteristic of TiO₂ exceed those of ZnO.

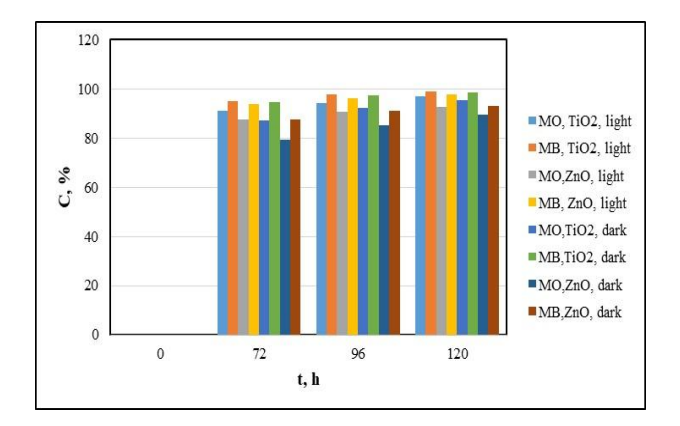


Fig. 1. Comparison of the decolorization of dyes with different catalysts and conditions

 TiO_2 was chosen for further investigations. The SEM images of TiO_2 on sunflower husks are shown in Fig. 2.

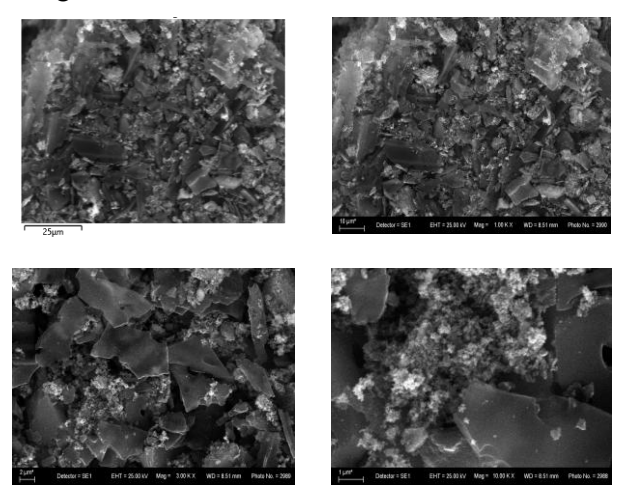
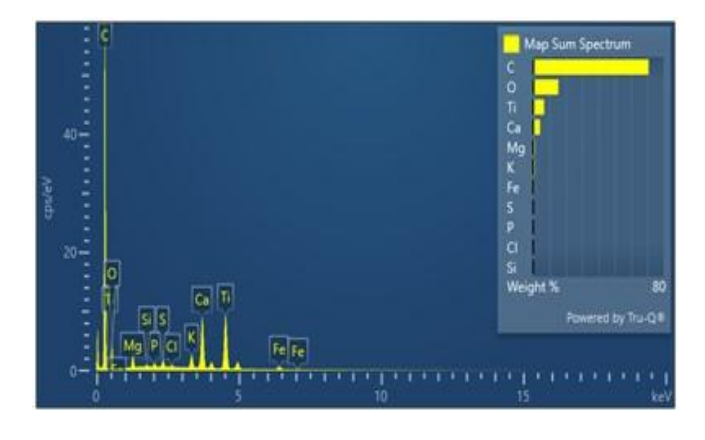


Fig. 2. SEM images of TiO₂ on sunflower husks

The EDS results are shown in Fig. 3 and summarized in Table 4.



To Go C Decton

Fig. 3. EDS of the TiO_2 on sunflower husks.

Table 4. Results	of the EI	S of the	TiO2 on	sunflower husks
I abic T. ICoulto	or the Li	or or and	1107011	Summo wer musiks

Map Sum Spectrum						
Element	Signal Type	Line	Wt%	Wt% Sigma	Atomic %	
С	EDS	K series	70.77	0.13	81.97	
О	EDS	K series	15.36	0.13	13.36	
Mg	EDS	K series	0.96	0.01	0.55	
Si	EDS	K series	0.09	0.01	0.04	
P	EDS	K series	0.18	0.01	0.08	
S	EDS	K series	0.35	0.01	0.15	
Cl	EDS	K series	0.11	0.01	0.04	
K	EDS	K series	0.89	0.01	0.31	
Ca	EDS	K series	4.06	0.02	1.41	
Ti	EDS	K series	6.57	0.03	1.91	
Fe	EDS	K series	0.66	0.01	0.16	
Total			100.00		100.00	

The surface morphology of the catalytic powder and its chemical composition are characterized by SEM and EDS techniques (Figs. 2, 3). The SEM images reveal that the morphology of the powder consists of two distinctive components - larger flat substrates with smaller clustered particles on top and between them. The large plate-like structures with irregular shapes and sizes between 5-20 µm form the base the catalytic powder. of The measurements clearly show that they are made of carbon and a closer look at higher magnifications reveals that they serve as a substrate for the nanocomponent of the catalyst. According to the elemental analysis, the small uniform particles (20-30 nm) that can be found clustered in the gaps of the carbon plate structures are primarily made of titanium and oxygen. This is in agreement with the XRD analysis that showed the presence of a tetragonal TiO2 phase. The observed surface morphology of nano sized particles on substrates with large surface area facilitates good catalytic properties of the synthesized material. The other element that can be seen from the elemental maps occupying the same volume as titanium in the powder is calcium. According to the XRD it forms the second distinctive phase in the catalyst, rhombohedral full chemical CaCO₃. The composition of the powder is calculated from the EDS results and can be viewed in Table 4. As expected, the strongest signal is attributed to carbon which comes from the sunflower husks. Oxygen accounts for about 13 at. %, followed by Ti and Ca with 1.9 and 1.4 at. %, respectively. All other elements are registered in very small amounts in the powder (under 0.5 at. % each) and can be attributed

to precursor impurities and sunflower husk inclusions.

A PANalytical Aeris diffractometer with CuK α radiation (40 kV, 15 mA), wavelength λ =1.5406 Å and θ - θ Bragg-Brentano geometry is used to determine the phase composition. The diffractogram is taken at room temperature, constant scan rate and reflection angle 2 θ in the range 10÷70° with a step of 0.02°, 60 s. The resulting XRD pattern is interpreted using the PDF 2-2022 database, ICDD. The presented diffractogram reveals the phase composition of the TiO₂ catalyst (Fig. 4).

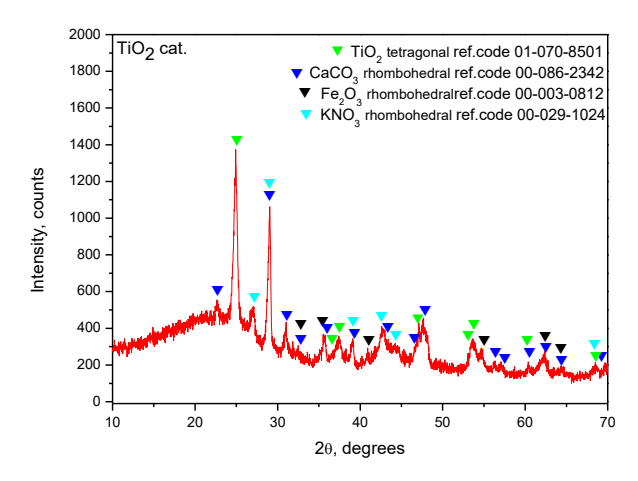


Fig. 4. XRD of TiO₂ on sunflower husks

The synthesized material exhibits low crystallinity, with the presence of an amorphous halo likely attributed to the use of an activated carbon carrier (derived from sunflower husks). The most intense peak, recorded at $2\theta = 24.76^{\circ}$, along with additional peaks at 37.38° , 46.89° and 53.13° , is associated with the (101), (004), (200), and (105) crystallographic planes of the tetragonal TiO_2

structure. The peak at $2\theta = 29.02^{\circ}$, attributed to the primary (104) reflection of the rhombohedral CaCO₃ phase, together with smaller peaks at 22.63°, 30.99°, 36.06° and 39.33°—linked to the (102), (006), (110), and (113) planes, respectively – confirm its significant presence in the catalyst. Additionally, the emergence of lower-intensity peaks at $2\theta = 54.58^{\circ}$ and 27.02°, corresponding to the (122) and (012) orientations of the rhombohedral Fe₂O₃ and KNO₃ phases, respectively, suggests that these two phases are present in smaller amounts within the TiO₂ catalyst.

The adsorption and desorption isotherms of TiO₂ catalyst are measured by physisorption of nitrogen gas. The isotherms are presented in Fig. 5.

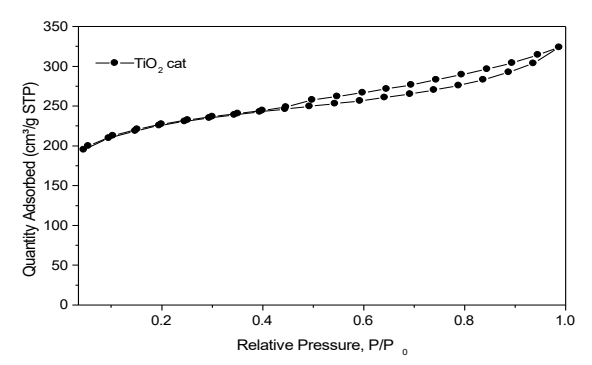


Fig. 5. Nitrogen adsorption/desorption isotherms on TiO₂ catalyst

The measured sorption isotherm approaches Type I (b) according to the IUPAC classification, with H4 type hysteresis. Reversible isotherms of this Type are given by microporous solids. For nitrogen adsorption at 77 K, Type I (b) isotherms are found with materials having pore size distributions over a broader range including wider micropores and possibly narrow mesopores ($< \sim 2.5$ nm). The H4type hysteresis loop is often found in micromesoporous carbons [34]. The structural characteristics are determined from the adsorption isotherm and are summarized in Table 5.

Table 5. Surface characteristics of TiO₂

Characteristics	TiO ₂ catalyst		
Surface area (BET), m ² /g	722		
Pore volume, cm ³ /g	0.502 for pores smaller than 150 nm (D)		
Average pore diameter, (4V/S), nm	2.8		
*Pore diameter (BJH desorption), nm	3.8		

^{*}The pore diameter is reported from the desorption isotherm.

The surface area is determined by the BET (Brunauer, Emmett, Teller) method. Multipoint BET is defined at relative pressure in the range of $p/p_0 =$ 0.1 - 0.3. The pore volume is measured at a relative pressure close to 1 (p/p₀ = 0.99). Average pore diameter is calculated, assuming that the pores have a cylindrical geometry at $p/p_0 = 0.99$. The measured structural characteristics of the TiO2 catalyst studied show a large specific surface area and a developed pore volume for pores with a diameter below 150 nm. The average pore diameter is 2.8 nm, close to the diameter of the most common pores with a size of 3.8 nm (see Fig. 6). Pore size distribution is the distribution of pore volume with respect to pore size. In this case, the pore diameter distribution is calculated from the desorption branch of the isotherm using the Barrett, Joyner, Halenda method (BJH method, Desorption). The differential pore diameter distribution curve for TiO2 catalyst is given in Fig. 6. The peak is at a pore diameter of 3.8 nm.

Fig. 7 shows the tolerance of both strains to the maximal concentration of the dyes. Up to the studied concentrations, no inhibition zone is detected.

Fig. 8 shows the decolorization of MB and CR for 42 h with *P. putida*. The initial concentration is 250 mg/l. The decolorization rate at 42 h is 92 % for CR and 96 % for MB. *B. japonicum* doesn't degrade MB and MO. It degrades CR to 95 % for 72 h.

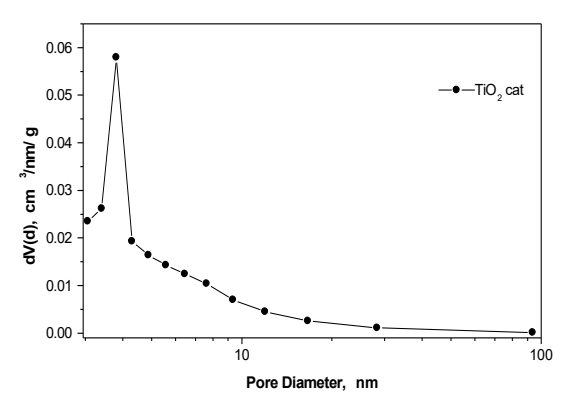


Fig. 6. Differential pore diameter distribution curve of TiO₂ catalyst

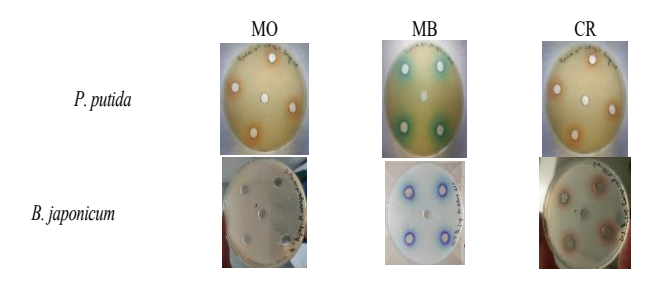


Fig. 7. Tolerance of the bacterial strains to 250 mg/l of the dyes

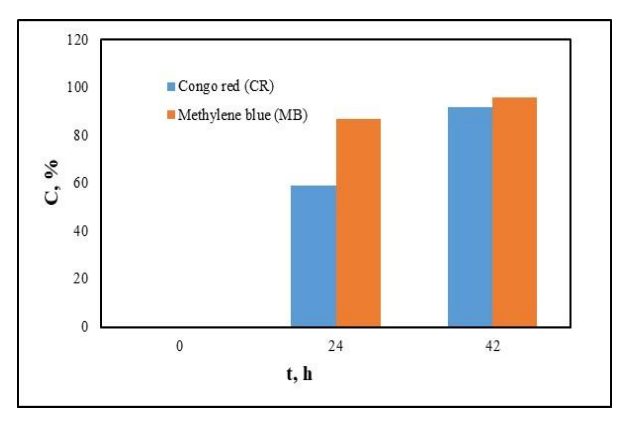


Fig. 8. Decolorization of dyes with *Pseudomonas* putida 1046

Fig. 9 shows a comparison of the decolorization rate of MB by the use of catalyst and combination of P. putida and catalyst at two different dye concentrations (100 mg/l and 50 mg/l). The combination of a catalytic and a bacterial process gives about two times faster decolorization for the 24th hour for both concentrations as compared with the pure catalyst. For the 48th hour the rate is also two times higher for the higher concentration. The decolorization rate at the 72nd hour is 93 % for the lower concentration and 94 % for the higher in the presence of bacteria and only 68 % for the higher concentration with catalyst. Further investigations are going to be carried out with different concentrations of dye in order to estimate the synergetic effect of catalyst and bacteria and the concentration that can be decolorized by the bacteria.

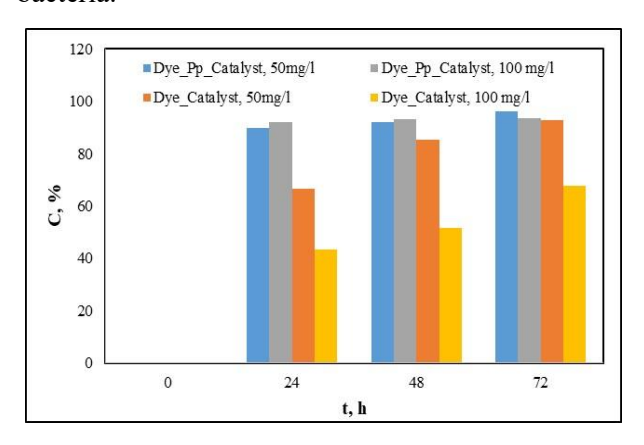


Fig. 9. Comparison of the decolorization of MB at different conditions with *P. putida 1046* (Pp).

CONCLUSIONS

It is found that the dyes are not toxic to *Pseudomonas putida 1046* and *Bradyrhizobium Japonicum 273 up to a* concentration of 250 mg/l. *Bradyrhizobium Japonicum 273* does not degrade the studied dyes, except CR. *Pseudomonas putida*

1046 can decolorize 250 mg/l of MB and CR for 42 h. up to 92 % and 96 % respectively.

The comparison of ZnO and TiO₂ as catalysts for dye degradation shows the advantage of TiO₂ as a catalyst. TiO₂ is not toxic to *Pseudomonas putida* 1046. The decolorization of MB in the presence of TiO₂ and *Pseudomonas putida* 1046 is 90 % for 24 h while using only the catalyst it is 40-60 % for the same time.

Acknowledgement: This research was funded by the Bulgarian National Science Fund, grant number KP-06-N67/6 from 12 December 2022.

- 1. W.S. Wan Ngah, L.C. Teong, M.A.K.M. Hanafiah, *Carbohydr. Polym.*, **83**, 1446 (2011).
- H. D. Bouras, A. R. Yeddou, N. Bouras, D. Hellel, M. D. Holtz, N. Sabaou, A. Chergui, Nadjemi, *J. Taiwan Inst. Chem. Eng.*, 80, 915 (2017) DOI: 10.1016/j.jtice.2017.08.002.
- M. Sharma, S. Sharma, A. Ahmed, M. Alkhanjaf, N. K. Arora, B. Saxena, A. Umar, A. A. Ibrahim, M. S. Akhtar, A. Mahajan, S. Negi, R. Kumar, S. Baskoutas, J. of Ind. and Eng. Chem. 142 45, (2025).
- 4. A. Strebell, M. Behringer, H. Hilbig, A. Machner, B. Helmreich, *Frontiers in Environ. Eng.*, DOI 10.3389/fenve.2024.1347981 1, (2024).
- A. Asfaram, M. Ghaedi, S. Hajati, A. Goudarzi, RSC Adv. 5, 72300 (2015).
- 6. Y. Liu, Z. Chen, C.-H. Shek, C.M.L. Wu, J.K.L. Lai, *ACS Appl. Mater. Interfaces*, **6**, 9776 (2014).
- 7. H. Zou, Y. Wang, Environ. Sci. Pollut. Res., 26, 23061 (2019).
- 8. Y. Yang, W. Yu, S. He, S. Yu, Y. Chen, L. Lu, Z. Shu, H. Cui, Y. Zhang, H. Jin, *App. Clay Sci.*, **168**, 304 (2019).
- 9. Y. Yang, D. Jin, G. Wang, D. Liu, X. Jia, Y. Zhao, *Colloid Surf.*, *B*, **88**, **521** (2011).
- 10. S. Natarajan, H.C. Bajaj, R.J. Tayade, *J. Environ. Sci.*, **65**, 201 (2018), https://doi.org/10.1016/j.jes.2017.03.011.
- A.B. Albadarin, C. Mangwandi, J. Environ. Manage., 164, 86 (2015).
- 12. A.B. Albadarin, J. Mo, Y. Glocheux, S. Allen, G. Walker, C. Mangwandi, *Chem. Eng. J.*, **255**, 525 (2014).
- 13. A. B. Albadarina, M. N. Collinsc, M. Naushad, S. Shirazian, G. Walker, C. Mangwandi, *Chem. Eng. J.*, **307**, 264 (2017).
- F. Di Fonzo, C.S. Casari, V. Russo, M.F. Brunella, A.L. Bassi, C.E. Bottani, *Nanotechnology*, 20, (2008).
- A. Di Mauro, M.E. Fragala, V. Privitera, G. Impellizzeri, *Mater. Sci. Semicond. Process*, 69, 44 (2017).
- 16. H. H. Haitosa, B. B. Tesfamariam, N. S. Gultom, Dong-Hau Kuo, X. Chen, Yi-nan Wu, O. A. Zelekew, *J. of Mol. Liquids*, **368**, 120666 (2022).

- 17. A. Diallo, K. Kaviyarasu, S. Ndiaye, B. Mothudi, A. Ishaq, V. Rajendran, M. Maaza, *Green Chem. Lett. Rev.*, 11, 166 (2018).
- 18. M. Saeed, H. Asghar, I. Khan, N. Akram, M. Usman, *Catalysis Today*, **447**, 115 (2025).
- P. Raizada, A. Sudhaik, S. Patial, V. Hasija, A.A.P. Khan, P. Singh, S. Gautam, M. Kaur, V.-H. Nguyen, Arab. J. Chem., 13, 8424 (2020).
- 20. R. Yang, Y. Fan, R. Ye, Y. Tang, X. Cao, Z. Yin, Z. Zeng, *Adv. Mater.*, **33** (9), e2004862 (2021).
- J. Y. Zheng, J. He, C. B. Han, G. Huang, B. C. Sun, W. K. Zhao, Y. Wang, L. Sun, J. Si, H. Yan, *Int. J. Biol. Macromol.*, 237, 124 (2023).
- 22. J. Su, H. Xue, M. Gu, H. Xia, F. Pan, *Ceram. Int.*, **40**, 15051 (2014).
- 23. M.M. Khan, S.F. Adil, A. Al-Mayouf, *Elsevier*, 462 (2015).
- 24. C. Klett, A. Barry, I. Balti, P. Lelli, F. Schoenstein, N. Jouini, *J. of Environ. Chem. Eng.*, **2** (2), 914 (2014).
- 25. S. Shahabuddin, N. M. Sarih, S. Mohamad, S. N. A. Baharin, *RSC Adv.*, **49**, 1 (2016).

- G. McMullan, C. Meehan, A. Conneely, N. Kirby, T. Robinson, P. Nigam, I. M. Banat, R. Marchant, W. F. Smyth, *Appl. Microbiol Biotechnol.*, 56, 81 (2001) DOI 10.1007/s002530000587.
- 27. T. P. Thao, Hsiang-Chien Kao, Ruey-Shin Juang, J. Chi-Wei Lan, J. of the Taiwan Inst. of Chem. Eng., 44, 780 (2013).
- 28. E. Vasileva, Ts. Parvanova-Mancheva, V. Beschkov, *J. of Int. Scientific Publications*, **14**, 165 (2020).
- 29. W. Hopper, A. Mahadevan, *Biodegradation*, 159 (1997) DOI: 10.1023/A: 1008254812074.
- 30. S. Zhang, Sh. Zhang, H. Liu, L. Li, R. Guo, J. of Environ. Chem. Eng., 11, 109264 (2023)
- 31. A. Yadav, P. Kumar, D. Rawat, Sh. Garg, P. Mukherjee, F. Farooqi, A. Roy, *Sci. of the Total Environ.*, **826**, 154038 (2022).
- 32. L. Ljutzkanov, A. Atanasov, BG patent № 63594 /26.06.2002.
- 33. N. Vorobey, K. Kukol, P. Pukhtaievych, S. Kots, *J. Central Europe. Agricul.*, **22 (4)**, 735 (2021), https://doi.org/10.5513/JCEA01/22.4.3157.
- 34. M. Thommes, K. Kaneko, A. V. Neimark, J. P. ver, F. R. Reinoso, J. Rouquerol, S. W. S. Kenneth, *Pure and Appl. Chem.*, 1051 (2015) https://doi.org/10.1515/pac-2014-1117.

Synthesis and properties of Cu - doped finely dispersed ceramic pigments

F. S. Yovkova¹, M. G. Minova¹, A. A. Georgieva^{1*}, I. G. Markovska¹

¹Burgas State University "Prof. Dr. Assen Zlatarov", Department of Chemical Technology, 1, Prof. Yakimov Blvd., 8000 Burgas, Bulgaria

Received: May 03 2025; Revised: July 10, 2025

The present work investigates the synthesis and properties of finely dispersed ceramic pigments from the Al_2O_3 - SiO_2 system. The synthesis of the pigments was carried out by the solid-phase sintering method. As initial materials both pure materials and waste raw materials - waste rice husks were used. In the first case, Al_2O_3 and $SiO_2.nH_2O$ were used as a pure initial material. The more active amorphous form of $SiO_2.nH_2O$ was chosen, instead of the crystalline form of silica. Rice husk is a waste product containing about 20 % SiO_2 . By burning rice husk in an oxidizing environment, the amount of SiO_2 significantly increases. For the purposes of the experiment, rice husk ash (RHA) with a 94.47 % SiO_2 content, was used. The synthesis was carried out at temperatures of 1350 °C and 1400 °C with a one-hour isothermal period. In both starting compositions - from pure and waste raw materials, the amount of Cu chromophore was 5% introduced in the form of CuO. Finely dispersed gray pigments were obtained. The pigments synthesized from the Al_2O_3 - SiO_2 system were investigated by a number of methods - X-ray diffraction, scanning electron microscopy, hot-stage microscopy, thermogravimetric analysis, color measurement, etc. The results of the scanning microscopy showed that clusters of particles are formed. The color of the pigments was determined spectrally on a Lovibond Tintometer RT 100 Color. The pigments with the best color characteristics were those obtained from pure raw materials (Al_2O_3 and $SiO_2.nH_2O$) at 1400 °C for 1 hour - (a) = - 3.6 and (b) = 5.6.

Keywords: ceramic pigments, Cu - chromophore, rice husk, solid-state sintering, color characteristics

INTRODUCTION

Inorganic ceramic pigments are used to color various materials, as well as to improve one or another property of the material. The color of the pigments is due to coloring ions such as cobalt, copper, nickel, etc. [1, 2]. These materials must have excellent chemical resistance [3], as well as resistance to high temperatures [4]. In addition, the pigments must be relatively chemically inert - they must not easily react with their carriers. They must be insoluble in water, organic solvents and binders [5]. Another requirement for them is to show good coverage, high color intensity and high refractive index [6].

Nowadays, ceramic pigments are used to color various ceramic materials. They are obtained by solid-phase synthesis [7, 8] or by sol-gel technology [9, 10]. Of particular interest, both from a scientific and an applied ecological aspect, is the production of ceramic pigments not only from pure but from waste raw materials. More and more scientific studies report on the synthesis of ceramic pigments using industrial waste [11], biowaste [12], spent catalysts, etc. [13].

Scientists create more stable pigments with a higher color intensity compared to pigments from pure SiO₂ [14, 15].

The development and production of various ceramic pigments using agro-waste is poorly represented. The lack of sufficient data, especially in recent years, on the synthesis of ceramic pigments, as well as their detailed study, makes the current research timely and useful for filling the existing niche.

In connection with the above, the aim of the present study is the synthesis of ceramic pigments from the Al₂O₃ - SiO₂ system, by the solid-phase sintering method, from pure raw materials and waste ones, by using rice husk ash as a source of silicon dioxide. Also, the starting batches are studied and the characteristics of the obtained pigments are determined.

EXPERIMENTAL

Materials and methods

• *Materials*. The synthesis of finely dispersed ceramic pigments from the Al₂O₃ - SiO₂ system was carried out by the solid-phase sintering method. Both pure materials and waste raw materials - ash from burnt rice husks were used as starting materials.

Two series of pigments were synthesized. In the first case, pure starting materials were used - Al₂O₃ and SiO₂.nH₂O (Sigma Aldrich) - compositions M2-5 and P2-5, Table 1. The more active amorphous form of SiO₂.nH₂O was chosen instead of the

^{*} To whom all correspondence should be sent: E-mail: adriana georgieva79@yahoo.com

crystalline form of silicon dioxide. Rice husk is a waste product, which is known to contain about 20% of SiO₂. By burning the rice husk in an oxidizing environment, the amount of SiO₂ significantly increases. For one of the purposes of the experiment (compositions MR2-5 and PR2-5, Table 1) ash from burnt rice husks (RHA) with a SiO₂ content of 94.47 % was used. Since the color of most natural and synthesized mineral substances is associated with the presence in their composition of d- or f-elements of the periodic system, in both starting compositions (from pure and from waste raw materials) Cu ions were selected and introduced as a chromophore in an amount of 5 %. The copper chromophore was introduced in the form of CuO.

Table 1. Compositions of ceramic pigments from the Al_2O_3 - SiO_2 system, synthesized from pure or waste raw materials (rice husk ash RHA) with 5 % of Cu chromophore.

№	Composition	Synthesis	SiO ₂ introduced
		temperature	in the form of:
1	M2-5	1350 °C	SiO ₂ .nH ₂ O
2	MR2-5	1350 °C	RHA
3	P2-5	1400 °C	SiO ₂ .nH ₂ O
4	PR2-5	1400 °C	RHA

The initial components were dry-mixed and homogenized in a planetary ball mill. The synthesis of ceramic pigments was carried out at temperatures of 1350 °C and 1400 °C, and to ensure the completeness of the reactions that occur during solid-phase sintering, at the corresponding maximum temperature, a one-hour isothermal hold in a Nabertherm high-temperature furnace in an air environment was performed at the final stage of the process. The preparation of ceramic pigments including all procedures during the technological process, is schematically presented in Figure 1.

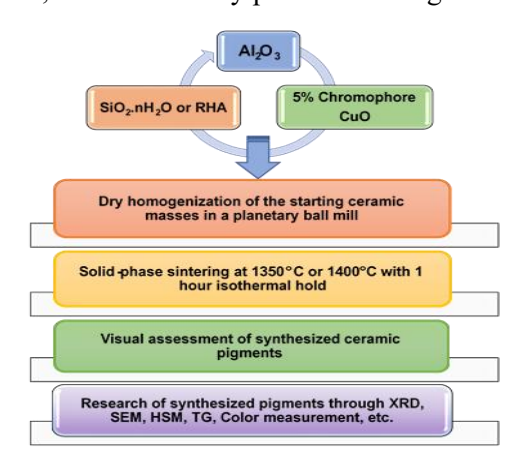


Figure 1. Scheme of the production of ceramic pigments from pure or waste raw materials by solid-phase sintering.

- *Methods*. The initial mixtures and the synthesized pigments were examined using the methods of:
- X-ray structural analysis. X-ray diffraction analysis was performed on a Bruker D8 Advance automatic powder X-ray diffractometer with CuKα radiation (Ni filter) and registration by a LynxEye solid-state detector. The X-ray spectrum was recorded in the angular range from 5.3 to 80° 2θ with a step of 0.03° 2θ. Qualitative phase analysis was performed using the PDF-2 (2009) database of the International Center for Diffraction Data (ICDD). Quantitative analysis was performed with the Topas 2 program.
- Scanning electron microscopy (SEM). The SEM observations were carried out on an apparatus TESCAN, SEM/FIB LYRA I XMU at 30 kV accelerating voltage. The observations were accompanied by energy-dispersive X-ray spectroscopy (EDS) carried out with a detector of Bruker.
- Hot-stage microscopy (HSM) Hightemperature microscope ESS Misura HSM - 1400 ODHT, model 1600/80, Italy (IFH-BAS) was used. The sample was heated to 1400 °C at a rate of 10 °C min⁻¹, and the graph reflects the changes occurring with it during heating.
- Thermogravimetric analysis (TG). Thermogravimetric analysis was performed on a complex thermal analysis apparatus (STA 449 F3 Jupiter), Netzsch, Germany, by heating to 1100 °C at a rate of 10 °C min⁻¹.
- Color measurement. The color of the pigments was spectrally determined on a Lovibond Tintometer RT 100 Color.

RESULTS AND DISCUSSION

Two series of finely dispersed ceramic pigments of the Al_2O_3 - SiO_2 system were synthesized by the solid-phase sintering method at temperatures of 1350 °C and 1400 °C. In the synthesis of the first series of pigments, pure starting materials were used - compositions M2-5 and P2-5. In the second series, a waste raw material was utilized - ash from rice husks burnt in air (RHA), as a source of silica - compositions MR2-5 and PR2-5.

The color of pigments is most often determined by d-d electron transitions or charge transfer and occurs only in compounds of transition elements since their electronic structure allows such a transition. That is why, in the syntheses carried out, in both starting compositions (from pure and from waste raw materials) 5% of Cu chromophore was introduced as CuO. The starting batches and the ceramic pigments obtained by us were studied and characterized using the methods of XRD, SEM, HSM, and TG, and the color characteristics of the pigments were spectrally determined with a Lovibond Tintometer RT 100 Color.

Studies on initial mixtures

Fig. 2 presents the results from the hot-stage microscopy (HSM) of a mixture obtained from pure raw materials - Al₂O₃ and SiO₂.nH₂O.

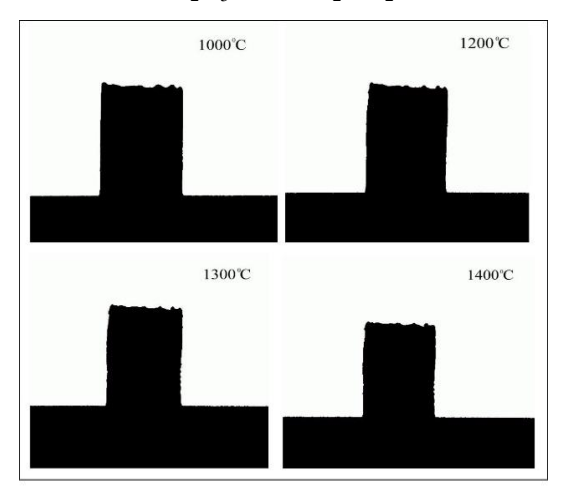


Figure 2. Hot-stage microscopy (HSM) of mixtures obtained from pure raw materials - composition P2-5.

The results indicate an extremely high thermal stability of the studied samples, even at a temperature of almost 1400 °C. This shows that the synthesized pigments are highly refractory and will not decompose during the firing of ceramic products covered with glazes colored with the pigments obtained by us. Therefore, the pigments could be used in real production conditions.

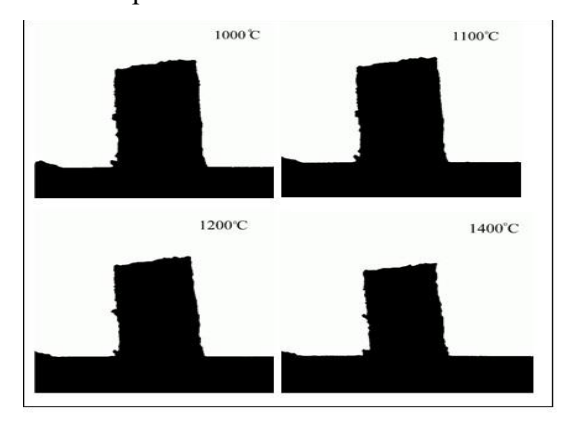


Figure 3. Hot-stage microscopy (HSM) of mixtures obtained from Al₂O₃ and waste RHA - composition PR2-5.

Fig. 3 presents the results of hot-stage microscopy (HSM) of batches composed of Al₂O₃ and air-burnt rice husk ash (RHA). It can be seen that the introduction of RHA, as a source of SiO₂ into the starting compositions, also gives high-temperature resistant batches. No spillage or shape change are observed up to almost 1400 °C.

The starting mixtures, consisting of Al₂O₃ and pure or waste raw materials, were also studied by means of thermogravimetric analysis. The complex thermal analysis shows that the process consists of several main stages of mass loss. DSC and DTG thermograms are presented in Figs. 4 and 5. Until a stable regime is reached in the complex thermal analysis apparatus, adsorption processes of moisture in the dry samples prevail, due to which the mass increases, after which the desorption process takes priority and the mass decreases. The first two lowtemperature endothermic stages in both charges proceed with mass loss, consisting mainly of water physically adsorbed on the surface of the material. The next stage is characterized by the endothermic peak in the range of 500 - 550 °C (Fig. 4), which corresponds to the dehydration of SiO₂.nH₂O. In Fig. 5 a large endothermic effect is observed between 400 - 500 °C, both in height and area. Here the mass loss is the greatest, which is probably a result of the combustion of unburnt particles in the RHA.

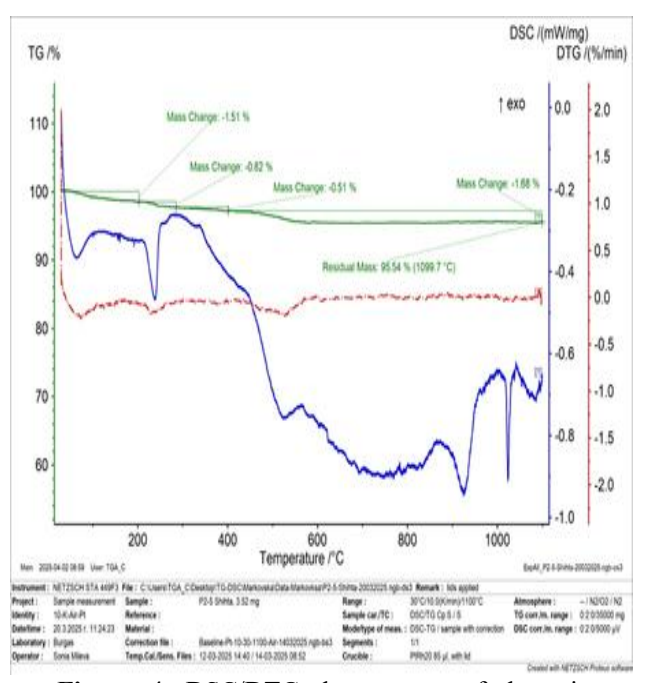


Figure 4. DSC/DTG thermogram of the mixture obtained from pure raw materials: Al₂O₃ and SiO₂.nH₂O.

F. S. Yovkova et al.: Synthesis and properties of Cu - doped finely dispersed ceramic pigments

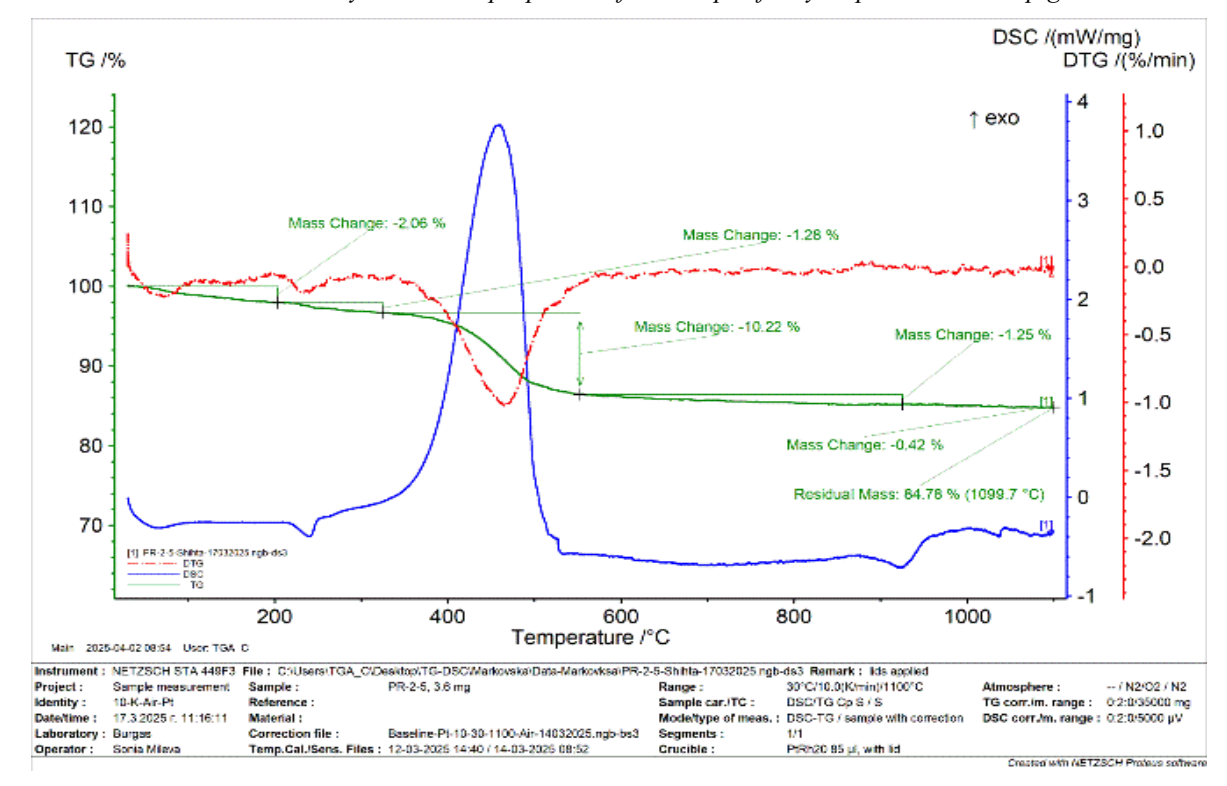


Figure 5. DSC/DTG thermogram of the batch obtained from Al₂O₃ and waste RHA

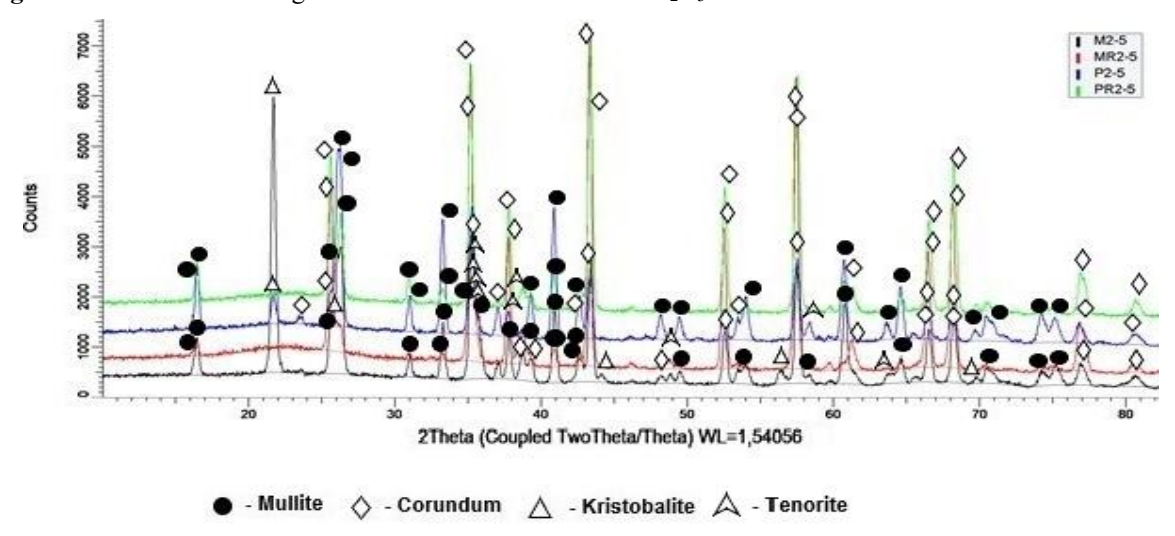


Figure 6. X-ray diffraction patterns of synthesized pigments in the Al_2O_3 - SiO_2 system

Table 2. Phase composition of pigments from the Al_2O_3 - SiO_2 system, synthesized from pure or waste raw materials, with a Cu chromophore in the amount of 5%. Mass content and crystal size

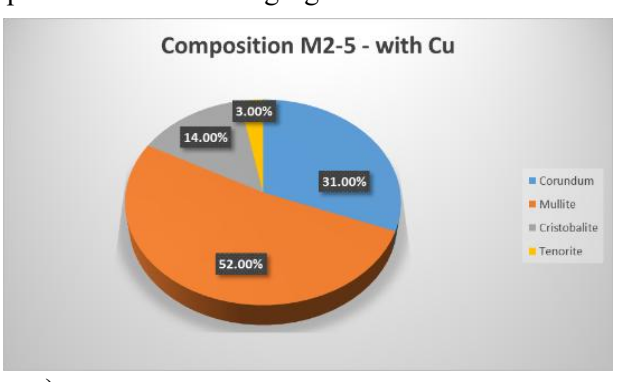
Sample	Corundum mass%, crystal size	Cristobalite mass%, crystal size	Mullite mass%, crystal size	CuO mass%, crystal size
M2-5	31%, 47nm	14%, 32nm	52%, 38nm	3%, 29nm
MR2-5	86%, 55nm	-	11%, 44nm	3%, 36nm
P2-5	17%, 54nm	3%, 22nm	78%, 44nm	2%, 34nm
PR2-5	71%, 57nm	-	27%, 46nm	2%, 52nm

Studies on pigments synthesized at temperatures of 1350 °C and 1400 °C

X-ray diffraction patterns of ceramic pigments synthesized by the solid-phase sintering method from pure or waste raw materials (rice husk ash RHA) with 5% of Cu chromophore are presented in Fig. 6. The sizes of the formed crystals vary between 22÷57 nm (Table 2).

The phase composition of the studied samples was determined from the X-ray diffraction analysis data. It can be seen that the main phases in the synthesized pigments are corundum (Al₂O₃) and mullite (3Al₂O₃.2SiO₂), and reflexes of cristobalite (SiO₂) and tenorite (CuO) are also observed. With increasing heat treatment temperature, a tendency is observed for the intensity of the peaks of the main phases to increase.

The X-ray diffraction results show that during high-temperature firing, SiO₂ almost completely reacts and mullite is formed, and the high-temperature modification of SiO₂ - cristobalite (compositions M2-5 and P2-5 with pure starting materials) is also noticeable. In pigments with the participation of waste raw materials (rice husk ash RHA), the predominant phase is corundum. For better visualization, the results presented in Table 2 are also interpreted through quantitative diagrams placed in the following figures.



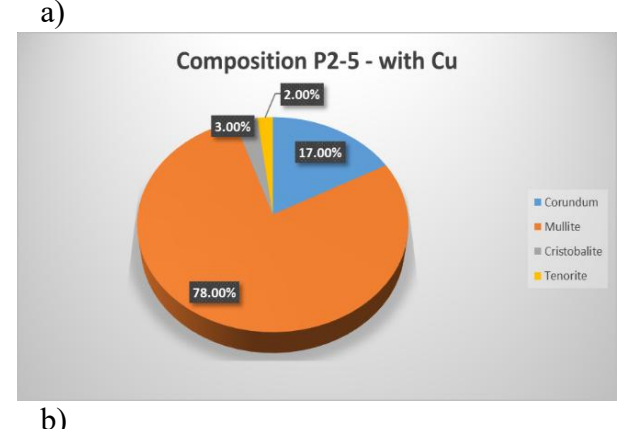
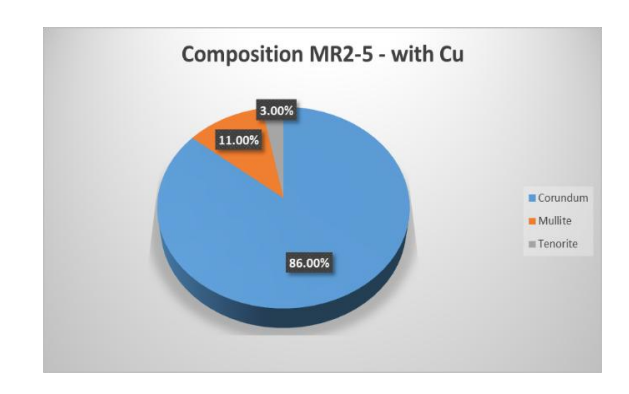


Figure 7. Quantitative diagrams of the X-ray phase analysis of the compositions a)- M2-5; b) - P2-5..



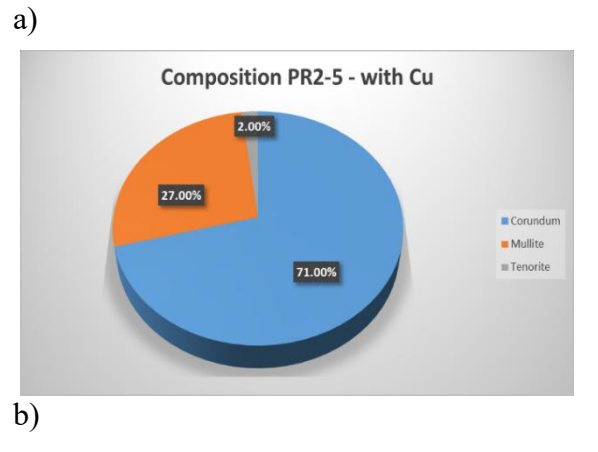


Figure 8. Quantitative diagrams of the X-ray phase analysis of the compositions – a) MR2-5 and b) - PR2-5.

Using the CIELab system which gives a numerical expression of the visual sensation of color, the basic color characteristics of the pigments were determined - color, brightness, color hue.

In the CIELab system, the color coordinates are as follows:

- L^* brightness, $L^*=0$ black color, $L^*=100$ white color;
 - a* green color (-) / red color (+);
 - b* blue color (-) / yellow color (+).

The results of the determined color parameters of the synthesized pigments from pure or waste raw materials, with chromophore Cu (5 %), are presented in Table 3.

Table 3. Color characteristics of the synthesized pigments at temperatures of 1350 °C and 1400 °C

No	Composition	Color	L*	a *	b *
1	M2-5		56.9	-3.1	1.1
2	MR2-5		34.0	-2.4	2.5
3	P2-5		38.7	-3.6	5.6
4	PR2-5		35,8	-1.8	3.4

The pigments with the best color characteristics are those obtained from pure raw materials (composition P2-5 - Al_2O_3 and $SiO_2.nH_2O$) at 1400 °C for 1 hour - (a) = -3.6 and (b) = 5.6.

Fig. 9. presents a SEM micrograph of ceramic pigments of the Al_2O_3 - SiO_2 system, synthesized at 1350 °C from pure starting materials (composition M2-5 - Al_2O_3 and $SiO_2.nH_2O$).

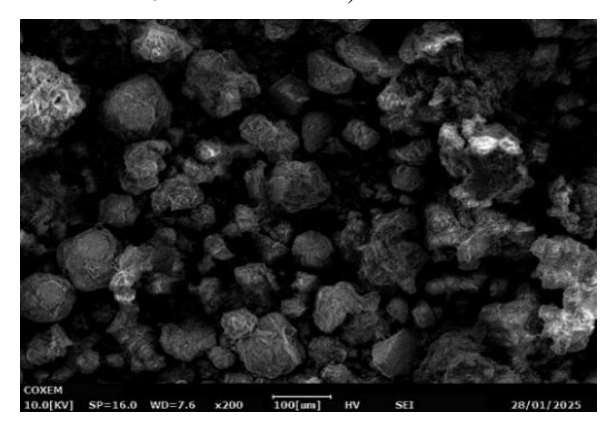
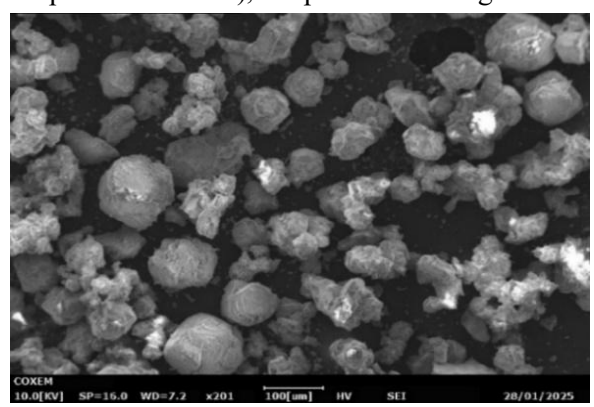


Figure 9. SEM image of pigments with composition M2-5 (Al₂O₃ and SiO₂.nH₂O), synthesized at 1350 °C.

SEM micrographs of pigments synthesized at 1350 °C from waste raw materials - Al₂O₃ and RHA (composition MR2-5), are presented in Fig. 10.



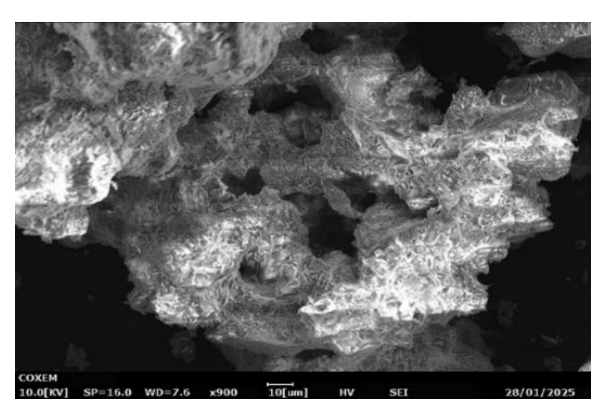


Figure 10. SEM images of pigments with composition MR2-5 (Al₂O₃ and RHA), synthesized at 1350 °C

The SEM analysis shows that clusters of particles are formed, with a size of around and below 100 nm.

The coarse shape of the particles indicates the high degree of crystallinity of the obtained pigments.

CONCLUSION

The synthesis and properties of finely dispersed ceramic pigments from the Al₂O₃ - SiO₂ system were studied. The synthesis of both series of pigments was carried out by the solid-phase sintering method. In the first case, pure starting materials were used -Al₂O₃ and SiO₂.nH₂O, and the more active amorphous form of SiO2.nH2O was chosen, instead of the crystalline form of SiO₂. For the preparation of the second series of pigments, ash from burnt rice husks with a SiO₂ content of - 94.47 % was used and utilized. The syntheses were carried out at temperatures of 1350 °C and 1400 °C with 1-hour isothermal hold. In both starting compositions - from pure and from waste raw materials, the amount of chromophore was 5% Cu introduced in the form of CuO. Finely dispersed pigments in the gray color range were obtained.

The synthesized pigments from the Al₂O₃ - SiO₂ system were studied using a number of methods, such as XRD, SEM, HSM, and TG. The phase composition of the studied samples was determined from X-ray structural analysis data. It was found that the main phases in the synthesized pigments are corundum and mullite, and reflections of cristobalite and tenorite were also observed. The sizes of the formed crystals in the samples vary between 22÷57 nm. The morphology and the structure of the obtained pigments were studied by SEM which shows that clusters of particles with a crystalline structure are formed. The color characteristics of the pigments were spectrally determined with a Lovibond Tintometer RT 100 Color. The pigments with the best color characteristics are those obtained from pure raw materials (Al₂O₃ and SiO₂.nH₂O) and baked at 1400 °C - resp. (a) = -3.6 and (b) = 5.6.

Acknowledgement: The financial support of this work by the Bulgarian Ministry of Education and Science, National Research Fund under the contract number KP-06-N87/14 is gratefully acknowledged.

- 1. M. Rodrigo, et al., Open Ceramics, 19, 100638 (2024).
- 2. S. Chokkha, et al., J. Mater. Cycles Waste Manag., **25**, 998 (2023) 10.1007/s10163-022-01581-9.
- 3. S. Cheng, et al., Ceram. Int., 49(13), 22110 (2023).
- 4. M. Z. Heerah, et al., Case Studies in Construction Materials, 15, 1 (2021) https://doi.org/10.1016/j.cscm.2021.e00571.
- 5. S. Wei, et al., Additive Manufacturing Frontiers, 4 (1), 200182 (2025).

- 6. D. F. L. Horsth, et al., Beilstein Journal of Nanotechnology, 14, 467 (2023).
- 7. Y. Wang, et al., Solid State Sciences, 135, 107088 (2023).
- 8. K. L. Patrocínio, et al., Ceram. Int., **50**, 18, 31955 (2024).
- 9. Y. Xie, et al., Materials Today Communications, **40**, 110123, (2024).
- 10. G. G.-Vacas, et al., Results in Engineering, **26**, 105074, (2025).
- 11. V. M. Pogrebenkov, et al., Glass and Ceramics, **59** (11-12), 396 (2002).
- 12. F. Bondioli, et al., J. Eur. Ceram. Soc., 24, 14 (2004).
- 13. Ts. Ibreva, Ts. Dimitrov, et al., Bulg. Chem. Commun., **50**, 31 (2018).
- 14. F. Andreola et al., Dyes Pigments, 94, 207 (2012).
- 15. F. Andreola et al., Ceram. Int., 39, 5427 (2013).

Preparation and analysis of epoxy/organoclay composites – structural characterization and mechanical properties

V. A. Angelov^{1,2*}, R. K. Krastev¹, T. T. Batakliev^{1,2}

¹Institute of Mechanics, Bulgarian Academy of Sciences, Acad. G. Bonchev Str., Bl. 4, 1113 Sofia, Bulgaria

²Center of Competence for Mechatronics and Clean Technologies "Mechatronics, Innovation, Robotics, Automation and Clean Technologies" MIRACle, Bulgaria

Received: April 02, 2025; Revised: July 09, 2025

The present research aims to obtain epoxy composites with organoclay filler and to investigate some of their mechanical properties. Epoxy composites were obtained at the Laboratory "OLEM" of the Institute of Mechanics-BAS and the mechanical characteristics (Young's modulus and strength in compression) were tested on a TIRAtest 2300 machine. Epoxy composites with fillers - C20A, C30B, 1.44 P, 1.28 E, 1.31 PS showed worse mechanical properties than neat epoxy resin. Composites with organoclay 1.34 TCN showed slightly better mechanical properties, compared to pure epoxy resin. X-ray diffraction (XRD) measurements were performed on the organoclay epoxy composites. Using the peak position (2θ) in the XRD patterns, the inter-layer spacing was calculated through Bragg's law.

Keywords: Preparation, organoclay, epoxy resin, XRD

INTRODUCTION

Polymer-clay nanocomposites (PCNs) are a new class of materials consisting of a polymer matrix and nanoclay as a reinforcing filler [1, 2]. Depending on the application, the polymer matrix can be thermoset, thermoplastic, rubber, or co-polymers. The first PCN, synthesized by the Toyota R & D group in Japan in 1992, used nylon-6 as the matrix and nanoclay as the filler, marking an important milestone in the development of high-performance composite materials.

One of the main reasons for the growing interest in PCNs is the unique reinforcement potential of layered silicate clays, which offer a high aspect ratio, large surface area, and low cost. However, untreated clay is naturally hydrophilic and therefore not easily dispersed in most polymers, which are typically hydrophobic [3]. This incompatibility often results in poor dispersion and limited improvements in the final material properties.

To overcome this challenge, various surface modification techniques have been developed to enhance clay compatibility with organic polymers. Among these, organo-treated montmorillonite clay has emerged as one of the most widely used nanofillers due to its superior compatibility with polymer matrices, high specific surface area, aspect ratio, and improved dispersibility at the nanoscale [4].

Montmorillonite, a nanoclay mineral belonging to the smectite group, has a layered structure and high cation exchange capacity, which enables ion exchange with its environment [5]. This versatile mineral is commonly found in bentonite deposits formed from volcanic ash weathering, with significant sources in the United States, China, and Greece, among other regions [6]. Such properties make it suitable for surface modification to enhance compatibility with epoxy resins.

Despite the advantages of organoclays, challenges remain in maintaining their structure during composite preparation. For example, when used as a nanofiller, Cloisite® 30B (C30B) often undergoes d-spacing collapse, as demonstrated by the shift to wider angles in the XRD basal reflection. This collapse has been attributed to contamination or, more often, to thermal degradation of the organic modifier during processing [7]. Recent work has shown that factors such as filler content, particle size, and environmental exposure can significantly affect the structural stability and performance of these composites [9–11].

In this study, epoxy/organoclay composites were prepared and systematically analyzed to address these challenges. In particular, the work focuses on a comparative investigation of different organoclay fillers in epoxy resin systems — an area that is not widely studied. By comparing the structural

© 2025 Bulgarian Academy of Sciences, Union of Chemists in Bulgaria

^{*} To whom all correspondence should be sent: E-mail: *v.angelov@imbm.bas.bg*

characteristics and mechanical properties of composites prepared with various organoclay modifications, this research aims to clarify how different treatments affect clay dispersion, interlayer spacing, and the overall performance of the final material. The goal of this work is to achieve improved compressive strength through the preparation of composites with intercalated structures. This study aims to provide new insights that will support the development and optimization of high-performance epoxy/organoclay nanocomposites.

EXPERIMENTAL

Materials

In the present study, several organoclays were used as fillers in the epoxy resin (matrix) to produce organoclay-epoxy composites. Clay Cloisite® 30B (Southern Clay Products, Inc.), organically modified with methyl tallow bis-2-hydroxyethyl quaternary ammonium chloride (MT2EtOH); Clay Cloisite 20A (Southern Clay Products, Inc.), containing organic modifiers - dimethyl, dihydrogenated tallow, quaternary ammonium; Nanoclay I.44P containing an organic modifier - 35-45 wt. % of dimethyl dialkyl (C14-C18) amine; Nanoclay I.31PS containing 15-35 wt. % of octadecyl-amine, 0.5-5 wt. % of aminopropyltriethoxysilane; Nanoclay I.34TCN containing 25-30 wt. % of methyl dihydroxy-ethyl hydrogenated tallow ammonium; and Nanoclay I.28E containing 25-30 wt. % of trimethyl stearyl ammonium. All nanoclays are produced by Sigma-Aldrich.

Epoxy resin prepolymer Epilox T 19-38/500 (liquid oligomer, $\eta = 450-550$ mPa.s at 25 °C) and amine hardener Epilox H 10–30 ($\eta = 200-300$ mPa.s at 25 °C) were purchased from Leuna-Harze GmbH (Germany) and were used as received.

Preparation method

All organoclays were dried at 80 °C for 8 h at the start of the preparation protocol. For the preparation of binary nanodispersions, the appropriate amount of organoclay was added to the liquid epoxy resin oligomer and the mixture was homogenized for 30 min by mechanical mixing at 10 000 rpm, followed by 30 min ultrasonication treatment at 250 W. The obtained clay/epoxy nanodispersions were then degassed in a vacuum set. The solid binary clay/epoxy nanocomposites were prepared from the nanodispersions using an *in-situ* polymerization method. The appropriate amount of the amine hardener was added to the respective dispersions at a molar ratio of *epoxy resin:hardener* = 100:49. The

mixture was poured into a cylindrical mold and cured for 24 h at room temperature followed by post-curing at 100 °C for 4 h.

Characterization methods

The moisture content in the organoclays before and after the drying procedure was measured using the moisture analyzer MX-50 from A&D Company Ltd. The moisture content is determined on a wet basis, meaning it is calculated as the difference between the wet sample mass and the dried sample mass, divided by the wet sample mass, and expressed in percentage. The X-ray diffractograms were obtained by using Bruker D8 Advance diffractometer with Cu K α radiation (λ = 0,15418 nm) and LynxEye detector.

The mechanical properties (Young's modulus and compressive strength) were tested on a TIRAtest 2300 machine at the Institute of Mechanics - BAS. The specimens with 15 mm initial diameter and 29 mm height were compressed at a velocity of 2 mm/min.

RESULTS AND DISCUSSION

Powder XRD analysis

The prepared composites were analyzed using XRD to determine the distance between the organoclay layers in the prepared epoxy-organoclay composites. The inter-layer spacing increases in the intercalated composites shown in Fig. 1b, which is associated with improved mechanical properties of the produced materials [12, 13].

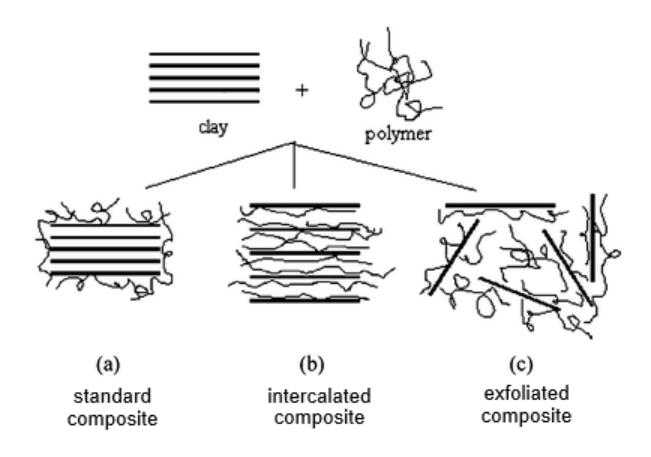


Fig. 1. Types of composites [14]

For all organoclays, the distances between the layers, reported by the producer, are summarized in Table 1. These distances were compared to the measured distances between the layers in the prepared composite. Based on this, the type was inferred, the increase of the inter-layer distance indicating intercalated composite type.

Table 1. Distance between the layers of organoclays

Samples (powder)	Distance (nm)
C30B	1.81
C20A	2.32
1.44 P	2.66
1.34 TCN	1.86
1.31 PS	2.18
1.28 E	2.45

The moisture content in the organoclays was reduced using a drying process to improve the homogenization process. The drying process was controlled by measuring the moisture content before and after the drying.

The results shown in Table 2 indicate that all organoclays were well dried after the drying procedure. The thermal treatment of the organoclays is reported to have an impact on the inter-layer distance [8]. In the current study, the inter-layer distance was not measured after the drying process, but was left as a subject to a future study.

Table 2. Moisture content of organoclays

Samples	Moisture content (%)		
Samples (powder)	Before drying	After drying 80 °C / 8 h	
C30B	1.4	0.1	
C20A	1.4	0.1	
1.44 P	1.0	0.1	
1.34 TCN	1.5	0.1	
1.31 PS	0.8	0.1	
1.28 E	2.5	0.1	

The X-ray diffraction patterns of epoxy composites with the six types of organoclays are illustrated in Fig 2.

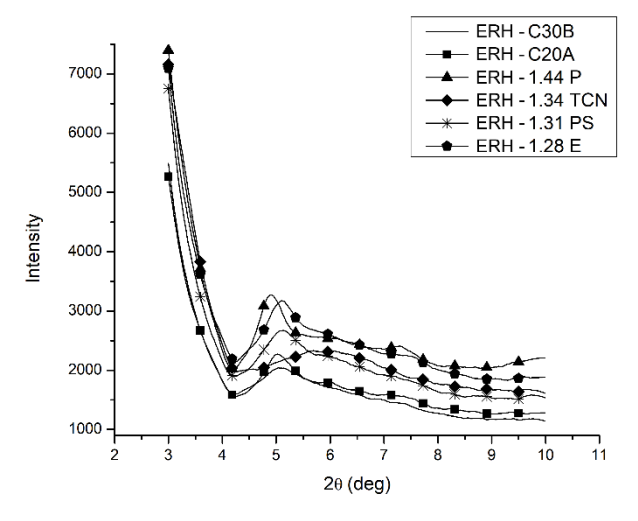


Fig. 2. XRD patterns of the obtained epoxy composites.

Using the peak position (2θ) in the XRD patterns, the inter-layer spacing was calculated through Bragg's law:

$$n\lambda = 2d \sin \theta$$

where λ is the wavelength of the incident wave ($\lambda = 0.15418$ nm), d is the spacing between the layers of organoclay in the composites.

The inter-layer spacing values calculated from the XRD analysis of the six composites are summarized in Table 3. In all six composites, a collapse of silicate layers (decrease in inter-layer distance) was observed. This suggests that the prepared composites are of the standard type indicated in Fig. 1a.

Table 3. Distance between the layers of organoclays in the epoxy composites shown in Fig. 2.

Samples (composites)	2θ (deg)	Distance (nm)
ERH - C30B	5.087	1.74
ERH - C20A	5.028	1.76
ERH - 1.44 P	4.910	1.80
ERH - 1.34 TCN	5.894	1.50
ERH - 1.31 PS	5.126	1.72
ERH - 1.28 E	5.107	1.73

Mechanical properties

The comparison of the Young's modulus of the six composites with that of neat epoxy resin is shown in Fig. 3.

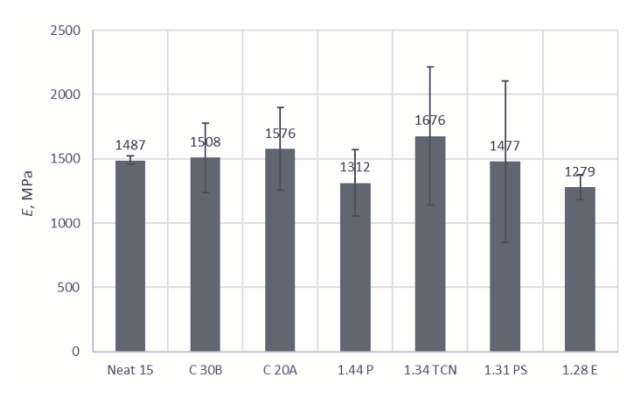


Fig. 3. Young' modulus of neat epoxy resin and organoclay-epoxy composites.

All the composites showed a higher dispersion of results than the neat resin. The 1.34 TCN composite indicated a higher elastic modulus, while 1.44 P and 1.28 E composites had lower moduli.

In Fig. 4 the compressive strength of the prepared composites was compared to that of neat epoxy resin. The results are similar to those for the modulus. There was only a slight improvement in the compressive strength of the composite 1.34 TCN. Composites C30 B and C20 A showed similar strength, and the rest of the composites showed a

decrease in the compressive strength. All tested samples showed elastic behavior up to about 2.6% deformation, with peak compressive strength occurring near 5% strain.

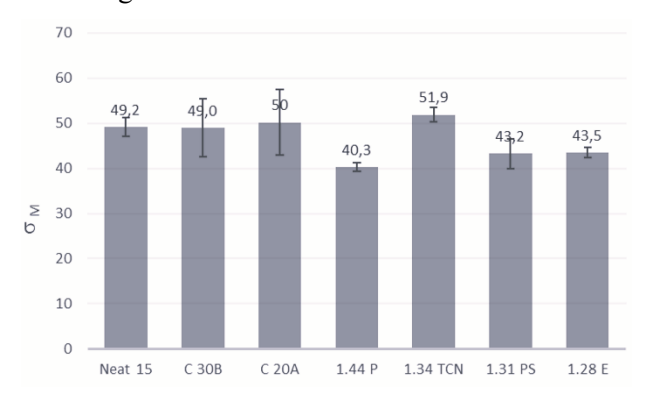


Fig. 4. Compressive strength of neat epoxy resin and organoclay-epoxy composites.

CONCLUSION

In the present study, several different nanofillers (organoclays) were investigated - C30B, C20A, 1.44 P, 1.34 TCN, 1.31 PS and 1.28 E. In all the six synthesized nanocomposites we observed a collapse of silicate layers (inter-layer distance has decreased). Only the epoxy nanocomposite with 1.34 TCN nanofiller showed slightly better mechanical properties than neat epoxy resin. The XRD diagram of the composite with 1.34 TCN organoclay showed the lowest inter-layer spacing compared to the other composites. The measurement of the impact of the drying procedure on the inter-layer spacing in the organoclays and its potential contribution to the collapse of silicate layers, observed in the final composites, is left as a subject for future study.

Acknowledgement: This work is supported by the Competence Center for Mechatronics and Clean

Technologies — MIRACle, developed by the Operational Programme "Science and Education for Smart Growth" (2014–2020) and Program "Research, Innovation and Digitalization for Smart Transformation" 2021-2027 (PRIDST), co-financed by the European Union through the European Structural and Investment Funds. The authors would like to express also their sincere gratitude to the Bulgarian National Science Fund (BNSF) under Grant No. KP-06-H77.

- 1. T. J. Pinnavaia, Science, **4595**, 365 (1983).
- Y. Fukushima, A. Okada, M. Kawasumi, T. Kurachi,
 O. Kamigaito, *Clay Minerals*, 23, 27 (1988).
- 3. W. Liu, S. V. Hoa, M. Pugh, Composites Science and Technology, **65**, 307 (2005).
- 4. R. Velmurugan, T. P. Mohan, *Journal of Reinforced Plastics and Composites*, **28** (2009).
- 5. F. Uddin, Metall. Mater. Trans. A, 39, 2804 (2008).
- 6. H. H. Murray, *Acta Geodyn. Geomater.*, **2**, 127 (2005).
- S. Filippi, M. Paci, G. Polacco, N. Dintcheva, P. Magagnini, *Polymer Degradation and Stability*, 96, 823 (2011).
- 8. S. Shelly, M. Mishra, *Materials*, **8**(12), 506 (2024).
- 9. A. Shettar, N. Kowshik, *Polymers and Polymer Composites*, **30**(4), 331 (2022).
- 10. T. D. Ngo, T. Ton-That, S. V. Hoa, *Advanced Composites and Hybrid Materials*, **4**, 1091 (2021).
- 11. K. Lee, J. Park, Polymers, 16(1), 55 (2024).
- 12. S. S. Ray, M. Okamoto, *Progress in Polymer Science*, **28**(11), 1539 (2003).
- 13. M. Müller, L. Gonçalves, A.L. Mendes, *Journal of Applied Polymer Science*, **139**(10), e51852 (2022).
- B. Chen, J. R. G. Evans, H. C. Greenwell, P. Boulet, P. V. Coveney, A. A. Bowden, A. Whiting, *Chem. Soc. Rev.*, 37, 568 (2008).

Electrocatalytic oxidation of H₂S by a ZrO₂ catalyst on biochar carbon

N. Shukova^{1*}, D. Uzun², E. Razkazova-Velkova¹, K. Petrov² A. Gigova², O. Dimitrov², M. Dimitrova², L. Ljutzkanov¹

¹Institute of Chemical Engineering, Bulgarian Academy of Sciences, Acad. G. Bonchev Str., Bl. 103, Sofia 1113, Bulgaria

Received: April 01, 2025; Revised: July 31, 2025

A catalyst based on ZrO₂ incorporated into a biochar carbon matrix was synthesized. The biochar was obtained from pyrolyzed sunflower husks. The ZrO₂ deposit onto carbon sunflower husks (ZCSH) was intended for usage in the electrooxidation of sulfide ions from a model solution containing 65 mg/l of S²⁻ and 18 g/l of NaCl. The electrocatalyst was characterized by scanning electron microscopy, X-ray diffraction and BET. Electrodes were manufactured with different amounts of catalyst (20 to 80 mg/cm²), binder (Teflon®) and Vulcan® XC-72. Their electrochemical properties were studied by means of cyclic voltammetry, galvanostatic measurements and Tafel slopes. The electrodes with 40 mg/cm² of catalytic mass within the electrode exhibited a lower overvoltage following the galvanostatic measurements.

Keywords: Hydrogen sulfide, ZrO2 catalyst, Fuel cells, Electrodes

INTRODUCTION

The origin of sulfides can be generally divided into natural and anthropogenic. Natural sources include volcanoes, hot springs, and closed deep-sea basins (where sulfides are formed from sulfurcontaining organic matter by sulfate-reducing bacteria). The main anthropogenic pollution with sulfides stems from the petroleum, leather, pulp and textile industries, sewage systems and wastewater treatment plants [1, 2]. The conventional methods for treatment of such effluents are sorption methods, that can be combined with oxidation with strong oxidants [3-7], precipitation with metals [8] or biological oxidation [9-11]. Thermal and electrical methods for decomposition are also developed [12, 13]. The Claus process is a classical method but it requires high temperatures and specific catalysts [14]. There are many catalysts and photocatalysts that convert H₂S in gaseous [10, 15–16] or dissolved form of sulfur. It is reported that Me²⁺ cations (Me=Mn, Co, Ni, Fe, Cu) catalyze the process of oxidation of H₂S [17, 18]. In many cases the main product is elemental sulfur that is undesirable both of environmental point of view and because it inhibits the oxidation by blocking the active sites of the catalyst. The processes that involve adsorption on different adsorbents in many cases use waste organic products for deriving adsorbents. This is a promising trend for the circular economics [19, 20] by converting wastes to valuable products. Biochar,

produced from agricultural wastes or sludge [21–24] limited-oxygen conditions, is rapidly emerging as an environmental restoration material. It is cheap, of large surface area, low cost, low energy consumption, high cation-exchange capacity, and stable structure [25]; it is a promising substitute for traditional anode catalysts which are expensive and environmentally harmful [26]. The biochar has high oxidation reduction reaction (ORR) catalytic activities. The latter is very important for the efficiency of fuel cells and metal-air batteries. It should be noted that biochar, as an electrocatalyst for microbial fuel cells (MFC), is a relatively new field, therefore, there is a wide scope for further investigations and applications [27]. Fuel cells (FC) and microbial fuel cells (MFC) are a promising new approach for decontamination of pollutants with simultaneous electricity generation [28, 29]. In our previous investigations, a catalyst for sulfide oxidation based on active carbon and ZrO₂ incorporated in a matrix of biochar, is reported [30, 31]. These studies are focused on the catalyst use for hydrogen sulfide wastewater treatment. In order to use a catalyst in fuel cells it is necessary to study its electrocatalytic properties and to design electrodes with suitable electrochemical characteristics.

The aim of the present study is to manufacture electrodes based on ZrO_2 over a biochar from sunflower husks, suitable for use in a FC.

²Institute of Electrochemistry and Energy Systems "Acad. Evgeni Budevski", Bulgarian Academy of Sciences, Acad. G. Bonchev Str., Bl. 10, Sofia 1113, Bulgaria

^{*} To whom all correspondence should be sent: E-mail: nastemil@abv.bg

MATERIALS AND METHODS

Catalyst preparation and characterization

The preparation method of the catalyst is a patented technology [32] that includes impregnation of the organic material (sunflower husks) with ZrCl₄ (Merck, ≥99.5% on trace metals basis) as a precursor salt and subsequent pyrolysis with simultaneous activation with water vapor and the flue gases from the pyrolysis. The process was conducted at 680 °C with a heating rate of 13°C per min and holding for 45 min at the final temperature. The obtained catalyst is ZrO2 incorporated into the activated carbon matrix at a ratio of 1:3. The ZrO2 incorporated into the biochar carbon matrix (ZCSH) was characterized by Brunauer-Emmett-Teller analysis (BET), X-ray diffraction analysis (XRD), and scanning electron microscopy analysis (SEM). XRD patterns were recorded on a Philips diffractometer using CuK radiation (λ =1.54178 Å, 40 kV and 30 mA) with a scanning rate of 2 min⁻¹. The scan range size was $10-100^{\circ}2\theta$ with 0.04° step size and 2s per step. The crystallite sizes (t) were determined by Scherer's formula: $t = \kappa \lambda / B\cos\theta$. where k is shape factor (k = 0.9 for spherical crystals with cubic symmetry), λ (Å) is the wavelength, θ is the diffraction angle of the peak, B (rad) is the line broadening at the FWHM (full width at half maximum) values of the peaks. BET studies were carried out on a Quantachrome Autosorb iQ (USA) instrument that measures the quantity of gas adsorbed onto or desorbed from a solid surface at an equilibrium vapor pressure by the static volumetric method.

The analytical procedures were applied in order to determine the morphology, surface area, pore diameter and distribution, etc. All the properties are important for characterization of a catalyst.

Electrode manufacturing

The electrodes were manufactured with Vulcan® XC72 (conductive carbon black, particle size ~ 50 nm, Merck) and Teflon® (PTFE powder, freeflowing, 1 µm particle size, Merck) as a binder. All electrodes had a geometric area of 1 cm² and were prepared from a mixture of catalyst, Teflon (35%) and Vulcan XC72 (60 mg/cm²). Different electrodes with 20 mg, 40 mg, 60 mg, 80 mg of ZrO2 catalyst and without a catalyst were obtained. The mixture (catalyst, Teflon and Vulcan XC72) was pressed on both sides of a current collector, which is a stainless-steel mesh (1 cm²) at 300 °C and a pressure of 300 atm.

Experimental equipment, conditions and electrochemical analysis

The electrolyte solution contained sodium sulfide (Na₂S.9H₂O, ACS reagent, ≥98.0%, Merck) and sodium chloride (NaCl, Merck). The concentration of S²⁻ in the electrolyte was 65 mg/l and that of NaCl - 18 g/l. These concentrations were chosen from our previous investigation [30] as those providing the most appropriate rate of oxidation. NaCl was added in order to improve the conductivity of the solution (this is the salinity of the Black Sea) [30]. The hydrogen sulfide from Black Sea can be utilized in fuel cells.

The 1 cm² electrodes were studied by cyclic voltammetry, steady-state polarization curves and Tafel analysis. The cyclic voltammetry measurements were done on a Solartron 1286 electrochemical The analyzer. polarization characteristics were determined on a Tacussell bipotentiostat type BI-PAD. Minimum three measurements were made for each result to achieve better reproducibility. Arithmetic averages are presented in the graphs. Galvanostatic measurements were made with Solartron 1286 (Fig. 1) at room temperature and a cell volume of 50 ml. The reference electrode was a reversible hydrogen electrode (RHE) (Gaskatel). The counter-electrode was platinum foil.

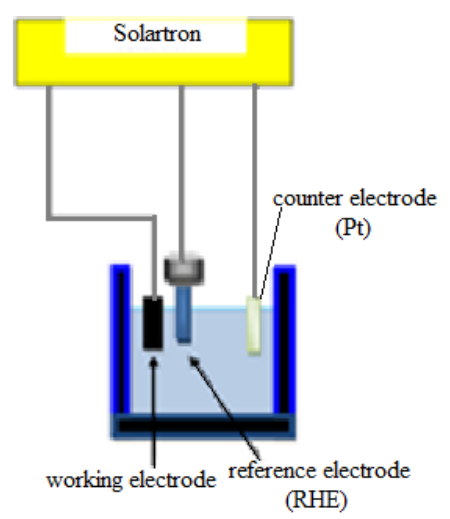


Fig. 1. Scheme of the three-electrode cell

RESULTS AND DISCUSSION

XRD studies

The samples were examined using a Philips X-ray diffractometer PW 1030.

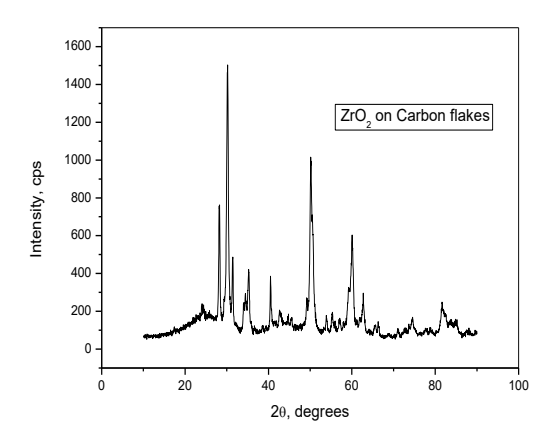
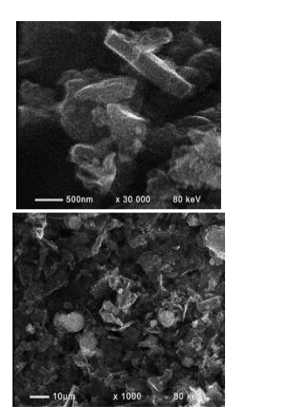


Fig. 2. XRD of the ZrO₂ on sunflower husks

In the literature peaks are observed at 2 theta for tetragonal and monoclinic zirconia, respectively [33]. In our studies XRD peaks, as presented in Fig. 2, are manifested at 24°, 28°, 30°, 35°, 40°, 50°, 60°, 63°, corresponding to the diffraction patterns of (111), (200), (220), (311), (222) and (400), likewise clearly tetragonal and monoclinic zirconia are present, matching the hexagonal wurtzite single crystal structure with the standard ZrO₂ (PDF card #82e1245).

SEM studies



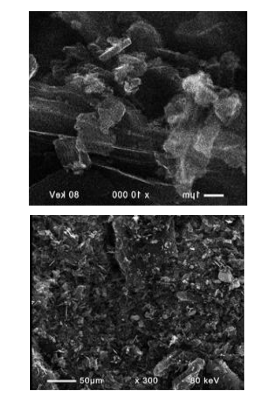


Fig. 3. SEM images of ZrO2 on sunflower husks

Scanning electron microscopy (SEM) images of the ZrO₂ surface morphology, obtained at different magnifications, are shown in Figure 3. The morphology of the pure ZrO₂ includes rectangular shapes of 20×500 nm. The material has an irregular network structure with a variety of large and small round particles, a rigorous structure with voids interacting with the solution, together with a hierarchy of channels aiding the processes of molecular diffusion leading to the catalytic reactions observed.

BET studies (surface area and pore size analysis)

Isotherms of the type shown in Figure 4 reveal that the adsorbate-adsorbent interactions are relatively weak. The steep vertical rise of the isotherms near P/Po=1 indicates the presence of macropores in the measured samples.

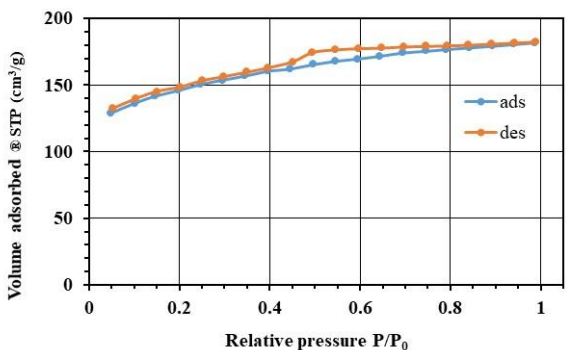


Fig. 4. BET isotherms of the ZrO₂ on sunflower husks

The specific surface area was determined by the BET method. Multipoint BET was determined at a relative pressure in the range p/p0 = 0.1-0.3; and single-point BET at p/p0 = 0.3. The pore volume was read at a relative measurement pressure close to 1 (p/p0 = 0.99). The pore diameter was calculated assuming that the pores have a cylindrical geometry, at p/p0 = 0.99. The results are summarized in Table 1

Table 1. BET structural characteristics of ZrO₂

Characteristics	Pure husk	ZrO ₂ onto biochar
Surface area (multi-point BET), m²/g	477	430
Surface area (single-point BET), m²/g	497	445
Total pore volume, cm ³ /g	0.301 for pores < 142 nm (D)	0.268 for pores < 160 nm (D)
Average pore diameter, (4V/S), nm	2.5	2.5

The presence of macro and mesopores facilitates the catalytical process, the adsorption of the reagents and the desorption of the products.

Polarization curve analysis

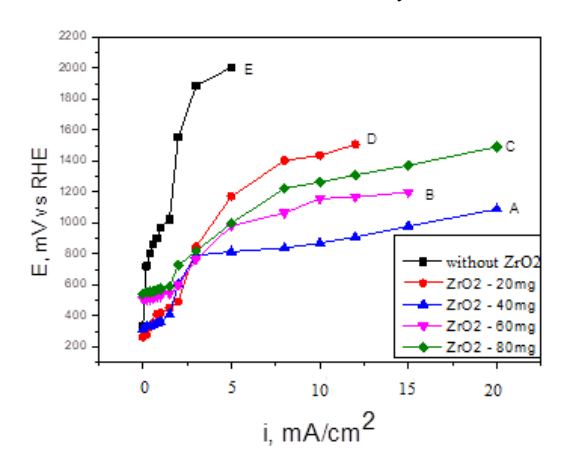


Fig. 5. Galvanostatic polarization curves of the electrodes as a function of the amount of ZrO₂ catalyst.

Figure 5 shows the polarization curves of the electrodes obtained for 20 mg, 40 mg, 60 mg, 80 mg of ZrO₂ catalyst, and without a catalyst. The figure shows that electrode (A) containing 40 mg of ZrO₂ catalyst and 60 mg of Vulcan XC-72 has the best electrochemical characteristics providing the lowest overpotential. The electrode containing 60 mg of ZrO₂ catalyst and 60 mg of Vulcan XC-72 provides a slightly higher overpotential and, hence, has inferior characteristics.

Tafel analysis

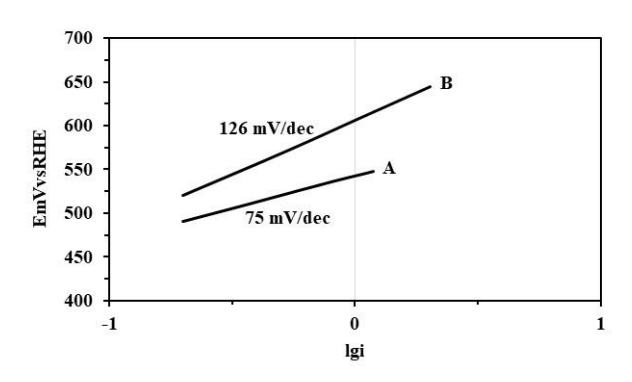


Fig. 6. Tafel slopes of electrodes containing 40 mg (A) and 60 mg (B) of ZrO₂ catalyst.

The Tafel slopes presented in Fig. 6 are of the two electrodes (A and B), with the best electrochemical characteristics given in the polarization curves shown in Fig. 5. The figure (Figure 6) shows that electrode A, containing 40 mg of ZrO₂ catalyst and 60 mg of Vulcan XC-72, possesses the best kinetic parameters. The results of Tafel slopes of 75 mV and 126 mV/dec, respectively, are close to literature data [34] for ZrO₂ catalyst. This improves the understanding of the electrocatalytic mechanisms of ZrO₂ catalyst supported on sunflower husks, but also

paves the way for its application in efficient and sustainable energy systems.

Cyclic voltammetry studies

It is observed that there are a pair of redox peaks for the electrode with 40 mg/cm². They can be found at 108, 90, 101 and 95 mV (Figure 7). The multiple peaks indicate the presence of electrochemical activity of the electrode in the selected solution. The availability of many peaks demonstrates the occurrence of different chemical reactions. This is to be expected, given the possibility of occurring of multiple chemical transformations of sulfur ions.

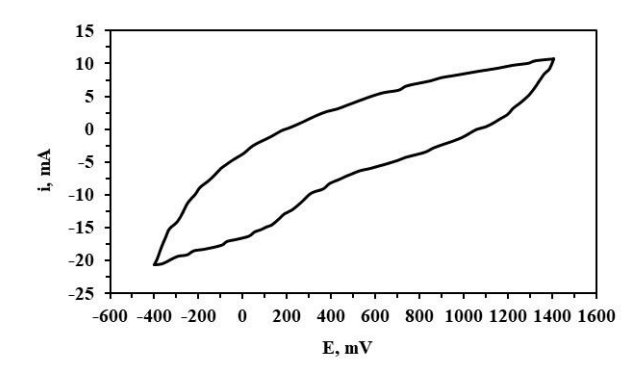


Fig. 7. Cyclic voltammogram of a ZrO₂ electrode, electrolyte (65 mg/l S²⁻ +18 g/l NaCl); $T = 25^{\circ}C$

CONCLUSIONS

ZrO₂ catalyst was synthesized on sunflower husks. It was characterized by XRD that showed tetragonal and monoclinic zirconia and hexagonal wurtzite single crystal structure of standard ZrO₂. The BET isotherms showed that the adsorbate-adsorbent interactions are relatively weak. The morphology of the pure ZrO₂ includes rectangular shapes of 20×500 nm. The material possesses an irregular network structure with a variety of large and small round particles.

At low current densities (up to 5 mA / cm²) the measured electrodes show similar characteristics. At high current densities, the electrode containing 40 mg of ZrO₂ catalyst and 60 mg of Vulcan XC-72 shows the best electrochemical characteristics.

Acknowledgement: This research was funded by the Bulgarian National Science Fund, Grant No KP-06-N67/6 from 12 December 2022.

- W. H. Smith, Encyclopedia of Biodiversity, 2nd edn., Explore book, 2001.
- 2. S. L. M. Rubright, L. L. Pearce, J. Peterson, *Environ. Toxicol. of hydrogen sulfide*, **71**, 1-13 (2017).
- 3. R. Cotrino, A.D. Levine, P. Amitzoglou, J. S. Perone, *Florida Water Res. J.*, (A-72), 22-25 (2007).
- M. Seredych, T. J. Bandosz, Chem. Eng. J., 128 (1), 59-68 (2007).
- 5. R. Wang, Sep. Purif. Technol., 31, 83-89 (2003).
- S. Yasyerli, I. Ar, G. Dogu, T. Dogu, *Chem. Eng. Process.*, 41 (9), 785-792 (2002).
- M. Tomar, T. H. A. Abdullah, Water Res., 28, 2545-2552 (1994).
- 8. M. Henze, P. Harremoës, J. la Cour Jansen, E. Arvin, Wastewater Treatment: Biological and Chemical Processes, 2nd edn., Springer, Berlin, 1997.
- T. Jia, L. Zhang, X. Li, Q. Zhao, Y. Peng, J. Sui, Ch. Wang, Sci. Total Environ., 857(Part 3), 1-20 (2023).
- 10. O. I. Dada, L. Yu, Sh. Neibergs, Sh. Chen, *Renew. Sustain. Energy Rev.*, **209**, 1-13 (2025).
- 11. G. Xia, Zh. Sun, J. Huang, J. Qi, J. Yao, *J. Environ. Manag.*, **367**, 1-20 2024.
- 12. G. Özgül, A. S. Koparal, Ü. B. Öğütveren, *Sep. Purif. Technol.*, **62**, 656 (2008).
- 13. J. Zaman, A. Chakma, Fuel Process. Technol., 41, 159-198 (1995).
- M. Capone, J. K. Kroschwitz, M. HoweGrant, Encyclopedia of Chemical Technology, 23, Wiley, New York, 1997.
- 15. Y. Xu, Zh. Ma, Zh. Wang, Ch. Liu, Y. Yang, *J. Ind. Eng. Chem.*, **136**, 524-531 (2024).
- Y. Yu, T. Zhang, L. Zheng, J. Yu, Chem. Eng. J., 225, 9-15 (2013).
- U.S. National Research Council, Hydrogen sulfide. Committee on Medical and Biologic Effects of Environmental Pollutants, 38 Subcommittee on Hydrogen Sulfide. University Park Press, Baltimore, MD, 1979.
- P. K. Dutta, K. Rabaey, Zh. Yuan, J. Keller, Water Res., 42, 317-322 (2008).

- T. Yuan, K. Hashimoto, A. Tazaki, M. Hasegawa, F. Kurniasari, Ch. Ohta, M. Aoki, N. Ohgami, M. Kato, J. Environ. Manage. 321 1-8 (2022).
- 20. D. Ouyang, Y. Chen, J. Yan, L. Qian, L. Han, M. Chen, *Chem. Eng. J.*, **370**, 614-624 (2019).
- S. Marzorati, A. Goglio, S. Fest-Santini, D. Mombelli, F. Villa, P. Cristiani, A. Schievano, *Int. J. Hydrogen Energy*, 44, 4496-4507 (2019).
- 22. J. Huang, H. Feng, Y. Jia, D. Shen, Y. Xu, *Water Sci. Technol.*, **80**, 1-17 (2019).
- 23. H.-C. Chang, W. Gustave, Z.-F. Yuan, Y. Xiao, Z. Chen, *Environ. Technol. Innov.*, **18**, 1043-1070 (2020).
- 24. X. Gong, L. Peng, X. Wang, L. Wu, Y. Liu, *Int. J. Hydrogen Energy*, **45**, 15336-15345 (2020).
- 25. Q. Hang, H. Wang, Z. Chu, B. Ye, Ch. Li, Z. Hou, *Environ. Sci. Pollut. Res.*, **23**, 8260 8274, (2016).
- 26. J. Lee, K.-H. Kim, E.E. Kwon, *Renew. Sustain. Energy Rev.*, 77, 70-79 (2017).
- 27. Sh. Li, Sh.-H. Ho, T. Hua, Q. Zhou, F. Li, J. Tang, *Green Energy & Environ.*, **6**, 1-16 2021, https://doi.org/10.1016/j.gee.2020.11.010.
- 28. L. Zhong, Sh. Zhang, Y. Wei, R. Bao, *Biochem. Eng. J.*, **124** (6), 6-12 (2017).
- 29. K. Wang, Sh. Zhang, Zh. Chen, R. Bao, *Chem. Eng. J.*, **341**, 184-190 (2018).
- 30. N. Dermendzhieva, E. Razkazova-Velkova, M. Martinov, L. Ljutzkanov, V. Beschkov, *J. Chem. Technol. Metall.*, **48** (5), 465-468 (2013).
- N. Dermendzhieva, E. Razkazova-Velkova, V. Beschkov, *Bulg. Chem. Commun.*, **52**, 35-38 (2020), ISSN: 0861-9808, DOI:10.34049/bcc.52.A.317.
- 32. L. Ljutzkanov, A. Atanasov, BG patent № 63594 /26.06.2002.
- 33. J. Chevalier, L. Gremillard, A.V. Virkar, D. R. Clarke, *J. Am. Ceram. Soc.*, **92** (9), 1901-1920 (2009), https://doi.org/10.1111/j.1551-2916.2009.03278.x
- 34. A. G. Rojek, Gr. Leniec, E. Mijowska, *Appl. Surf. Sci.* **684** (161851) 1-8 (2025).

Instructions about Preparation of Manuscripts

General remarks: Manuscripts are submitted in English by e-mail. The text must be prepared in A4 format sheets using Times New Roman font size 11, normal character spacing. The manuscript should not exceed 15 pages (about 3500 words), including photographs, tables, drawings, formulae, etc. Authors are requested to use margins of 2 cm on all sides.

Manuscripts should be subdivided into labelled sections, e.g. INTRODUCTION, EXPERIMENTAL, RESULTS AND DISCUSSION, etc. **The title page** comprises headline, author(s)' names and affiliations, abstract and key words. Attention is drawn to the following:

- a) **The title** of the manuscript should reflect concisely the purpose and findings of the work. Abbreviations, symbols, chemical formulae, references and footnotes should be avoided. If indispensable, abbreviations and formulae should be given in parentheses immediately after the respective full form.
- b) **The author(s)'** first and middle name initials and family name in full should be given, followed by the address (or addresses) of the contributing laboratory (laboratories). **The affiliation** of the author(s) should be listed in detail (no abbreviations!). The author to whom correspondence and/or inquiries should be sent should be indicated by an asterisk (*) with e-mail address.

The abstract should be self-explanatory and intelligible without any references to the text and containing up to 250 words. It should be followed by keywords (up to six).

References should be numbered sequentially in the order, in which they are cited in the text. The numbers in the text should be enclosed in brackets [2], [5, 6], [9–12], etc., set on the text line. References are to be listed in numerical order on a separate sheet. All references are to be given in Latin letters. The names of the authors are given without inversion. Titles of journals must be abbreviated according to Chemical Abstracts and given in italics, the volume is typed in bold, the initial page is given and the year in parentheses. Attention is drawn to the following conventions: a) The names of all authors of a certain publications should be given. The use of "et al." in the list of references is not acceptable; b) Only the initials of the first and middle names should be given. In the manuscripts, the reference to author(s) of cited works should be made without giving initials, e.g. "Bush and Smith [7] pioneered...". If the reference carries the names of three or more authors it should be quoted as "Bush et al. [7]", if Bush is the first author, or as "Bush and co-workers [7]", if Bush is the senior author.

Footnotes should be reduced to a minimum. Each footnote should be typed double-spaced at the bottom of the page, on which its subject is first mentioned. **Tables** are numbered with Arabic numerals on the left-hand top. Each table should be referred to in the text. Column headings should be as short as possible but they must define units unambiguously. The units are to be separated from the preceding symbols by a comma or brackets. Note: The following format should be used when figures, equations, etc. are referred to the text (followed by the respective numbers): Fig., Eqns., Table, Scheme.

Schemes and figures. Each manuscript should contain or be accompanied by the respective illustrative material, as well as by the respective figure captions in a separate file. As far as presentation of units is concerned, SI units are to be used. However, some non-SI units are also acceptable, such as °C, ml, l, etc. Avoid using more than 6 (12 for review articles) figures in the manuscript. Since most of the illustrative materials are to be presented as 8-cm wide pictures, attention should be paid that all axis titles, numerals, legend(s) and texts are legible.

The authors are required to submit the text with a list of three individuals and their e-mail addresses that can be considered by the Editors as potential reviewers. Please note that the reviewers should be outside the authors' own institution or organization. The Editorial Board of the journal is not obliged to accept these proposals.

The authors are asked to submit **the** final text (after the manuscript has been accepted for publication) in electronic form by e-mail. The main text, list of references, tables and figure captions should be saved in separate files (as *.rtf or *.doc) with clearly identifiable file names. It is essential that the name and version of the word-processing program and the format of the text files is clearly indicated. It is recommended that the pictures are presented in *.tif, *.jpg, *.cdr or *.bmp format. The equations are written using "Equation Editor" and chemical reaction schemes are written using ISIS Draw or ChemDraw programme.

EXAMPLES FOR PRESENTATION OF REFERENCES

REFERENCES

- 1. D. S. Newsome, Catal. Rev.-Sci. Eng., 21, 275 (1980).
- 2. C.-H. Lin, C.-Y. Hsu, J. Chem. Soc. Chem. Commun., 1479 (1992).
- 3. R. G. Parr, W. Yang, Density Functional Theory of Atoms and Molecules, Oxford Univ. Press, New York, 1989.
- 4. V. Ponec, G. C. Bond, Catalysis by Metals and Alloys (Stud. Surf. Sci. Catal., vol. 95), Elsevier, Amsterdam, 1995.
- 5. G. Kadinov, S. Todorova, A. Palazov, in: New Frontiers in Catalysis (Proc. 10th Int. Congr. Catal., Budapest (1992), L. Guczi, F. Solymosi, P. Tetenyi (eds.), Akademiai Kiado, Budapest, 1993, Part C, p. 2817.
- 6. G. L. C. Maire, F. Garin, in: Catalysis. Science and Technology, J. R. Anderson, M. Boudart (eds.), vol. 6, Springer Verlag, Berlin, 1984, p. 161.
- 7. D. Pocknell, GB Patent 2 207 355 (1949).
- 8. G. Angelov, PhD Thesis, UCTM, Sofia, 2001, pp. 121-126.
- 9. JCPDS International Center for Diffraction Data, Power Diffraction File, Swarthmore, PA, 1991.
- 10. CA 127, 184 762q (1998).
- 11. P. Hou, H. Wise, J. Catal., in press.
- 12. M. Siney, private communication.
- 13. http://www.chemweb.com/alchem/articles/1051611477211.html.

Texts with references which do not match these requirements will not be considered for publication!!!

Selected papers presented at the 2nd Seminar on investigations, modeling, and optimization of nanocomposite structures, 2 April 2025, Sofia

CONTENTS

PREFACE	i
M. Dimova-Gabrovska, Y. Brusarska, E. Kirilova, D. Shopova, D. Damyanova, S. Rangelov, Wear resistance analysis of additively manufactured nanocomposite structures	5
A. A. Georgieva, F. S. Yovkova, K. Z. Panayotova, Synthesis, characterization and application aspects of barium titanate-based ceramic samples with graphene nanostructures introduced	13
M. G. Minova, F. S. Yovkova, I. G. Markovska, A. A. Georgieva, Synthesis and properties of Ni-doped fine dispersed ceramic pigments.	17
M. Dimova-Gabrovska, Y. Brusarska, E. Kirilova, S. Yanakiev, Z. Tomova, S. Rangelov, Adhesive bond between dentin and CROWNTEC with different printing orientations	23
D. S. Kiryakova, A. S. Ilieva, G. R. Kolchakova, Calcium carbonate nanoparticles as a filler for gelatin-based biofilms: preparation, characterization and properties	29
M. P. Miteva, V.O. Raikova, Application of Me-PAN nanocomposite membrane in two-stage ultrafiltration of industrial wastewater	36
M. Dimova-Gabrovska, R. Moskova, A. Vlahova, S. Rangelov, Nanofiller concentration in PMMA-nanocomposites for preliminary dental restorations	40
G. N. Nikolova, Thermal effects on concrete nanocomposites with central inclined cracks: Influence of crack geometry and nano-SiO ₂ content	52
G. N. Nikolova, Analytical and numerical study of thermal stresses and stress intensity factors in a concrete nanocomposite with nano-SiO ₂ under monotonically increasing temperature	61
N. Shukova, N. Armenova, D. Uzun, A. Gigova, O. Dimitrov, M. Dimtrova, L. Ljutzkanov, E. Razkazova-Velkova, Microbial and catalytic degradation of synthetic dyes	68
F. S. Yovkova, M. G. Minova, A. A. Georgieva, I. G. Markovska, Synthesis and properties of Cu - doped finely dispersed ceramic pigments	76
V. A. Angelov, R. K. Krastev, T. T. Batakliev, Preparation and analysis of epoxy/organoclay composites – structural characterization and mechanical properties	83
N. Shukova, D. Uzun, E. Razkazova-Velkova, K. Petrov, A. Gigova, O. Dimitrov, M. Dimitrova, L. Ljutzkanov, Electrocatalytic oxidation of H ₂ S by a ZrO ₂ catalyst on biochar carbon.	87
instructions to Authors	92